5-2018

Molten Core Fabrication of Bismuth-Containing Optical Fibers

Benoit Faugas
Clemson University

MOLTEN CORE FABRICATION OF BISMUTH-CONTAINING OPTICAL FIBERS

A Dissertation
Presented to
the Graduate School of
Clemson University

In Partial Fulfillment
of the Requirements for the Degree
Doctor of Philosophy
Materials Science and Engineering

---

by
Benoit Faugas
May 2018

Accepted by:
Prof. John Ballato, Committee Chair
Prof. Stephen Foulger
Prof. Liang Dong
Prof. Philip Brown

ABSTRACT

Glass optical fibers have generated significant commercial and research interest in the fields of communications, lasers and sensors since their successful development in the 1970s. Since then, higher performing optical fibers have arisen due to new and evolving demands necessitating the community to occasionally rethink the materials from which optical fibers are made. Although chemical vapor deposition (CVD)-based methods dominate due to their ability to make extremely low loss optical fiber, it is limited in the range of materials, hence properties, that can be brought to bear on modern problems. Accordingly, the method for fiber fabrication has proven to be a very useful technology from which fruitful knowledge and fiber performance has emerged. Not only does this technique allow the study of new and unusual glass optical fibers but it has also provided the opportunity of fabricating crystalline core analogs as well. Crystals, because of their regular structure, are very attractive fiber waveguide materials; particularly for electro-optic functionalities. The fabrication of crystalline oxide core phases using the molten core method is further intriguing because of the high quench speed (~m/min compared to mm/h for standard conventional crystal fiber growth techniques), which usually leads to amorphous phases. The possibility of fabricating both phases (crystals and glasses) whilst using conventional optical fiber drawing techniques is thus an attractive feature of the molten core method. The thermodynamic-kinetic interplay offered by said method is the central topic of this dissertation. The questions of *where does the thermodynamic takes over the kinetics when one draws fibers using the molten core method?* and *can one control crystal formation during fiber draw?* will be investigated. For that purpose, the bismuth germanate and bismuth silicate system will be explored for their

interesting electro-optic and nonlinear optic phases ($Bi_4Ge_3O_{12}$/$Bi_4Si_3O_{12}$ crystals and bismuth oxide glass).

Chapter I provides a background on optical fiber history and the principal optical fiber fabrication techniques. Additionally, the fundamental origin of nonlinearities in materials are described as are a few nonlinear applications.

Chapter II investigates the fabrication of $Bi_4Ge_3O_{12}$ (BGO) crystalline core fibers in borosilicate glass cladding. Phase pure BGO crystalline core fibers were demonstrated. It is shown that one needs to control the inherent core-clad interaction, which incorporates glass cladding compounds and prevents one to retain a stoichiometric melt in order to obtain a single phase. Nonetheless, the glass cladding compounds (SiO_2 notably) are found incorporated into the crystal structure and do not prevent the crystallization processes from taking place.

Chapter III explores the understanding of eulytine crystal formation during fiber draw in borosilicate and soda-lime silicate glass claddings. Homogeneous nucleation is investigated and refuted as a crystallization mechanism. Instead, heterogeneous nucleation is demonstrated as a pathway for crystal growth. The reaction $2Bi_2SiO_5 + SiO_2 \rightarrow Bi_4Si_3O_{12}$ for crystal growth is also considered but could not be identified as the mechanism.

Chapter IV studies the necessary processing conditions using the molten core method in order to fabricate bismuth-containing glass optical fibers. The materials' processing conditions are shown to affect the fiber core structure, where a low density precursor powder is necessary to achieve a glass core phase as a result of a volume expansion effect. Furthermore, it is found that fibers fabricated from a borosilicate

glass cladding are impractical due to cracks as a result of the CTE mismatch between core and cladding, and, soda-lime silicate glass cladding provides a better match. Finally, the thermo-reduction behavior of bismuth oxide is studied and it is shown that bismuth metallic nanoparticles are formed during fiber draw. The use of an oxidizing agent such as CeO_2 is shown to have no relevant impact on the formation of these nanoparticles.

DEDICATIONS

Pour ma famille et mes parents, Catherine et François.

ACKNOWLEDGEMENTS

First, I would like to thank my advisor and mentor Prof. John Ballato for awarding me a place in his group and giving me this challenging and futuristic project to work my mind around. Thank you also for sharing and translating your passion about optical fibers and glass/crystal science! Finally, thank you for providing me support and guidance with an ever-ending happiness and easy-going way, and, for the laughter's about the French way.

I would also like to thank Dr. Klaus Böhnert, who initiated and funded the project, for the discussion and support about the project itself and also for understanding the challenge. Also, thank you for receiving me at the ABB Company while I was visiting Switzerland.

I also show my gratitude to my committee members Prof. Stephen Foulger, Prof. Liang Dong and Prof. Philip Brown. Thank you for agreeing to be part of my committee and taking your time to serve in my committee.

Big thanks to Courtney Kucera for all the guidance throughout my years within the group. You have been of tremendous help! Thank you also for all your generosity (e.g., cooking) and for bringing a family ambiance to the group!

I will always be beholden to T. Wade Hawkins, Maxwell Jones and Kenneth Peters for drawing the optical fibers. Thank you also for the engineering discussion and the will to draw optical fibers, sometimes, within the limits of the materials.

Furthermore, I would kindly acknowledge the MS&E and COMSET staff members for providing me help within the university. Thank you Ms. Heather Cox, Ms. Sheryl Gonzalez and Ms. Sandra Bradberry. Thanks also goes to Mr. Donald

Mulwee for all his support and teaching at the electron microscope facilities, as well as for his (contagious) happiness.

Moreover, I am thankful for my group members for the science discussion and, everyday laughter's in the office: Laura, Josh, Matt, David, Amber, Baris, Ronaldo. A special thanks to my dear work colleague and friend of all time Maxime Cavillon for all the never-ending discussions about the molten core method, optical fibers, soccer, wine and, philosophy of life… T'es vraiment un mec à la cool.

Of course, my time through my PhD required more friends, and I would like to thank all my friends who have made this journey wonderful. The list is too long to detail but if you have crossed my path then you know your name belongs here. Special thanks to Jake Townsend, Bradley Schultz and Erica Linard (and their respective families) whom I am forever grateful for their friendship, incommensurable varieties of unpredictable discussions, and wonderful memories we have built. It would not have been the same without you!

Finally, it is my pleasure to acknowledge the friendship of Robert Bowen and his family for the tailgates, Sunday barbeques and, laughter's and caring at all times.

Financial support is acknowledged from the Department of Materials Science and Engineering and the ABB company (grant #2009842).

TABLE OF CONTENTS

Page

TABLE OF CONTENTS (CONTINUED)

Page

TABLE OF CONTENTS (CONTINUED)

Page

TABLE OF CONTENTS (CONTINUED)

Page

TABLE OF CONTENTS (CONTINUED)

Page

LIST OF FIGURES

Page

LIST OF FIGURES (CONTINUED)

Page

LIST OF FIGURES (CONTINUED)

Page

LIST OF FIGURES (CONTINUED)

Page

LIST OF FIGURES (CONTINUED)

Page

LIST OF FIGURES (CONTINUED)

Page

LIST OF FIGURES (CONTINUED)

Page

LIST OF TABLES

Page

LIST OF TABLES (CONTINUED)

Page

CHAPTER I

INTRODUCTION

I.1. A (short) history of glass fiber optics

Optical fibers are made of glassy materials, most typically silica, SiO_2. It is important to acknowledge that the history of glass optical fibers first requires a brief discussion of the history of inorganic glasses in order to put into proper perspective the requisite innovations that led to modern optical fibers.

Glasses have been made for millennials and glass making was originally considered an art and not, per se, a science. Glasses were highly-regarded materials despite their initial lack of transparency due to their inherent resemblance with precious stones (induced by the high color impurities content in the glass). With the advances of glass making techniques over the years as well as improvement in raw materials, transparent glasses first appeared in the early BC era and were well appreciated, for example, by the Romans (in 500 BC and after) who could observe the color of wine through the glass. Glasses and their fabrication techniques were nonetheless in danger during human history. The conquerors, and battles they fought, brought a decay in glass making knowledge as craftsmen holding knowledge were killed. Thankfully, the exodus engendered by the battles spread more the glass fabrication knowledge than killed it and, craft techniques and skills survived as they were carefully passed on in each civilization. Later on, starting in 1600s, the scientific activity and curiosity that was raised among the community largely involved glass materials in experiments and helped understand the world as it is today. For instance, the use of optical glass prisms allowed Isaac Newton to further study the behavior of

light and, the use of glass lenses in microscopes allowed Louis Pasteur to study diseases and vaccines in the field of medicine. Numerous experiments performed in the scientific field relied on glass at some point during the process; and it is, perhaps, all the collective glass knowledge accumulated by all the different civilizations through history that permitted the birth of the fiber optic world as we know it today [1].

Optical fiber is the generic term used to describe a thin, long glass material in cylindrical form, which is used as a transmission medium in a communication system. The optical fiber carries an input signal through the propagation of light in its interior until the output signal is decoded by a receiver/detector for further processing. Historically, the first transmission medium used to carry light was showed by Jean-Daniel Colladon in 1842, where he demonstrated that a falling stream of water could guide (and bend) light due to total internal reflection [2]. This was a first step towards optical fiber as one of its core principle relies on the same exact effect. Additionally, the idea of using light as a way of communication was first demonstrated in 1880, when Alexander Bell and Charles Tainter developed the first "radiophone/photophone" using the energy waves of the sun beams to transmit their voices [3]. Although the basic ideas behind the optical fiber communication system were demonstrated, there was still a lack of an adequate transmission medium. It was, perhaps, medical studies that pushed the beginning of the optical fiber realm. Starting in 1888, Dr. Roth and Prof. Reuss were interested in illuminating body cavities and, adapting the knowledge of these past experiments, they investigated the use of glass rods as a tool for their means. Their investigations (along with other scientists) were successful and by the 1920s bent glass rods were common for illumination in

surgeries. This was thus somewhat a second step towards the fabrication of optical fibers as the ability of glass to transmit light was demonstrated. In 1926, Clarence W. Hansell, an American electrical engineer, successfully investigated the use of light guiding through glass fiber bundles rather than glass rods for image transmission in remote viewing [4]. By the beginning of the mid-1950s, Danish Holger Hansen and Abraham van Heel proposed the addition of a second layer of glass onto the fibers to improve the light transmission, which also proved to be a major step towards reduction of interference between glass fibers in the bundle [5]. This constituted the third step in the design of optical fibers. In late 1956, Larry Curtiss, then an undergraduate student at the University of Michigan, makes the first glass-clad fibers (for endoscope purposes) using for the first time the rod-in-tube method [6], technique that will be later employed to make the first optical fiber.

While all the concepts for making an optical fiber as we know it today were laid down (i.e., total internal reflection, glass as a transmission medium, glass-cladding design and, use of light as an information carrier) the use of glass optical fibers for long-distance telecommunications was not mused yet. Telecommunications application was the main driving force towards optical fiber research: the amount of data from telephone calls and video were increasing and needed to be carried further away. It was not until 1960 when Townes and Schawlow laid down the principles of laser operation [7] (in conjunction with the independent work of Russian scientists Prokhorov and Basov [8], [9]) that optical waves were studied more intensively for carrying information. Although micro waves were being investigated at the time for transporting information, optical waves would prove more beneficial due to their inherent ability to carry a larger amount of information (imparted from their higher

frequency). The first lasers demonstrated by Maiman [10] and Javan [11] early after the laser principles were established was shown to be a suitable source for carrier waves. However, a suitable transmission medium was not yet thought of and transport of light in air was proven impractical. It was in 1966 that Kao and Hockham at Standard Telecommunication Laboratories (STL) theoretically demonstrated that silica-glass-based fibers could be a suitable medium for optical communication [12], and they provided an unprecedented motivation towards the making of optical fibers. They suggested that impurities would be a major impairment for achieving low-loss optical fibers using silica glass, and an upper limit of 20 dB/km was conceived for practical applications. Maurer at Corning Glass Works started a small research project in 1966 on the making of glass cladded optical fibers. Knowing that impurities were the main problem, he used high purity glasses that were first made available by Hyde through his flame hydrolysis method [13]. He teamed up with Zimar to draw single mode optical fibers out of the rod-in-tube method using a titania (TiO_2)-doped silica glass rod as a core (used by the company as ultra-low expansion glass for lenses) and fused silica tube as the cladding. Although being successful in their protocol, irregularities obtained during the process scattered the light significantly. At the same time, scientists at Bells Labs and the British Post Office were investigating a new technique, the double crucible method, where concentric molten glass streams could be drawn into fiber continuously. However, as in every research team of the time, impurity absorption in fibers was still troublesome and hard to reduce. It was in 1970 that the breakthrough appeared, when Keck and Schultz developed at Corning Glass Works the inside vapor deposition process. They deposited titania uniformly into a fuse silica tube, which provided them the preform to draw fibers: they had achieved a

loss of 16 dB/km [14], [15], below the 20 dB/km mark suggested by Kao. The fiber was not yet practical as titania was reduced during fiber draw and the newly formed oxidation state absorbed light (and additional heat treatment cycles under oxygen atmosphere led to titania crystallization, which made the fiber very brittle). In the meantime, they had changed their methods to the outside vapor deposition (OVD) technique [16] using the flame hydrolysis technique developed by Hyde and they worked with a more suitable dopant, i.e., germania (GeO_2). In 1972, they reached a loss of 4 dB/km, now making the first practical optical fiber and thus opening the era of optical fiber for long-distance telecommunications [17] (and much more applications later). One year later, a new fiber fabrication method was developed by MacChesney at Bell Labs where he used the so-called modified chemical vapor deposition process (MCVD) [18]. This technique used a different chemical reaction than in OVD and proved to be efficient as well in producing low loss fibers. In early 1976, losses of 0.47 dB/km at 1.2 μm were reported by Horiguchi and Osanai at the Nippon Telephone and Telegraph (NTT) Company in Japan using MCVD [19]. In 1977, an additional fabrication method was uncovered by Izawa, namely the vertical axial deposition (VAD) technique, who worked at NTT on its own optical fiber project [20]. The three techniques were similar in a sense that they used chemical vapor deposition processes, and it is in their designs that they differed, but all demonstrated low losses necessary for the targeted telecommunications applications. The seeking for fabrication of low loss optical fibers and its feasibility was thus pioneered closely in the 1970s and the understanding of the techniques was the next focus to improve the fabricated optical fibers for commercial uses. Communication

systems were then tried and installed successfully in different countries during the late 1980s, thus fully opening the age of optical fibers.

Further improvement in the optical communication fiber system was made in 1987 when David Payne reported the first erbium-doped optical fiber amplifier (EDFA) at 1.54 μm at the University of Southampton in England, which overcame the problem of attenuation when dealing with kilometer-long optical fibers [21]. This newly designed fiber allowed one to amplify a signal all-optically, thus suppressing the need of an opto-electrical converter system and improving the systems' cost and efficiency. Furthermore, the tremendous success of optical fibers allowed the scientific community to study optical nonlinearities in more depth over the next years (see [22]) due to the inherent design of optical fiber waveguides and their low losses. For instance, nonlinear effects such as Stimulated Raman Scattering (SRS) and Stimulated Brillouin Scattering (SBS) [23] were demonstrated and shown to have undesirable consequences on communication system performances. Despite this, nonlinear phenomena offered interesting properties and scientists showed they could be used to one's advantage. The field of nonlinear fiber optics was created and nonlinear optical fibers became integrated in communication systems.

From here, it seemed that scientists managed to overcome the largest issues on the material and processing sides when dealing with light transport in silica fibers. The data transmission rate delivered in the optical fibers increased year after year up to millions of bit per second, and the bandwidth of optical fibers was large enough to accommodate all information. Although optical fibers were widely used first for long-distance telephone service, and later for computer-related telecommunications

(Internet), new and ever-long growing technological demands call for specialty optical fibers with novel materials and/or designs.

I.2. Optical fiber fabrication technologies

As mentioned in the above section, losses in optical fibers were a major concern, mainly due to the transition metals and hydroxyl groups present in the glass that absorbed a significant amount of light over a wide spectral range. Four major preform fabrication techniques were designed over the past decades to overcome this problem such as OVD, MCVD, VAD and PCVD (Plasma Chemical Vapor Deposition). They are all based on a same technique, i.e., chemical vapor deposition (CVD). The fundamental principle lying behind the use of CVD is built on the ability to select highly pure precursor gas compounds from a high purity liquid due to the large difference in vapor pressures between the desired gas precursors and the impurities gas compounds. In this regard, gas precursors such as $SiCl_4$, $GeCl_4$, PCl_3, BCl_3… were shown to be of high interest due to their vapor pressures being several orders of magnitudes higher than that of other impurities (up to ~10^{10} atm difference with Fe_2Cl_6 for example [24]). Thus, $SiCl_4$, $GeCl_4$… readily volatilize while the impurities do not and stay in the liquid form. The other advantage of the CVD technique is that the high vapor pressures are obtained at room temperature, thus facilitating the process. Each individual CVD technique possesses its own design that will ultimately affect the end properties of the drawn fibers (for a comparison, see [25]). Despite the dissimilarities between the preform fabrication techniques, losses close to the theoretical value could be obtained, e.g., on the order of <0.2 dB/km.

We will now briefly detail the OVD process (for a review, see [26]), scheme of which is provided in Figure I-1. This technique starts with a rotating mandrel onto which soot particles are uniformly deposited. The soot particles are directed on the mandrel and formed through flame hydrolysis deposition, whereby halides ($SiCl_4$, $GeCl_4$, $POCl_3$, BCl_3…) are passing through an oxy-hydrogen flame burner to form the desired oxides. The chemical reactions taking place in the burner are as follow: $XCl_{4\,(g)} + O_{2\,(g)} \rightarrow XO_{2\,(s)} + 2Cl_{2\,(g)}$ (oxidation) and $XCl_{4\,(g)} + 2H_2O_{\,(g)} \rightarrow XO_{2\,(s)} + 4HCl_{\,(g)}$ (hydrolysis) with X=Si, Ge [27]. The oxide composition deposited is varied by carefully selecting processing parameters such as flow rates of gas precursors and flame temperature, which will ultimately control the refractive index profile of the end fiber. Then, the mandrel containing the deposited oxide soot is removed and the soot porous preform (called "blank") is consolidated in a high temperature furnace, were the soot particles on the blank are sintered and transformed into a glass. Gas flow of chlorine (Cl_2) and helium (He) are usually employed to dry and clean the soot blank central line from hydroxyl groups, and SiF_4 gas can also be utilized to dope the preform with fluorine during the consolidation step [28]. The obtained glass preform is then taken for fiber draw. The advantages of this technique (as well as VAD) is that very low loss optical fibers can be produced with a good control of refractive index profiles. Plus, large amount of soot particles can be deposited and hence very large glass preform can be employed, which is beneficial for large scale production.

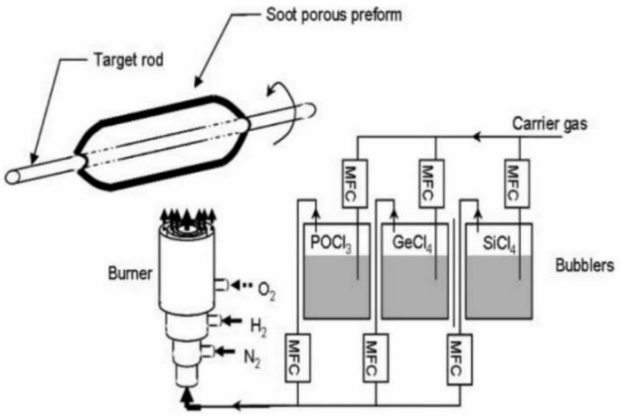

Figure I-1. Fabrication principle of the Outside Vapor Deposition (OVD) technique (taken from [27]) in the making of optical fiber glass preform.

We will now briefly detail the MCVD process (for a review, see [25]), which is mainly used for specialty optical fiber fabrication. In this process, the soot deposition is carried out inside a rotating silica glass substrate tube, in contrast to the OVD process where it is carried out on the outside of a mandrel. MCVD uses the oxidation reaction similar to OVD: $XCl_{4\,(g)} + O_{2\,(g)} \rightarrow XO_{2\,(s)} + 2Cl_{2\,(g)}$ (with X=Si, Ge). The precursor gas streams are flowed through the tube and an outside moving flame passing along the tube triggers the reaction. Small SiO_2 particles are deposited downstream through thermophoresis process and, as a result, a porous white soot layer is formed on the inside walls of the tube (see Figure I-2). This will be subsequently consolidated/sintered through various heating steps to form a glass and the tube will be collapsed on its own at high temperatures to form a solid glass preform ready to be drawn to fiber. Additional gas such as Cl_2 can be added during these processes to purify the glass from impurities.

MCVD is the most widely used method in research due to its highest degree of flexibility in compositional changes. For instance, an additional step can be introduced before the consolidation process in order to introduce rare-earth (RE)

oxides and aluminum oxide in the glass to make active optical fibers (step that is not available with the OVD process). This is achieved whether through solution doping or gas phase deposition technique (for a review, see [29]). Solution doping is perhaps the simplest of the two techniques. Briefly, it requires one to soak the soot blank with an aqueous solution of RE and Al salts for a few hours. The soot blank is then dried and, upon the consolidation process, the RE and Al elements are converted to oxides and are incorporated into the glass matrix. This allows the making of suitable high quality laser fibers in the telecommunication window.

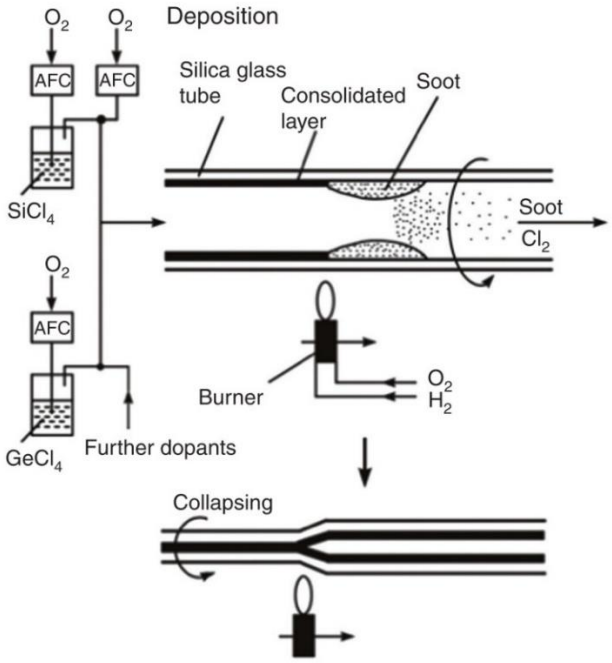

Figure I-2. Fabrication principle of the Modified Chemical Vapor Deposition (MCVD) technique in the making of optical fiber glass preform (taken from [29]).

Notwithstanding the tremendous efforts involved in the fabrication processes of optical fibers, their evolution constantly directed them towards greater functionalities, driven by needs for higher fiber performance. The standard single mode optical fibers used today show great properties for optical communications but demonstrate

limitations for other potential applications. Larger amount of materials as well as new materials would be beneficial to enhance the fibers' functionalities. However, the CVD-based techniques are restrained in terms of gas precursor compounds availability, as well as precursor content incorporation in the glass preform without difficulty. Thus, one cannot introduce new materials or large concentrations of standard material. Hence, new ways of thinking about optical fibers fabrication were necessary to meet the new upcoming challenges. The development of microstructured optical fibers (MOFs) and particularly hollow core photonic crystal fibers (HC-PCF) in the mid-1990s was shown to be one great route to increase fibers' performance [30]. In this technology, the core structure is modified by introducing air-holes that forms a regular pattern around a plain core and the light is guided by constructive interference of the scattered light generated at the air-hole interface. Many different core designs can be assembled to modify the fibers' properties such as nonlinearities or dispersion profiles. The main fabrication method for MOFs employs the stack-in-draw technique (Figure I-3). Thin silica capillaries are stacked together in an array, then introduced in the core preform, and finally drawn to fiber size under pressure. These fibers are silica-based and thus allowed a smooth development transition from standard optical fiber fabrication, requiring "only" an understanding of physical core structure effects. Despite showing enhanced performance and adaptability, their fabrication is not so straightforward and one must go towards better core structure complexity to meet higher fiber performances.

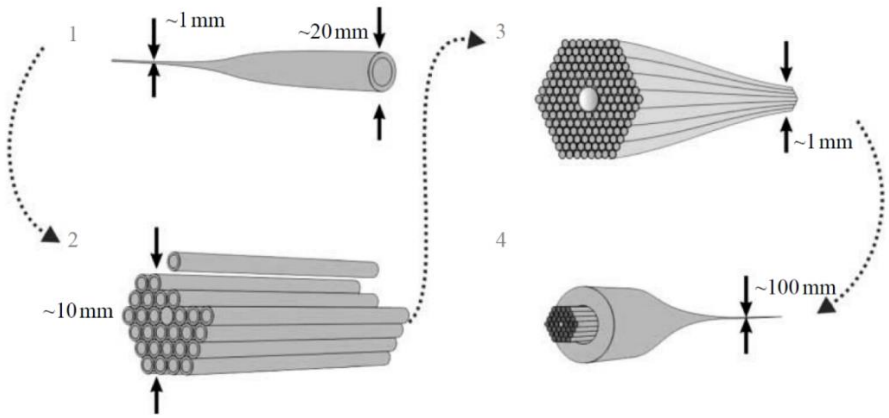

Figure I-3. Fabrication technology of hollow core photonic crystal fibers (taken from [31]).

An alternative fabrication approach to the conventional CVD methods was demonstrated in the mid-1990s by Ballato, et al. [32]. This technique, known as the molten core method (or powder-in-tube method), allowed the realization of optical fibers possessing new core compositions that previously could not be fabricated using CVD or conventional glass melting method. This, in turn, permitted the use of the intrinsic properties of new compounds as a tool (rather than the core structure) in order to enhance the fibers' functionalities [33]. In this technique, a hollow core glass preform is utilized in which a precursor material of choice is introduced (in the form of a single crystal, crystalline powder, glass rods…). The precursor material undergoes a melting phase transformation during the heating of the preform and the melt is then quenched during the fiber draw (Figure I-4). Thus, the glass preform acts as a crucible of high purity within which one can melt a wide range of compositions.

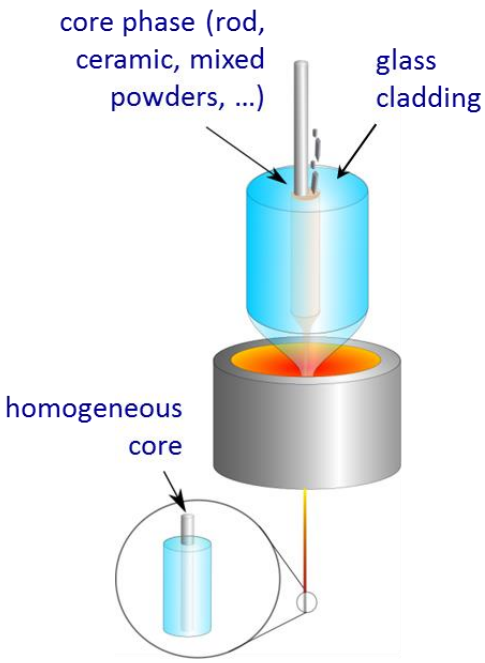

Figure I-4. Fabrication technology of the molten core technique (taken from [56]).

This technique was shown to be straightforward, providing scalability and, enabling the fabrication of long length of flexible optical fibers. Various unusual and unstable glass core compositions were fabricated and demonstrated interestingly low nonlinear optical properties compared to conventional fibers [34]–[39]. One of the main practical issue of the molten core method lies in the low purity of the precursors compounds available and thus the high losses exhibited in the fabricated fibers. In addition to glass core fibers, the molten core technique has established the capability of fabricating crystalline core optical fibers. This was first demonstrated in the semiconductor family with silicon, germanium and indium antimony [40]. This indubitably showed the large potential that this method could offer, combining the standard fabrication methods for crystals and glass optical fibers. Nowadays, single crystalline fibers are fabricated through methods such as, the Czochralski method [41], the micro-pulling down method [42] or the laser heated pedestal growth method

[43]. These fabrication techniques allow the making of good quality single crystalline fibers but employ slow crystal growth rates (see Table I-1). Furthermore, these fibers are not cladded in-line for waveguide properties and are limited in terms of length of fibers that can be drawn at once. Therefore, there is a technological interest to fabricate such crystalline fibers using an optical fiber fabrication technique that could palliate these difficulties. While the molten core method showed the fabrication and crystallization of core material in the semiconductor family, this raised the scientific question of: could this be achieved in the oxide crystal family? Oxide crystals are of great interest for their optical properties whether, for instance, as rare-earth hosts for laser applications or as noncentrosymmetric crystals for electro-optic applications. In the case of lasers, single oxide crystalline core optical fibers could provide much better thermal management, higher cross section efficiencies compared to bulk crystal and easier integration into systems. Thus, there is a necessity to investigate the formation of oxide crystals using the molten core approach. Ballato, et. al. [44], showed the reactive fabrication and transformation of a $Bi_{12}GeO_{20}$ single crystal into a mixture of Bi_2GeO_5 and Bi_2O_3 crystals, thus exhibiting a first proof-of-concept for the crystallization of oxide material during fiber draw.

Table I-1. Relative crystal growth rates in various standard single crystal growth techniques as compared to the molten core method.

Crystal growth technique	Growth rate	Relative rate	Reference
Hydrothermal	<mm.day^{-1}	1	[45]
Micro-pulling down	≤mm.hr^{-1}	~25	[46]–[49]
Czochralski	~mm.hr^{-1}	~1000	[50], [51]
Laser heated pedestal growth (LHPG)	~mm.min^{-1}	~1,500	[52]
Molten core (cane)	m.min^{-1}	~1,500,000	[53]
Molten core (fiber)	m.s^{-1}	>20,000,000	[54]

The molten core method is a technique that is less well evaluated than the standard fabrication techniques, perhaps due its complexity with interconnected processing parameters. The most intriguing facet of this technique is, perhaps, its ability to form crystal while drawing at large speeds (m/min at least). Generally, melts are kinetically trapped and quenched into a glass phase during fiber draw but the crystal nucleation and growth at high quenching rates is somewhat fascinating and provocative. The thermodynamic (i.e., crystal formation) and kinetic (i.e., glass formation) interplay provided by the molten core technique is not well comprehended and thus requires further investigation. In this dissertation, we will then focus on understanding the science of formation of crystal and amorphous phase using the molten core method. We will also understand the limitations of single oxide crystal growth using the molten core approach, and understand how to control the crystals' formation during fiber draw through designs. Furthermore, we will provide an understanding of the precursor materials' processing in relationship to the molten core method using soft glass cladding preforms.

In order to investigate the thermodynamic-kinetic interplay problematic, the binary systems Bi_2O_3-GeO_2 and Bi_2O_3-SiO_2 were chosen as candidates for their interesting nonlinear and electro-optic phases. Each binary system shows the ability of forming stable crystals such as $Bi_{12}GeO_{20}$, $Bi_{12}SiO_{20}$, $Bi_4Ge_3O_{12}$ (BGO), $Bi_4Si_3O_{12}$ (BSO), and metastable crystals Bi_2GeO_5, Bi_2SiO_5. Furthermore, Bi_2O_3 is considered an intermediate glass former and can easily form a glass when mixed with a good glass former such as germania and silica (and quenched at high rates). Glass formation in both binary systems can be achieved over a wide range of concentration, and glasses up to 90 mol% Bi_2O_3 in the Bi_2O_3-SiO_2 system were reported in the literature [55]. Thus, bismuth oxide based systems are good candidates to study the thermodynamic-kinetic interplay exhibited by the molten core method. The BGO and BSO crystalline phases are attractive for their electro-optic properties, which can find applications as high voltage sensors or wavelength converter, while the glass phase is of interest for its nonlinear optic properties, which can find applications for all-optical signal processing, supercontinuum generation or Raman amplification. An understanding of nonlinearities and their material origin will be explained in the next section I.3. Note that for practical applications of crystalline core optical fibers, three requirements need to be met for the crystalline core: “phase pure”, meaning that there is only one crystal structure and no other crystalline phases detected with X-ray diffraction; “single phase”, meaning that the core is fully crystalline in terms of microstructure with crystals occupying the full core volume (no amorphous phases); and, “single crystalline”, meaning that no grain boundaries are formed and that the one core crystal exhibit one single orientation along the fiber axis.

I.3. Nonlinearities in optical fibers and their applications

Fiber nonlinear optics is a field that can be considered as a sub-discipline of modern optical fibers. It is based on the comprehension of nonlinear effects occurring when light interacts with matter. New nonlinear phenomena were discovered in optical fibers shortly after the fabrication of the first optical low loss optical fibers in 1970. In short, the nonlinear effects modify the input photons properties and generates new modulated output photons, which can be harvested for their interesting properties. While the discovery of second harmonic generation (SHG) by Franken, et al. [57], in 1961 can be considered the beginning of the nonlinear optic area (imparted by the availability of a strong laser radiation provided by Maiman in 1960), nonlinear optical effects were known before the invention of the laser. Amongst such nonlinear effects, the well-known Pockels and Kerr effects appearing in bulk materials were already studied and understood [58], [59]. Nonetheless, the newly fabricated optical fibers provided suitable conditions for observation of new phenomena due to their low loss and tightly confined mode in their small cores, which allowed a long length of interaction between the electromagnetic field of the light and the core matrix. At this time, the world of nonlinear optics in optical fibers was nascent and new phenomena were brought into light such as three-wave mixing [60], four-wave mixing [61], stimulated Raman scattering or stimulated Brillouin scattering [62] amongst others. Although these phenomena were unwanted then due to their negative effects on long distance optical fiber communication systems, it was realized that new applications could emerge from them and thus their studies were forthcoming at high speed. Nowadays, the realm of nonlinearities is very wide owing to the large variety of

materials that can exhibit nonlinearities (virtually all of them) and the broad number of phenomena that result from them.

I.3.1. Introduction to nonlinear optics

We will first review here the origin of nonlinearities from a materials' viewpoint. For that matter, we will describe the electronic polarization and then derive the linear equation of polarization using the classical harmonic oscillator model. Then, we will introduce nonlinearities in the derivation of the polarization equation. Finally, we will introduce nonlinearities as related to optical fibers and discuss, briefly, some nonlinear effects and their potential applications.

I.3.1.1. Electronic polarization

Taking the general and simplest model of an atom, it is known that this latter is made of a positive nuclear charge center of mass, comprised of neutrons and protons, surrounded by electrons orbiting around this positive center, forming an electronic cloud. This atom is electrically neutral as the charge distribution center of mass from the electrons coincide with that of the positive charge distribution of the protons. If an applied electric field E is applied to this same atom, the trajectories of the electrons will now be influenced by the applied electric field, and the electrons will be displaced in accordance to the applied electric field (whether it is a DC or AC field)[1]. As a result, the electronic cloud center of mass will be displaced and a separation between the positive and negative distribution center of mass will be created. This separation gives rise to an induced electric dipole moment[2] $p_{induced}$ and it will be said

[1] Throughout this section we will consider an AC field such that in equations $E=E_0\sin(\omega t)$.
[2] An electric dipole moment p is a vector defined as a separation of a positive and a negative charge of equal magnitude Q such that $\boldsymbol{p} = Q\boldsymbol{x}$, where $\boldsymbol{x}$ is a vector from the negative to the positive charge and this forms the basics of polarization.

that the atom is polarized. In other terms, the applied electric field E (cause) induces an electric dipole moment $p_{induced}$ (consequence). This is mathematically described by the following equation:

$$p_{induced} = \alpha E \tag{1.1}$$

where the coefficient α is termed the polarizability of the atom. All atoms and molecules contain electrons in their structure that are able to be displaced under the application of an electric field. Hence, all atomic elements can be polarized, the difference between each of them being the extent with which it can be polarized and is differentiated through the use of α. It is worth noting that the coefficient α includes different types of polarization mechanisms (electronic, nuclear, ionic,…) and that there is a frequency dependence for each contribution (further discussion on polarization mechanisms can be found in [63].) Here, for simplification, only the contribution from the electronic cloud (and most likely outer shell electrons of the atoms [64]) is considered, as the electrons are the lightest elements in the atomic structure that can easily respond to the electric field at the optical frequencies of interest (Visible/Near Infrared). We will thus talk about electronic polarization.

The electronic polarization induced by the applied electric field gives rise to a Coulombic force between the two charge distribution center of mass. Indeed, while the applied electric field drives the electrons away from the nucleus, the Coulombic force produced between electron and nuclear charges attracts the electrons back toward the nucleus. This restoring force (noted F_r) is proportional to the displacement x between the two charge distribution center of mass and is written as:

$$F_r = -\beta x \tag{1.2}$$

where β is a proportionality constant and the negative sign implies that the force is always directed toward the nucleus. Thus, there is a net balance of forces while the electric field is applied, where the force F created by E to drive the electrons away from the nucleus ($F = qE$, with q the electron charge) is balanced by the coulombic restoring force F_r, as:

$$-ZeE = -\beta x \tag{1.3}$$

Thus, we find out that the magnitude of the induced electronic dipole moment is:

$$p_e = Qx = \frac{Z^2e^2}{\beta}E \tag{1.4}$$

From the Equation 1.1, the electronic polarizability α_e is defined as:

$$\alpha_e = \frac{Z^2e^2}{\beta} = \frac{Ze^2}{m_e\omega_0^2} \tag{1.5}$$

where ω_0 is the electronic resonance frequency at which the electron cloud exhibit simple harmonic motion around the nucleus when the electric field is removed (introduced and deduced from Newton's second law, see [63]). Note that the way the electronic polarizability is written in Equation 1.5, it is assumed that the oscillations are carried out in a lossless medium.

I.3.1.2. Origin of nonlinearities and nonlinear equations

While the aforementioned view of polarization considers only one atom and is thus a microscopic polarization, materials deal with a large collection of atoms. Thus, when a material is subjected to an electric field, all the atoms and molecules within the material become polarized, so that a macroscopic polarization *P(t)* develops throughout the material. This latter is defined as:

$$P = Np_{induced} = N\alpha_e E \tag{1.6}$$

where N is the number of atoms/molecules per unit volume. It is thus seen that the macroscopic polarization is linearly dependent with the electric field. Furthermore, the linear dependency between the macroscopic polarization and the electric field can be expressed as follows:

$$P(t) = \varepsilon_0 \chi^{(1)} E(t) \tag{1.7}$$

where ε_0 is the dielectric constant in vacuum and, $\chi^{(1)}$ is the first-order electric susceptibility that serves as a proportionality constant. Equation 1.7 constitutes the linear polarization.

We have considered previously that the electrons displacement around the nucleus was linear with the electric field (i.e., linear restoring force), which is an assumption valid for weak applied electric field. When the applied electric field becomes comparable to interatomic electric fields (~10^5-10^8 V.m^{-1}), the electrons do not move harmonically with the electric field (i.e., they move anharmonically). There is now a nonlinear dependence of the restoring force with the displacement of the center of mass. This anharmonicity is introduced in the classical harmonic oscillator model (now anharmonic) through the restoring force equation by expanding x in a power series in Equation 1.2, such that:

$$F_r = -\beta x - \zeta x^2 - \eta x^3 \tag{1.8}$$

In order to find the expression of the macroscopic polarization P, one needs to solve the equation of motion of the electron through Newton's second law (the derivation step will not be followed here and the reader is referred to Ref. [65]). In a general

form, the nonlinearities introduced in the restoring force are translated to the (now nonlinear) macroscopic polarization by expanding the electric field in a power series (assuming that changes in polarization are relatively small), such that Equation 1.7 becomes:

$$P(t) = \varepsilon_0[\chi^{(1)}E(t) + \chi^{(2)}E^2(t) + \chi^{(3)}E^3(t) + \cdots] \quad (1.9)$$

where, $\chi^{(2)}$ and $\chi^{(3)}$ are the second-order and third-order electric susceptibilities, arising from the nonlinearity of the restoring force. Thus, one can see that nonlinearities in a material truly originate from the electronic polarizability of an atom or molecule and the anharmonic oscillations of the electrons constituting an atom around the nucleus when an intense electric field is applied. We can also rewrite Equation 1.9 as follow:

$$P(t) \equiv P^{(1)}(t) + P^{(2)}(t) + P^{(3)}(t) + \cdots \quad (1.10)$$

where, $P^{(2)}(t)=\varepsilon_0\chi^{(2)}E^2(t)$ and $P^{(3)}(t)=\varepsilon_0\chi^{(3)}E^3(t)$ are referred as the second-order nonlinear polarization and third-order nonlinear polarization respectively.

It is then important to consider the effect of a materials' structure on the nonlinearities. Let us assume that the nonlinear polarization is given by the second-order nonlinear polarization. If we consider a material possessing a center of inversion such as a centrosymmetric crystal, a change of sign in the electric field (i.e., change of polarization state by 180°) should also change the sign of the macroscopic polarization due to the inversion center. In this case, we have:

$$-P(t) = \varepsilon_0\chi^{(2)}[-E(t)]^2 = \varepsilon_0\chi^{(2)}E(t)^2 = P(t) \quad (1.11)$$

We thus see that P(t) must equal −P(t) and, this condition can only be met if $\chi^{(2)}=0$. In other terms, centrosymmetric crystals (as well as liquids and glasses) should not exhibit a second-order nonlinear susceptibility. Therefore, only noncentrosymmetric crystals belonging to a certain crystal class with specific point group will exhibit second-order nonlinear effects. Note, nonetheless, that centrosymmetric materials can exhibit a non-zero $\chi^{(2)}$ under special conditions, see for example [66], [67].

Furthermore, it is worth recalling that the square of the electric field, $|E|^2$, is proportional to its intensity, I. We will thus find that, in the case of centrosymmetric materials such as glasses (where $\chi^{(2)}=0$), nonlinearities can be expressed in terms of the refractive index [$n \propto P(t)/E(t)$] simply as:

$$n = n_0 + n_2 I \tag{1.12}$$

where, n_2 is the nonlinear refractive index and is proportional to (the real part of) $\chi^{(3)}$ in Equation 1.9 and is thus proportional to the electronic polarizability. One can see that changes of refractive index can occur as a result of changes in light intensity due to the intensity-dependent refractive index. Various models have been proposed to model n_2 on the basis of different parameters in glasses and can be found in [68].

While all the aforementioned equations describing nonlinearities are valid for any type of materials, optical fiber waveguides are a special case. A nonlinear parameter γ is introduced for expressing nonlinearities in optical fibers and is defined as [69]:

$$\gamma = \frac{2\pi n_2}{\lambda A_{eff}} \tag{1.13}$$

where, n_2 is the nonlinear refractive index, λ the wavelength of operation, and A_{eff} the effective mode area. As seen in Equation 1.13, nonlinearities in optical fibers depend

not only on the material parameter n_2 (as expected) but also on the effective mode area. Within the cross-section of a fiber, the power is non-uniformly distributed and the intensity of the light is inversely proportional to the area of the core. Thus, the light-matter interactions (and thus nonlinearities) are enhanced in optical fibers compared to bulk materials due to the confinement of the optical electric field in a small core area. This light intensity dependency with core area in optical fibers is then added to the material nonlinearities using A_{eff}. For completion, the effective mode area depends on optical fiber parameters such as core radius and core-cladding refractive index difference [69], which can be tuned to design nonlinear properties in optical fibers.

As previously discussed, the linear and nonlinear macroscopic polarization result from the application of an electric field to the material, and it is important to make a distinction about the nature of this latter. The applied electric field could originate from two different sources: whether it is applied to the material through a voltage, or it is applied via an incident light beam travelling through the material. The former case refers to the field of electro-optics, while the latter case refers to field of nonlinear optics. In the case of electro-optics, the nonlinear polarization equation is preferred to be written as a change of refractive index *n*, as follows:

$$\Delta(1/n^2) = rE + sE^2 \tag{1.14}$$

where, *r* is called the linear electro-optic coefficient (i.e., the Pockels coefficient) and *s* is called the quadratic electro-optic coefficient (i.e., the Kerr coefficient). We will note here that, for simplicity, the refractive index (and polarization) and electric field were taken to be scalar quantities in all previous written equations (i.e., independent

of field direction and thus assumed an isotropic material). Nonetheless, a more rigorous treatment of the vector nature of the fields (and anisotropy of the medium) implies the use of a tensor notation for the nonlinear electrical susceptibilities and electro-optic coefficients (more in Ref. [65], [70]). This can be understood by the fact that the different bond lengths in a material exhibit different bond polarizabilities along different directions. We will now review the effects and applications induced by the second- and third-order nonlinear susceptibilities.

I.3.2. Second-order nonlinearities in optical fibers and their applications

We will first consider here the second-order nonlinearities in connection to the field of electro-optics. As we have previously discussed, materials lacking an inversion center exhibit a Pockels coefficient. Thus, when applying a voltage to a noncentrosymmetric (single) crystal, the refractive index of the single crystal will change accordingly along the different axes of the crystal and, as a result, the single crystal will become birefringent. Basically, if a linear polarized wave is launched along the z-axis of a single crystal cylinder, an optical phase shift is induced and the wave is decomposed into two components. Note that this is best achieved if the single crystal orientation in the *z*-axis is oriented along the [001] crystal plane, such that the refractive index does not change in the *z* direction but only in the transverse direction. The created optical phase shift between the two waves is proportional to the applied voltage [70] and can then be used to deduce the magnitude of the applied voltage. Thus, if one can fabricate a noncentrosymmetric single crystalline core optical fiber, one can use this latter as high voltage sensor. For example, bismuth germanate $Bi_4Ge_3O_{12}$ and bismuth silicate $Bi_4Si_3O_{12}$, both with eulytine crystal structures, exhibit a large Pockels coefficient [71] and are ideal candidate materials [72], [73]. For an

actual device configuration, the reader is referred to Ref. [74], [75]. Voltage measurement is a key component in the protection of electric power grids in order to avoid faults. Nowadays, voltage measurements in power substation are mainly performed using instrument transformers, which are not immune to electro-magnetic interference, may show undesired galvanic connections and, are bulky equipment. Regarding both safety and environmental footprint points, fiber-optic voltage sensors are highly adapted to these high voltage environments. They provide inherent galvanic isolation of electronics from high voltage, provide total voltage measurement and thus better accuracy and, could replace tons of conventional equipment leading to much smaller environmental footprint. Additionally, the inherent design of an optical fiber such as small weight and size instrument with inherent immunity to electromagnetic interference is beneficial. Thus, the fabrication of optical fibers possessing a (noncentrosymmetric) crystalline core for fiber-optic voltage sensor is of great motivation.

Let us now consider the field of nonlinear optics. Crystals exhibiting second-order nonlinearities have the possibility of emitting light at twice the frequency (or half the wavelength) of the incident light launched into the crystal. This phenomenon is known as second-harmonic generation (also described as a second-order parametric process). Considering the general equation for nonlinearities (Equation 1.9) and taking the electric field of light as $E(t) = E_0 \sin(\omega t)$, one obtains:

$$P(\omega, t) = \varepsilon_0 \chi^{(1)} E_0 sin(\omega t) + \varepsilon_0 \chi^{(2)} E_0^2 sin^2(\omega t) + \varepsilon_0 \chi^{(2)} E_0^3 sin^3(\omega t) \quad (1.15)$$

Recalling the trigonometry relation $2sin^2(x) = 1 - \cos(2x)$ with $x = \omega t$, and assuming only second-order nonlinearities one can see that the nonlinear polarization

will radiate new photons at frequency 2ω (or half-wavelength) in addition to photons at frequency ω (i.e., incident light beam frequency). Hence, noncentrosymmetric BGO and BSO crystalline core optical fiber could be used for generating new wavelengths at half the wavelength of the incident beam. This could be useful for medical treatments, spectroscopic and environmental sensing applications, where rare-earth laser transitions do not offer the desired wavelengths. Note, nonetheless, that the special condition known as phase matching is required in order to efficiently generate a new wavelength. This requires the wavevector of the incident and generated electric fields to be equal so that the amplitudes of the waves are all in phase and construct in the same direction (see ref. [65], [69] for more information).

Furthermore, nonlinear effects tend to be proportional to the light beam intensity launched into the crystal as well as the length of interaction, and many applications would be more beneficial if long crystal length were available. The fabrication of crystals in optical fiber waveguide designs would allow one to meet this requirement as the light is confined in the fiber core and can maintain high intensity over long distance of propagation. Moreover, the optical fiber design would promise better heat dissipation due to its large surface to volume ratio, which can ensure better thermal stability of the generated beams and the use of higher operating intensity levels, in addition to higher cross section emissions (in case of lasers).

Although unrelated to second-order nonlinearities, it is worth mentioning, for completion, that crystalline materials are also employed as hosts for rare-earth ions (and transition metal ions), which provide better lasing properties compared to glasses (in general). BGO and BSO were previously studied as rare-earth ions host [76]–[78]

and showed that they could potentially be used for lasing applications. Plus, they would benefit from the optical fiber design for the reasons mentioned above. Additionally, BGO and BSO crystals are good scintillators and they can be used in optical fibers as gamma- and x-rays detection devices [79], [80].

I.3.3. Third-order nonlinear effects in optical fibers and their applications

A wide variety of nonlinear effects are commonly found in a medium exhibiting third-order nonlinearities (i.e., having an intensity-dependent refractive index). Among others, Self Phase Modulation (SPM), Four Wave Mixing (FWM), and Cross Phase Modulation (XPM) are perhaps the most common (elastic) effects (for their derivations from nonlinear equations, see Ref. [69]).

Briefly, SPM is a nonlinear effect that gives rise to the phase shift of a light wave pulse when this latter is sent through a nonlinear optical medium (such as an optical fiber). The nonlinear phase shift, $\Delta\Phi$, originates from the change of refractive index of the medium induced by the nonlinear refractive index n_2 such that $\Delta\Phi = 2\pi n_2 P_0 L_{eff}/\lambda_0 A_{eff} = \gamma P_0 L_{eff}$, where P_0 is the peak power and L_{eff} is the effective length of the medium [69]. It is seen that SPM is more effective where the medium is of long length, such as in an optical fiber waveguide. Thus, the optical wave modifies its own phase (hence the "SPM" notation) and will lead to the spectral broadening of the pulse as it propagates along a fiber. As an example, SPM effect in nonlinear optical fibers can be used (in junction with the use of a Mach-Zehnder interferometer) for fast optical switching to reroute signal streams within an optical network with very high speed. It can also be used for all-optical regeneration of optical signals in optical networks (i.e., reset the original shape of a signal that was degraded during

transmission propagation in the fiber). SPM can also be combined with the anomalous dispersion regime of an optical fiber to propagate a light pulse as an optical soliton stationary wave, or it can be combined with the normal dispersion regime of an optical fiber to compress a light pulse [81].

XPM is a nonlinear effect arising from the coupling of two or more optical waves having different frequencies/wavelengths. As seen in Equation 1.12, the refractive index of a medium can be changed by the intensity of the light travelling through the medium, which modifies the refractive index. When two optical waves are launched into a fiber, each individual wave sees a change in refractive index of the medium not only due to its own intensity, but also due to the intensity from that of the other copropagating wave. Thus, the intensity of one wave can modulate the phase of another copropagating wave. This can be used, for example, for ultrafast optical switching (using various schemes of interferometers), for demultiplexing of optical time-division multiplexing channels (i.e., process specific wavelengths on the receiving end of an optical fiber system) or for wavelength conversion of wavelength division multiplexing channels [81].

FWM, similarly to XPM, is also a nonlinear effect arising from the coupling of two or more optical waves having different frequencies/wavelengths. However, this effect leads to the interaction between optical waves of different frequencies to generate new optical frequencies such that energy and momentum are conserved during the process. Two cases are found. One case where three photons of the same frequency can be annihilated to create one photon of a new frequency, which is known as third-harmonic generation. Similarly to the second-harmonic generation described in the

above section I.3.2, phase matching conditions are required and are difficult to satisfy. In the other case, two photons of different frequencies ω_1 and ω_2 can be annihilated to create two photons of frequencies ω_3 and ω_4. FWM can find applications, among others, for optical amplification, wavelength conversion, optical phase conjugation and supercontinuum generation [81].

As previously discussed, the various nonlinear effects experienced in optical fibers depend on the nonlinear parameter γ. In conventional silica fibers (of the type SMF-28), small value of $\gamma \sim 1$ $W^{-1}.km^{-1}$ are encountered due to the low n_2 value on the order of $2.6x10^{-20}$ $m^2.W^{-1}$. In order to take advantage of nonlinearities in such fibers, one has to employ long length of fibers (as the nonlinearities build up along the fibers' length) and/or employ high peak power sources (as the change in refractive index is light intensity dependent). Hence, for applications requiring shorter length of fibers (e.g., in data centers), there are more convenient ways to make nonlinear optical fibers. Different approaches have been utilized to make highly nonlinear optical fibers, whether based on structures (tapered fibers [82], microstructured fibers [83]) or based on materials with large n_2 such as chalcogenides [84], [85]. Bismuth oxide based glasses were also shown to exhibit large nonlinearities and are thus of interest for nonlinear applications [86]–[88]. Fabrication of bismuth oxide-based glass core optical fibers was formerly demonstrated in 2005 using a special processing route where bismuth-based glass core and glass cladding compositions were formed into a mould and multiple rod-in-tube steps were accomplished to drive down the core size area [89]. These fibers demonstrated large nonlinearities $\gamma \sim 1100$ $W^{-1}.km^{-1}$ and various nonlinear devices of great interest were demonstrated using short lengths of these fibers [90]–[97]. This showed the potential impact that bismuth-based glass core

optical fibers could have on optical fiber technologies. Nonetheless, their fabrication method was demonstrated through a rather tedious process and the studied molten core method here is believed to provide potentially a more straightforward approach.

I.4. References

[1] A. Macfarlane and G. Martin, *Glass: a world history*. The University of Chicago Press, 2002.

[2] D. Colladon, "On the reflections of a ray of light inside a parabolic liquid stream," *Comptes rendus des séances de l'Académie des Sciences de Paris*, vol. 15, pp. 800–802, 1842.

[3] "San Diego Evening Tribune," 1937.

[4] C. W. Hansell, "Picture transmission," US Patent 1,751,584, 1927.

[5] A. C. S. van Heel, "A new method of transporting optical images without aberrations," *Nature*, vol. 173, p. 39, 1954.

[6] J. Hecht, *City of Light: The Story of Fiber Optics*. Oxford University Press, Oxford, UK, 1999.

[7] A. L. Schawlow and C. H. Townes, "Masers and maser communications system," US Patent 2,929,922, 1960.

[8] N. Basov and A. Prokhorov, "Use of molecular beams for the radio-spectroscopic study of the rotational spectra of molecules," *J. Exp. Theor. Phys. USSR*, vol. 27, no. 4, pp. 431–438, 1954.

[9] N. Basov and A. Prokhorov, "Possible Methods for Obtaining Active Molecules for a Molecular Oscillator," *J. Exp. Theor. Phys. USSR*, vol. 28, no. 2, pp. 249–250, 1955.

[10] T. Maiman, "Stimulated optical radiation in ruby," *Nature*, vol. 187, pp. 493–494, 1960.

[11] A. Javan, W. R. Bennett, and D. R. Herriott, "Population inversion and continuous optical maser oscillation in a gas discharge containing a He-Ne mixture," *Phys. Rev. Lett.*, vol. 6, no. 3, pp. 106–110, 1961.

[12] C. K. Kao and G. A. Hockham, "Dielectric-fibre surface waveguides for optical frequencies," *Proc. IEEE*, vol. 113, pp. 1151–1158, 1966.

[13] J. F. Hyde, "Method of making a transparent article of silica," US Patent 2,272,342, 1942.

[14] F. P. Kapron, D. B. Keck, and R. D. Maurer, "Radiation losses in glass optical waveguides," *Appl. Phys. Lett.*, vol. 17, no. 10, pp. 423–425, 1970.

[15] D. B. Keck and A. R. Tynes, “Spectral response of low-loss optical waveguides,” *Appl. Opt.*, vol. 11, no. 7, pp. 1502–1506, 1972.

[16] D. B. Keck and R. D. Maurer, “Method of forming optical waveguide fibers,” US Patent 3,775,075, 1973.

[17] D. B. Keck, R. D. Maurer, and P. C. Schultz, “On the ultimate lower limit of attenuation in glass optical waveguides,” *Appl. Phys. Lett.*, vol. 22, no. 7, pp. 307–309, 1973.

[18] J. B. MacChesney, R. E. Jaeger, D. A. Pinnow, F. W. Ostermayer, T. C. Rich, and L. G. Van Uitert, “Low-loss silica-borosilicate-clad fiber optical waveguide,” *Appl. Phys. Lett.*, vol. 23, pp. 340–341, 973.

[19] M. Horiguchi and H. Osanai, “Spectral losses of low-OH-content optical fibres,” *Electron. Lett.*, vol. 12, no. 12, p. 310, 1976.

[20] T. Izawa, S. Sudo, and H. Hanawa, “Continuous fabrication process for high-silica fiber preforms,” *Trans. IEICE*, vol. E62, pp. 779–785, 1979.

[21] R. J. Mears, L. Reekie, I. M. Jauncey, and D. N. Payne, “Low-noise erbium-doped fibre amplifier operating at 1.54μm,” *Electron. Lett.*, vol. 23, pp. 1026–1028, 1987.

[22] R. H. Stolen, “The early years of fiber nonlinear optics,” *J. Light. Technol.*, vol. 26, no. 9, pp. 1021–1031, 2008.

[23] E. P. Ippen and R. H. Stolen, “Stimulated Brillouin scattering in optical fibers,” *Appl. Phys. Lett.*, vol. 21, no. 11, pp. 539–541, 1972.

[24] D. M. Dobkin and M. K. Zuraw, *Principles of chemical vapor deposition*. Springer Netherlands, 2003.

[25] S. R. Nagel, J. B. MacChesney, and K. L. Walker, “An Overview of the Modified Chemical Vapor Deposition (MCVD) Process and Performance,” *IEEE J. Quantum Electron.*, vol. QE-18, no. 4, pp. 459–476, 1982.

[26] M. G. Blankenship and W. Deneka, Charles, “The Outside Vapor Deposition Method of Fabricating Optical Waveguide Fibers,” *IEEE Trans. Microw. Theory Tech.*, vol. MTT-30, no. 10, pp. 1406–1411, 1982.

[27] V. Petit, A. Le Rouge, F. Béclin, H. El Hamzaoui, and L. Bigot, “Experimental Study of SiO_2 Soot Deposition using the Outside Vapor Deposition Method,” *Aerosol Sci. Technol.*, vol. 44, no. 5, pp. 388–394, 2010.

[28] G. E. Berkey, “Method of making fluorine doped optical preform and fiber and resultant articles,” US Patent 4,629,485, 1986.

[29] K. Schuster, S. Unger, C. Aichele, F. Lindner, S. Grimm, D. Litzkendorf, J. Kobelke, J. Bierlich, K. Wondraczek, and H. Bartelt, “Material and technology trends in fiber optics,” *Adv. Opt. Technol.*, vol. 3, no. 4, pp. 447–468, 2014.

[30] P. S. J. Russell, “Photonic-Crystal Fibers,” *J. Light. Technol.*, vol. 24, no. 12, pp. 4729–4749, 2006.

[31] F. Benabid, “Hollow-core photonic bandgap fibre: new light guidance for new science and technology,” *Philos. Trans. R. Soc. A Math. Phys. Eng. Sci.*, vol. 364, no. 1849, pp. 3439–3462, 2006.

[32] J. Ballato and E. Snitzer, “Fabrication of fibers with high rare-earth concentrations for Faraday isolator applications,” *Appl. Opt.*, vol. 34, no. 30, pp. 6848–6854, 1995.

[33] J. Ballato and P. Dragic, “Rethinking optical fiber: New demands, old glasses,” *J. Am. Ceram. Soc.*, vol. 96, no. 9, pp. 2675–2692, 2013.

[34] P. Dragic, T. Hawkins, P. Foy, S. Morris, and J. Ballato, “Sapphire-derived all-glass optical fibres,” *Nat. Photonics*, vol. 6, no. 9, pp. 629–635, 2012.

[35] P. D. Dragic, C. Ryan, C. J. Kucera, M. Cavillon, M. Tuggle, M. Jones, T. W. Hawkins, A. D. Yablon, R. Stolen, and J. Ballato, “Single- and few-moded lithium aluminosilicate optical fiber for athermal Brillouin strain sensing.,” *Opt. Lett.*, vol. 40, no. 21, pp. 5030–3, 2015.

[36] A. Mangognia, C. Kucera, J. Guerrier, J. Furtick, T. Hawkins, P. D. Dragic, and J. Ballato, “Spinel-derived single mode optical fiber,” *Opt. Mater. Express*, vol. 3, no. 4, p. 511, 2013.

[37] P. Dragic, C. Kucera, J. Furtick, J. Guerrier, T. Hawkins, and J. Ballato, “Brillouin spectroscopy of a novel baria-doped silica glass optical fiber,” *Opt. Express*, vol. 21, no. 9, pp. 10924–10941, 2013.

[38] M. Cavillon, J. Furtick, C. J. Kucera, C. Ryan, M. Tuggle, M. Jones, T. W. Hawkins, P. Dragic, and J. Ballato, “Brillouin Properties of a Novel Strontium Aluminosilicate Glass Optical Fiber,” *J. Light. Technol.*, vol. 34, no. 6, pp. 1435–1441, 2016.

[39] M. Cavillon, C. J. Kucera, T. . W. Hawkins, A. F. J. Runge, A. C. Peacock, P. D. Dragic, and J. Ballato, “Oxyfluoride core silica-based optical fiber with intrinsically low nonlinearities for high energy laser applications,” *J. Light. Technol.*, vol. 8724, no. c, pp. 8–13, 2017.

[40] J. Ballato, T. Hawkins, P. Foy, B. Yazgan-Kokuoz, C. McMillen, L. Burka, S. Morris, R. Stolen, and R. Rice, “Advancements in semiconductor core optical fiber,” *Opt. Fiber Technol.*, vol. 16, no. 6, pp. 399–408, 2010.

[41] H. J. Scheel and T. Fukuda, *Crystal growth technology*. Wiley Press, West Sussex, England, 2003.

[42] V. I. Chani, “Part I Introduction to Micro-Pulling-Down Method,” in T. Fukuda and V. Chani “Shaped Crystals: Growth by Micro Pulling Down Technology,” Springer-Verlag Berlin Heidelberg, 2007.

[43] J. A. Harrington, “Single-crystal fiber optics: a review,” *Proc. SPIE*, vol. 8959, p. 895902, 2014.

[44] J. Ballato, C. McMillen, T. Hawkins, P. Foy, R. Stolen, R. Rice, L. Zhu, and O. Stafsudd, "Reactive molten core fabrication of glass-clad amorphous and crystalline oxide optical fibers," *Opt. Mater. Express*, vol. 2, no. 2, p. 153, 2012.

[45] A. C. Walker, "Hydrothermal Growth of Quartz Crystals as Related to Phase Considerations," *Ind. Eng. Chem.*, vol. 46, no. 8, pp. 1670–1676, 1954.

[46] H. Jiang, H. J. Kim, G. Rooh, H. Park, S. Kim, U. Fawad, and J. Cheon, "Czochralski growth and scintillation properties of bismuth germanium silicon oxide (BGSO) single crystals," *IEEE Nucl. Sci. Symp. Conf. Rec.*, pp. 1580–1582, 2011.

[47] F. Raynal, B. Blanzat, J. P. Denis, J. Loriers, and C. Pannel, "Synthesis, characterization and optical properties of bismuth germanate doped with trivalent europium," *Mater. Res. Bull.*, vol. 11, no. 3, pp. 731–738, 1976.

[48] K. Takagi, T. Oi, T. Fukazawa, M. Ishii, and S. Akiyama, "Improvement in the scintillation conversion efficiency of $Bi_4Ge_3O_{12}$ single crystals," *J. Cryst. Growth*, vol. 52, pp. 584–587, 1981.

[49] V. Vaithianathan, S. Kumaragurubaran, P. Santhanaraghavan, N. Muralidhar, R. Kumar, A. K. Sinha, P. Ramasamy, and T. Nagarajan, "Growth and structural study of bismuth germanate single crystal and its energy resolution," *Mater. Chem. Phys.*, vol. 74, no. 2, pp. 121–125, 2002.

[50] J. B. Shim, J. H. Lee, A. Yoshikawa, M. Nikl, D. H. Yoon, and T. Fukuda, "Growth of $Bi_4Ge_3O_{12}$ single crystal by the micro-pulling-down method from bismuth rich composition," *J. Cryst. Growth*, vol. 243, no. 1, pp. 157–163, 2002.

[51] V. Chani, K. Lebbou, B. Hautefeuille, O. Tillement, and J. M. Fourmigue, "Evaporation induced diameter control in fiber crystal growth by micro-pulling-down technique: $Bi_4Ge_3O_{12}$," *Crystal Research and Technology*, vol. 41, no. 10. pp. 972–978, 2006.

[52] C. D. Nie, S. Bera, and J. A. Harrington, "Growth of single-crystal YAG fiber optics," *Opt. Express*, vol. 24, no. 14, p. 15522, 2016.

[53] J. Ballato, T. Hawkins, P. Foy, R. Stolen, B. Kokuoz, M. Ellison, C. McMillen, J. Reppert, A. M. Rao, M. Daw, S. R. Sharma, R. Shori, O. Stafsudd, R. R. Rice, and D. R. Powers, "Silicon optical fiber," *Opt. Express*, vol. 16, no. 23, pp. 18675–18683, 2008.

[54] J. Ballato, T. Hawkins, P. Foy, B. Yazgan-Kokuoz, R. Stolen, C. McMillen, N. K. Hon, B. Jalali, and R. Rice, "Glass-clad single-crystal germanium optical fiber," *Opt. Express*, vol. 17, no. 10, pp. 8029–8035, 2009.

[55] F. H. El Batal, "Gamma ray interaction with bismuth silicate glasses," *Nucl. Instruments Methods Phys. Res. Sect. B Beam Interact. with Mater. Atoms*, vol. 254, no. 2, pp. 243–253, 2007.

[56] D. A. Coucheron, M. Fokine, N. Patil, D. W. Breiby, O. T. Buset, N. Healy, A. C. Peacock, T. Hawkins, M. Jones, J. Ballato, and U. J. Gibson, "Laser recrystallization and inscription of compositional microstructures in crystalline SiGe-core fibres," *Nat. Commun.*, vol. 7, p. 13265, 2016.

[57] P. A. Franken, A. E. Hill, C. W. Peters, and G. Weinreich, “Generation of optical harmonics,” *Phys. Rev. Lett.*, vol. 7, no. 4, pp. 118–119, 1961.

[58] F. Pockels, “Ueber den Einfluss des elektrostatischen feldes auf das optische verhalten piezoelektrischer krystalle (On the influence of the electrostatic field on the optical behavior of piezoelectric crystals),” *Abhandlungen der Gesellschaft der Wissenschaften zu Gottingen*, vol. 39, pp. 1–204, 1893.

[59] J. Kerr, “A new relation between electricity and light: Dielectrified media birefringent,” *London, Edinburgh Dublin Philos. Mag. J. Sci.*, vol. 50, no. 332, pp. 337–348, 1875.

[60] R. H. Stolen, J. E. Bjorkholm, and A. Ashkin, “Phase-matched three-wave mixing in silica fiber optical waveguides,” *Appl. Phys. Lett.*, vol. 24, pp. 308–310, 1974.

[61] R. H. Stolen, “Phase-Matched-Stimulated Four-Photon Mixing in Silica-Fiber Waveguides,” *IEEE J. Quantum Electron.*, vol. 11, no. 3, pp. 100–103, 1975.

[62] A. Kobyakov, M. Sauer, and D. Chowdhury, “Stimulated Brillouin scattering in optical fibers,” *Adv. Opt. Photonics*, vol. 2, pp. 1–59, 2010.

[63] S. O. Kasap, *Principles of electronic materials and devices*, Third edition. McGraw-Hill, New York, NY, 2006.

[64] N. W. Grimes and R. W. Grimes, “Analysis of oxide dielectric data and the quantum theory of atomic polarizability,” *J. Phys. Condens. Matter*, vol. 9, pp. 6737–6747, 1997.

[65] R. Boyd, *Nonlinear optics*, Third edition. Academic Press, 2008.

[66] R. A. Myers, N. Mukherjee, and S. R. J. Brueck, “Large second-order nonlinearity in poled fused silica,” *Opt. Lett.*, vol. 16, no. 22, pp. 1732–1734, 1991.

[67] IEEE, “An American National Standard IEEE Standard Definitions of Terms Associated with Ferroelectric and Related Materials,” *IEEE Trans. Ultrason. Ferroelectr. Freq. Control*, vol. 50, no. 12, pp. 1–32, 2003.

[68] V. Dimitrov and S. Sakka, “Linear and nonlinear optical properties of simple oxides. II,” *J. Appl. Phys.*, vol. 79, no. 3, p. 1741, 1996.

[69] G. Agrawal, *Nonlinear fiber optics*, Fifth edition. Academic Press, New York, NY, 2013.

[70] F. Agullo-Lopez, J. Cabrera, and F. Agullo-Rueda, *Electrooptics: Phenomena, Materials and Applications*. Academic Press, San Diego, CA, 1994.

[71] D. P. Bortfeld and H. Meier, “Refractive indices and electro- optic coefficients of the eulitities $Bi_4Ge_3O_{12}$ and $Bi_4Si_3O_{12}$,” *J. Appl. Phys.*, vol. 43, no. 12, pp. 5110–5111, 1972.

[72] S. Wildermuth, K. Bohnert, H. Brändle, J. M. Fourmigue, and D. Perrodin, “Growth and characterization of single crystalline $Bi_4Ge_3O_{12}$ fibers for electrooptic high voltage sensors,” *J. Sensors*, vol. 2013, pp. 1–7, 2013.

[73] K. Bohnert, P. Gabus, and H. Brändle, “Fiber-Optic Current and Voltage Sensors for High-Voltage Substations,” *16th Int. Conf. Opt. Fiber Sensors*, pp. 752–754, 2003.

[74] K. Bohnert and J. Nehring, “Method and device for the optical determination of a physical quantity,” US Patent 5,715,058, 1998.

[75] K. Bohnert, A. Frank, and H. Brändle, “Optical high voltage sensor,” US Patent 8,233,754, 2012.

[76] L. F. Johnson and A. A. Ballman, “Coherent emission from rare earth ions in electro-optic crystals,” *J. Appl. Phys.*, vol. 40, no. 1, pp. 297–302, 1969.

[77] A. Lira, I. Camarillo, E. Camarillo, F. Ramos, and M. Flores, “Spectroscopic characterization of Er^{3+} transitions in $Bi_4Si_3O_{12}$,” *J. Phys. Condens. Matter*, vol. 16, pp. 5925–5936, 2004.

[78] G. A. Kumar, R. E. Riman, A. A. Kaminskii, R. Praveena, C. K. Jayasankar, I. K. Bae, S. C. Chae, and Y. N. Jang, “Optical properties of single crystal Nd^{3+} -doped $Bi_4Ge_3O_{12}$: Laser transitions at room and low temperature,” *Phys. Rev. B*, vol. 74, no. 1, p. 14306, 2006.

[79] M. Ishii, K. Harada, Y. Hirose, N. Senguttuvan, M. Kobayashi, I. Yamaga, H. Ueno, K. Miwa, F. Shiji, F. Yiting, M. Nikl, and X. Q. Feng, “Development of BSO ($Bi_4Si_3O_{12}$) crystal for radiation detector,” *Opt. Mater.*, vol. 19, no. 1, pp. 201–212, 2002.

[80] C. N. Holmes, “International Workshop on Bismuth Germanate,” in *Proceedings of the International Workshop on Bismuth Germanate*, 1982, p. 402.

[81] G. Agrawal, “Nonlinear Fiber Optics and its Applications in Optical Signal Processing,” *Institute of Optics University of Rochester, Rochester, NY*. pp. 1–44, 2007.

[82] F. Lu and W. Knox, “Generation of a broadband continuum with high spectral coherence in tapered single-mode optical fibers.,” *Opt. Express*, vol. 12, no. 2, pp. 347–353, 2004.

[83] B. Eggleton, C. Kerbage, P. Westbrook, R. Windeler, and A. Hale, “Microstructured optical fiber devices.,” *Opt. Express*, vol. 9, no. 13, pp. 698–713, 2001.

[84] G. Lenz, J. Zimmermann, T. Katsufuji, M. E. Lines, H. Y. Hwang, S. Spälter, R. E. Slusher, S.-W. Cheong, J. S. Sanghera, and I. D. Aggarwal, “Large Kerr effect in bulk Se-based chalcogenide glasses,” *Opt. Lett.*, vol. 25, no. 4, pp. 254–256, 2000.

[85] R. E. Slusher, G. Lenz, J. Hodelin, J. Sanghera, L. B. Shaw, and I. D. Aggarwal, “Large Raman gain and nonlinear phase shifts in high-purity As_2Se_3 chalcogenide fibers,” *J. Opt. Soc. Am. B*, vol. 21, no. 6, pp. 1146–1155, 2004.

[86] N. Sugimoto, H. Kanbara, S. Fujiwara, K. Tanaka, and K. Hirao, “Ultrafast response of third-order optical nonlinearity in glasses containing Bi_2O_3.,” *Opt. Lett.*, vol. 21, no. 20, pp. 1637–1639, 1996.

[87] N. Sugimoto, H. Kanbara, S. Fujiwara, K. Tanaka, Y. Shimizugawa, and K. Hirao, "Third-order optical nonlinearities and their ultrafast response in Bi_2O_3–B_2O_3–SiO_2 glasses," *J. Opt. Soc. Am. B*, vol. 16, no. 11, p. 1904, 1999.

[88] N. Sugimoto, T. Nagashima, T. Hasegawa, and S. Ohara, "Bismuth-based optical fiber with nonlinear coefficient of 1360 W^{-1}/km^{-1}," *Opt. Fiber Commun. Conf. 2004. OFC 2004*, vol. 2, pp. 5–7, 2004.

[89] T. Nagashima, N. Sugimoto, S. Ohara, and T. Hasegawa, "Non-lead optical glass and optical fiber," US Patent 7,524,781, 2009.

[90] J. H. Lee, K. Kikuchi, T. Nagashima, T. Hasegawa, S. Ohara, and N. Sugimoto, "All fiber-based 160-Gbit/s add/drop multiplexer incorporating a 1-m-long Bismuth Oxide-based ultra-high nonlinearity fiber," *Opt. Express*, vol. 13, no. 18, p. 6864, 2005.

[91] G. Meloni, A. Bogoni, L. Potì, C. Scuola, S. Sant, and V. Moruzzi, "Real-time ps-resolution optical sampler based on XPM-induced polarization rotation in 1-meter-long bismuth oxide fibre," in *ECOC 2005 Proceedings*, 2005, vol. 1, pp. 63–64.

[92] J. T. Gopinath, H. M. Shen, H. Sotobayashi, E. P. Ippen, T. Hasegawa, T. Nagashima, and N. Sugimoto, "Highly nonlinear bismuth-oxide fiber for supercontinuum generation and femtosecond pulse compression," *J. Light. Technol.*, vol. 23, no. 11, pp. 3591–3596, 2005.

[93] J. H. Lee, T. Tanemura, K. Kikuchi, T. Nagashima, T. Hasegawa, S. Ohara, and N. Sugimoto, "Use of 1-m Bi_2O_3 nonlinear fiber for 160-Gbit/s optical time-division demultiplexing based on polarization rotation and a wavelength shift induced by cross-phase modulation," *Opt. Lett.*, vol. 30, no. 11, p. 1267, 2005.

[94] G. Meloni, M. Scaffardi, P. Ghelfi, A. Bogoni, L. Potì, and N. Calabretta, "Ultrafast all-optical ADD-DROP multiplexer based on 1-m-long bismuth oxide-based highly nonlinear fiber," *IEEE Photonics Technol. Lett.*, vol. 17, no. 12, pp. 2661–2663, 2005.

[95] J. H. Lee, T. Nagashima, T. Hasegawa, S. Ohara, N. Sugimoto, and K. Kikuchi, "Bismuth-oxide-based nonlinear fiber with a high SBS threshold and its application to four-wave-mixing wavelength conversion using a pure continuous-wave pump," *J. Light. Technol.*, vol. 24, no. 1, pp. 22–27, 2006.

[96] R. Salem, A. S. Lenihan, G. M. Carter, and T. E. Murphy, "160-Gb/s polarization-independent optical demultiplexing in 2-m nonlinear fiber," *IEEE Photonics Technol. Lett.*, vol. 18, no. 21, pp. 2245–2247, 2006.

[97] F. Parmigiani, S. Asimakis, N. Sugimoto, F. Koizumi, P. Petropoulos, and D. J. Richardson, "2R regenerator based on a 2-m-long highly nonlinear bismuth oxide fiber," *Opt. Express*, vol. 14, no. 12, pp. 5038–44, 2006.

CHAPTER II

INVESTIGATION OF THE FABRICATION OF BISMUTH GERMANIUM OXIDE $Bi_4Ge_3O_{12}$ (BGO) CRYSTALLINE FIBERS VIA THE MOLTEN CORE METHOD

This chapter focuses on the growth of BGO single crystalline core fibers fabricated using the molten core method. For this purpose, two experimental designs were considered and they will be described in the first section. Next, details about the materials and methods used will be reported in a second section. Then, the results will be gathered and discussed in a third section. Finally, a conclusion will be given in the last section, summarizing the obtained results.

As a reminder, based on the discussions of Chapter I, interest in crystalline BGO core optical fibers stems from the material's acentric crystal structure, which would afford useful fiber-based electric field sensors. In this specific Chapter, the use of the molten core approach to fabricate complex oxide crystalline fibers are explored to develop a fundamental understanding of the chemical interplay between the molten BGO core phase and the SiO_2 glass cladding.

II.1. Experimental designs

The first exploratory design employed the drawing of a BGO single crystal sleeved inside a borosilicate glass cladding. This experiment was performed to understand the crystal interaction with the glass cladding. An additional experiment was performed in static conditions (i.e., in a furnace) to better understand this interaction and can be found in Appendix A.

The second design explored the use of a core with a BGO single crystal surrounded by Bi_2O_3 powder (Figure II-1). The purpose of the Bi_2O_3 powder was to retain a higher amount of Bi_2O_3 in the core that could help in obtaining a single phase core. An additional draw was performed and employed a tuned surrounding powder composition (in the Bi_2O_3-GeO_2 system) to study the retention of GeO_2 content in the crystalline core and can be found in Appendix A.

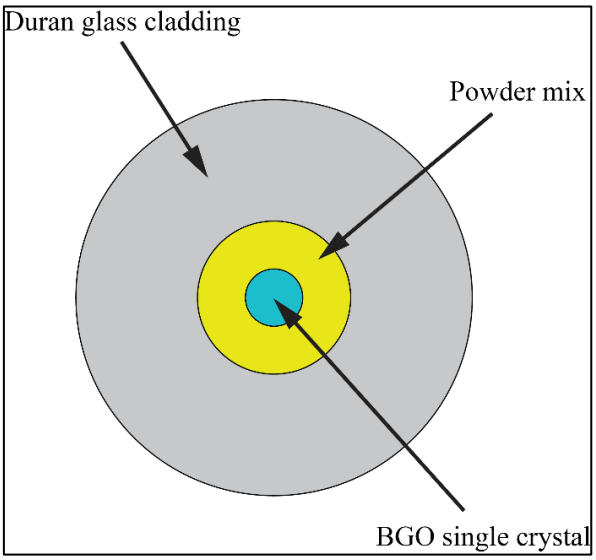

Figure II-1. Schematic of the second experimental design. The BGO single crystal (blue) is surrounded by a powder mix (yellow) and sleeved into the DURAN® glass cladding (grey). The drawing is not to scale.

II.2. Materials and Methods

II.2.1. Sample preparation

First, in all experiments described in this Chapter, a borosilicate (denoted DURAN®) glass cladding tube of dimensions 3x30 mm (inner diameter x outer diameter) was used with a composition of $81SiO_2$-$13Bi_2O_3$-$4Na_2O$-$2Al_2O_3$ in wt%. The DURAN® glass cladding drawing range is 950-1080°C owed to its relatively low viscosity-temperature dependence around its softening point. DURAN® is not a particularly stable glass and so its fabrication into fiber generally requires a two-step

drawing: the preform is first drawn to a large diameter ("cane"), which is on the order of millimeters in diameter, followed by a redraw into fiber (~125 µm). This two-step processing limits crystallization on the surface of the fibers that would take place if the preform was drawn directly to fiber, which improves the mechanical properties of the drawn fibers. The second step may not be employed depending on the desired size of the sample to be investigated. Secondly, all draws involving the use of powder precursor material made use of high purity commercial powders (Alfa Aesar Puratronic® grade: Bi_2O_3, 99.9995%).

In the first experimental design, a two-centimeter-long BGO single crystal rod of 1.2 mm diameter ($T_{melting}$=1050°C) grown by Fibercryst (Fibercryst S.A.S. Co., Villeurbanne, France) using the micro-pulling down method (with the [001] crystal plane direction grown along the rod axis) was sleeved into the hollow core of a DURAN® glass preform. The preform was then drawn at 1080°C to cane with a draw speed of 0.3 $m.min^{-1}$.

In the second experimental design involving a crystal surrounded with the Bi_2O_3 powder, a same BGO single crystal rod was introduced first in the DURAN® glass preform then followed by the insertion of the powder from atop the preform. The crystal was centered in the core as much as it could be during the preform preparation. The preform was then drawn at 1080°C to cane with a draw speed of 0.3 $m.min^{-1}$.

II.2.2. Electron microscopy

A Hitachi SU-6600 Scanning Electron Microscope (SEM) with Energy-Dispersive X-ray spectroscopy (EDX) in secondary electron (SE) mode was employed to image the morphology and analyze the composition of the core. The SEM was operated with

electron beam energy of 20 kV in a variable pressure environment of 30 Pa. The working distance was about 10 mm. The canes were manually polished to a 2.5 µm finish or mechanically polished to a 0.05 µm finish. In all experiments, EDX is not able to detect boron and therefore, all compositions obtained are not true compositions, but, rather are used to provide insight into changes from the original core phase to the final fiber. Herein, all compositions are noted in mole percent (mol%). The starting crystals' structure, orientation and spatial arrangement were also investigated using the Hitachi SU-6600 SEM with an attached Oxford Instruments Electron Backscattered Diffraction (EBSD) camera. The samples were polished to a 0.05 µm mirror-like finish in a silica colloidal solution before analysis. It is important to underline that EBSD is not an accurate technique to detect (new) crystalline phases since it detects the phases that the experimenter input before the measurement is performed, which are then matched with the detected Kikuchi bands. The operating conditions were a 20 kV accelerating voltage and a working distance of 18 mm. EBSD patterns were taken with a resolution of 334 x 256 pixels.

II.2.3. Powder X-ray diffraction

In addition to EBSD, powder x-ray diffraction (PXRD) was also performed to verify the crystallinity of the obtained canes as well as to identify the phases. A Rigaku Ultima IV diffractometer was used for this purpose, employing Cu Kα radiation (λ=1.5408Å) as the x-ray source. For PXRD experiments, sections of the canes were crushed into powder using a silica mortar and pestle. The resultant powder therefore contained both cladding and core material. The scan speed was set to 0.65 deg.min^{-1} and the 2-theta scan range was set between 19° and 65°. The obtained XRD

diffractograms were analyzed using the OriginPro 8 software, and this latter was utilized to subtract baselines.

II.3. Results and discussion

II.3.1. BGO single crystal

The BGO single crystal was analyzed using SEM in order to provide a qualitative and quantitative comparison to the subsequent fiber draws. Figure II-2a illustrates the compound concentration observed across the single crystal. The theoretical composition of the $Bi_4Ge_3O_{12}$ single crystal is a ratio of $2Bi_2O_3$ for $3GeO_2$ corresponding to 60 mol% GeO_2 and 40 mol% Bi_2O_3. The experimental values found using EDX showed an average composition of 60.9 ± 0.3 mol% GeO_2 and 39.1 ± 0.3 mol% Bi_2O_3, which were close to the stoichiometric values. Nevertheless, it is interesting to note that the single crystal was grown slightly off stoichiometry by ~1 mol% Bi_2O_3, likely due to Bi_2O_3 evaporation [1]. Figure II-2b shows the PXRD of the precursor BGO single crystal used in this work. This latter was shown to match the BGO eulytine crystal structure reference in the JCPDS database [2]. Figure II-3 illustrates the X-, Y- and Z-axis inverse pole figures (IPF) orientation maps of the BGO single crystal. The crystal plane orientations were found to be [-35-2], [-6-32] and [136] in the X, Y and Z directions respectively and indicate that the single crystal was not grown along low-index crystallographic directions. These planes will serve as a reference for future draw comparison. Note that single crystallinity was demonstrated through the single color obtained in the IPF orientation maps as well as through the accurate crystal plane direction color matching in Figure II-3e.

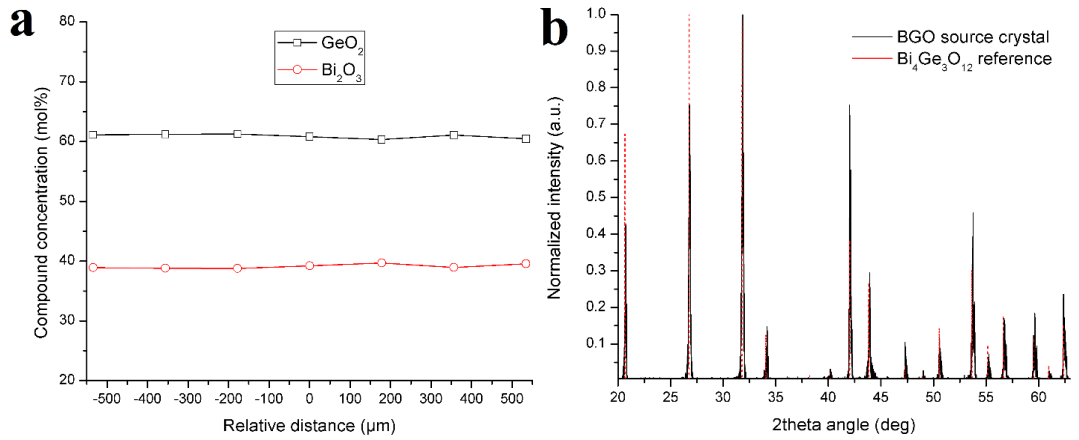

Figure II-2. (a) Compound concentration profile across the BGO single crystal rod cross section. The average concentration across the single crystal is found to be of 60.9 GeO_2 mol% and 39.1 Bi_2O_3 mol%. (b) Powder x-ray diffraction (PXRD) diffractogram of the BGO single crystal source and reference (JCPDS card #01-077-0497). The peaks were matched to the BGO eulytine crystal structure.

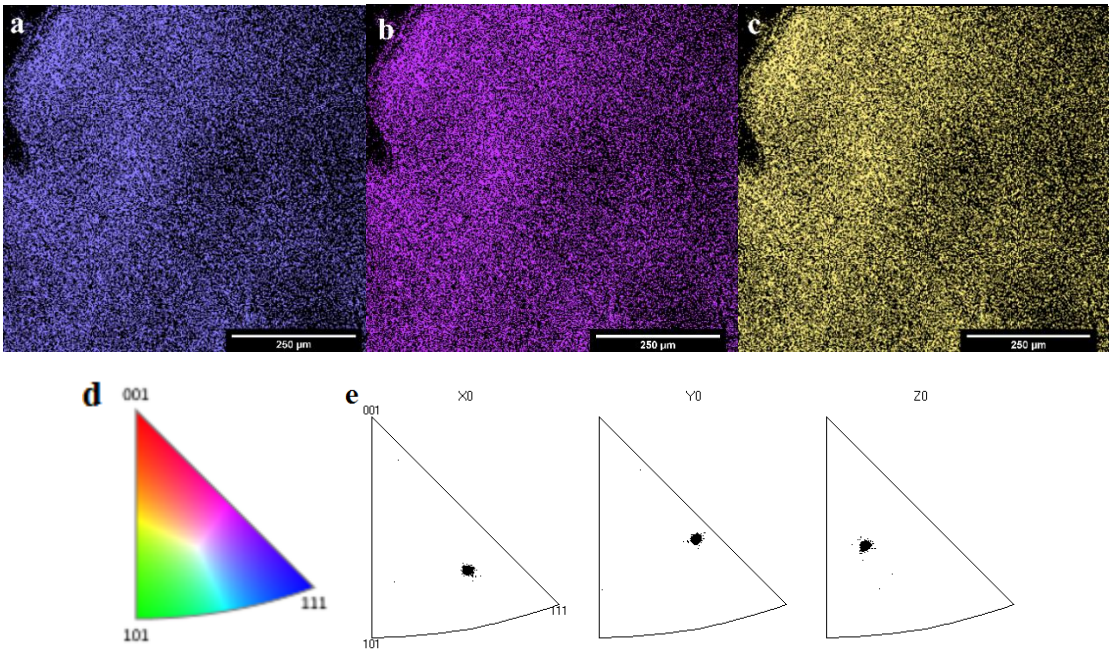

Figure II-3. IPF orientation maps of the BGO single crystal along the a) X-, b) Y- and, c) Z-axis. d) Stereographic triangle showing the orientation color-scale and, e) Color matching between each pixel in each orientation map and the orientation color-scale, showing single crystallinity.

II.3.2. First design: BGO single crystal sleeved into DURAN®

Figure II-4 depicts the obtained cane resulting from the simple sleeving of the BGO single crystal precursor inside the DURAN® borosilicate glass cladding. A

white core over a length of about four centimeters was obtained. It is interesting to note that a white color usually indicates polycrystallinity due to light scattering from the crystals. Hence, it was expected to observe crystals in the core.

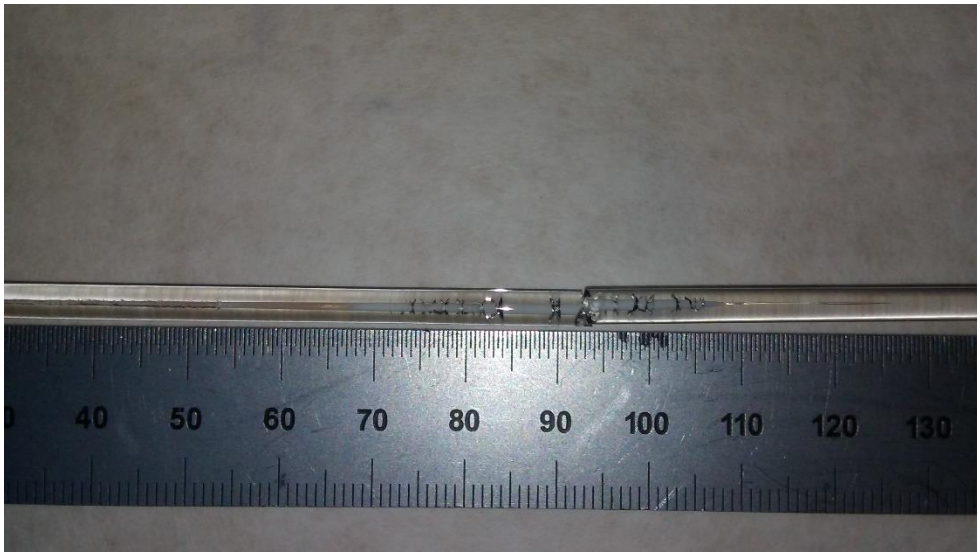

Figure II-4. Pictures of optical canes drawn using the first draw design, employing a 1.2 mm diameter BGO single crystal as precursor. The first piece of cane to be drawn is situated on the right. A white core is depicted over a length of ~4 cm. A large number of cracks was observed in the cladding surrounding the core.

A piece from the middle part of the white core cane was taken for analysis. The cane was 3.8 mm diameter and the core was 865 µm diameter. Line-like grains (such as observed by Zhang, et al. [3]) were observed at the core-cladding interface as well as dendrite-like grains (Figure II-5a); and as one moves towards the center, more uniform grains were seen (Figure II-5b). The core thus was polycrystalline and all structures were shown to be crystals of the eulytine family, as will be discussed later.

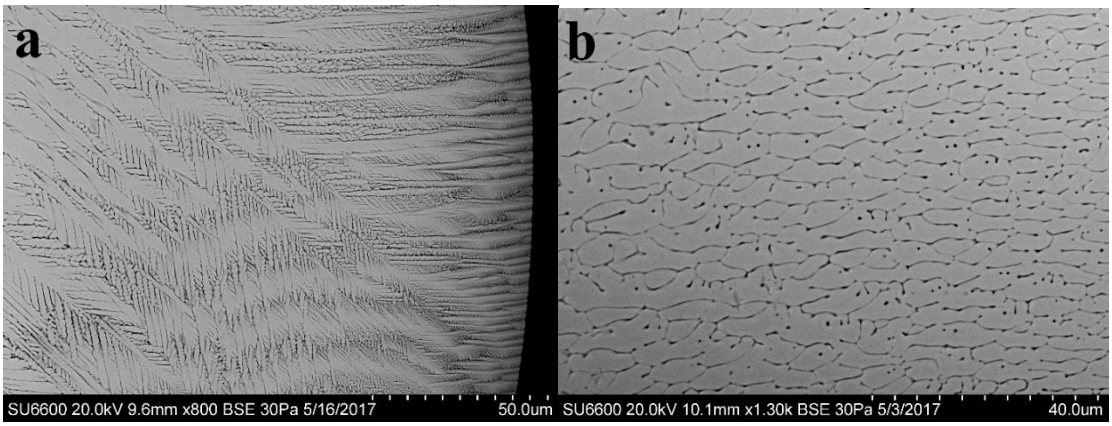

Figure II-5. (a) SEM micrograph of the core-cladding interface of the middle region of the white core cane showing large line-like and dendrite-like grains. (b) SEM micrograph of the same core but at its center demonstrating more uniform grains.

II.3.2.1. Microstructure analysis

The structures observed in the core center were seen as small grains despite the lack of well-defined grain boundaries. Shim, et al., [4] noticed the formation of grains with large grain boundaries during BGO single crystal growth using the micro-pulling down method. They attributed the formation of these grain boundaries to be a result of crystal growth from a bismuth-poor melt, induced by the well-known evaporation of the bismuth oxide precursor [5]. In the case here, the composition of the crystals was found to vary from the outer edge of the core ($40.5SiO_2$-$31.3GeO_2$-$26.2Bi_2O_3$-$0.8Al_2O_3$-$1.3Na_2O$) to the center of the core ($13.5SiO_2$-$50.6GeO_2$-$34.5Bi_2O_3$-$0.6Al_2O_3$-$0.8Na_2O$). Clearly, a modification of the initial precursor stoichiometry was noted and was attributed to the partial incorporation of species from the glass cladding into the BGO melt (i.e., dilution of all compounds) rather than the only evaporation mechanism of Bi_2O_3. Note, nonetheless, that the measured compositions are skewed due to the inability of the instrument to detect boron oxide and, also likely due to the probed interaction volume that can potentially contain both crystal and amorphous phases. Additionally, the grain boundaries were found to be bismuth-poor as can be

seen from the dark color of the SEM micrograph in Figure II-5. The crystals were thus grown from a bismuth-poor melt as the stoichiometric content (40 mol% Bi_2O_3) was not retained. Note that the presence of SiO_2 in the grain composition can be expected as the latter can substitute for GeO_2, as will be discussed in section II.3.2.2.

Although it was observed in section II.3.1 that the BGO single crystal precursor was grown from a slightly off-stoichiometric melt and was still found to be single phase, this observation likely holds only in the vicinity of the stoichiometric melt composition up to a certain limit. In the case here, in view of the large off-stoichiometry observed, the compositions from which the crystals were grown were likely exceeding that limit; yielding the various microstructures noted. Smet, et al., [6] reported BGO crystal growth from off-stoichiometric melts in the Bi_2O_3-GeO_2 system. They showed the ability of the melt to form different crystal microstructures (well-faceted, cellular and dendritic) depending on the growth rate and the composition range (60 to 25 mol% Bi_2O_3). In the case here, similar microstructures were observed to those by Smet, et al., [6] and the following explanation is offered. As the BGO single crystal precursor melts during the draw process, compounds from the glass cladding are incorporated into the core and thus, the relative Bi_2O_3 concentration is diluted in the newly formed melt. The glass cladding incorporation process takes place gradually from the core-cladding interface towards the core center and hence, a loss of stoichiometry results. Then, the Bi_2O_3 content is gradually depleted from the core center and a compositional gradient was induced in the cane cross section. As a result, different compositions were observed across the core and, thus, different microstructures were grown. Line-like and dendritic-like grains were grown where the Bi_2O_3 content was small (25-33 mol%) while small uniform grains

were grown where the Bi_2O_3 content was large (>33 mol%), which concurs with the observation of Smet, et al., [6].

Furthermore, the difference in crystal morphology can be attributed to a difference in quenching rates; also keeping with Smet, et al., [6]. They showed that crystals formed with larger quenching rates demonstrated more disordered crystal growth (such as the formation of dendrites). This indicates that the large quenching rates observed with optical fiber drawing techniques should not allow the crystal growth of homogeneous phase. Nonetheless, small uniform grains were observed in the core center, and were likely the result of a thermal gradient. The canes and fibers drawn with an optical fiber draw tower possesses an inherent thermal gradient across their cross section (despite the large quenching rates), and the core is the last part of the cane from which the heat will be extracted. In the case here, the cane diameter was on the order of millimeters and thus, there was a larger volume of material from which to extract heat compared to conventional (optical) fibers that have diameters on the order of 100 microns. Thus, the thermal gradient across the cane core was likely to be large and the core was kept at a higher temperature than its surrounding for a longer time before reaching room temperature, allowing a more homogeneous crystal growth.

It is interesting to note that material transport was shown to be the limiting mechanism for single phase formation, i.e., the amount of Bi_2O_3 available at the growth front. Indeed, the grain boundaries were observed as bismuth-poor and thus there was a lack of Bi_2O_3 in the melt to grow a single phase. The growth rate, on the other hand, was not a limiting mechanism as sufficient energy was provided for the atoms to cross the liquid-crystal interface and attach onto the on growing crystal front. This behavior correlates with the findings of Dimesso et al. [7] who pointed towards a

diffusion-limited crystallization mechanism in the crystal growth of bismuth germanate glasses.

II.3.2.2. Crystal structure analysis

Figure II-6 illustrates the PXRD diffractogram of the white core cane. The positions of the observed peaks were matched closely to that of the BGO single crystal source, confirming that the grains crystallized with the BGO crystal structure. The peaks of the white core cane were seen to exhibit a small 2-theta angle shift compared to that of the BGO single crystal source (from ~0.07° to 0.21° as one goes towards higher 2-theta degree angle). This shift likely is associated with the substitution of Si^{4+} atoms for Ge^{4+} in the grown crystals lattice. $Bi_4Ge_3O_{12}$ (BGO) and $Bi_4Si_3O_{12}$ (BSO) are both known to crystallize with the same eulytine structure and are thus isostructural, where $(SiO_4)^{4-}$ units can replace the $(GeO_4)^{4-}$ units of the BGO eulytine crystal structure [7], [8]. Furthermore, the fabrication of various $Bi_4(Ge_{1-x}Si_x)_3O_{12}$ (BGSO) compositions have been reported [7], [9], [10], confirming the ability of silicon to replace germanium. In the case here, it was observed that silicon atoms were introduced in the core melt with a compositional gradient, and hence crystals with various compositions of the form $Bi_4(Ge_{1-x}Si_x)_3O_{12}$ were likely grown. Hence, the PXRD peak shifts are associated with a continuous change in Si/Ge ratio in the core crystals. This also correlates with the findings of Xie, et al. [10], who reported a similar behavior while studying different BGSO compositions. For completeness, the cubic lattice parameters of the BSO crystal structure are 10.28 Å [11] and those of the BGO structure are 10.52 Å [2]. Hence, per Bragg's law, an increase in 2-theta angle corresponds to a decrease in lattice parameter, correlating with the findings that Ge^{4+} atoms were substituted for Si^{4+}. While Si^{4+} and Ge^{4+} atoms

have been demonstrated to substitute for each other in the eulytine crystal structure, B^{3+} (and Al^{3+}) could potentially also substitute in the crystal structure as well. Boron (and aluminum) atoms were likely to be incorporated into the core. Boron (and aluminum) is known to adopt a tetrahedrally coordinated state and could thus substitute for germanium atoms in the structure, which would reduce the lattice parameter constant (hence increase the 2-theta angle value of the peaks) similarly to silicon. Thus, the peak shifts could also originate from boron (and aluminum) substitution. Nonetheless, the substitution of germanium groups $(GeO_4)^{4-}$ with boron groups $(BO_4)^{5-}$ (and aluminum groups $(AlO_4)^{5-}$) would introduce a charge imbalance that needs to be compensated for by bismuth cation substitution. The necessity for charge compensation was mentioned by Durif-Varambon [7], and thus a tetravalent atoms would be necessary to balance the charges following the substitution scheme: $4Bi^{3+} + 3(SiO_4)^{4-} = 3M^{4+} + Bi^{3+} + 3(BO_4)^{5-}$. In the case treated here, silicon is the only tetravalent ions introduced from the glass cladding that could satisfy the substitution scheme. However, the ionic radius of silicon ion (r_{Si}= 0.26 Å) is much smaller than that of bismuth ion (r_{Bi}= 1.03 Å) and it is thus unlikely that silicon will replace bismuth. Hence, it is unlikely that boron (and aluminum) was substituted in the eulytine crystal structure. Although boron and bismuth have the same valence state, the boron atom is much smaller (r_B= 0.03 Å) than the bismuth atom and is unlikely to replace this latter. Note that, while the substitution scheme seems unlikely based on the arguments laid down by Durif-Varambon, it is not impossible that boron (and aluminum) could be introduced in the crystal structure through an interstitial mechanism. It is worth noting that the glass cladding incorporation inherent to the

molten core method was not shown to be an impediment to crystal growth and that it could be used to one's advantage to tune the crystal core phase.

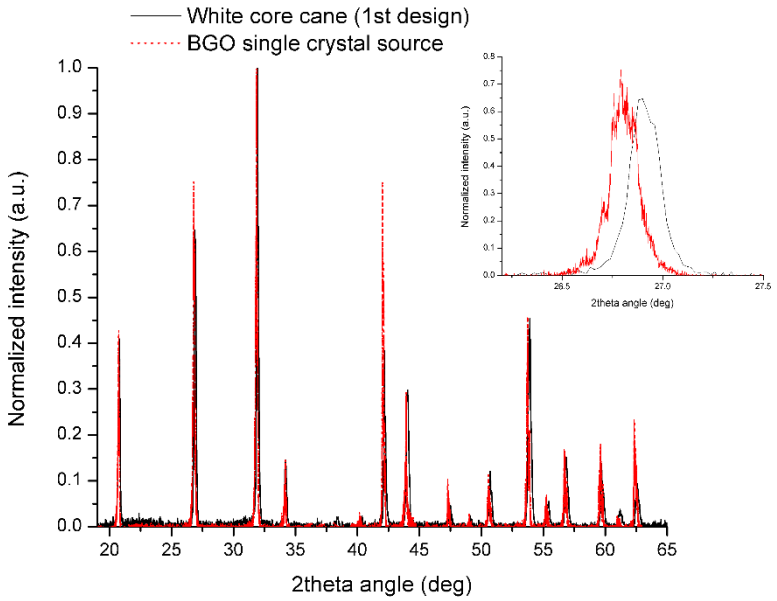

Figure II-6. PXRD diffractogram of the white core cane resulting from a BGO single crystal drawn inside the DURAN® borosilicate glass cladding (1st design). The crystalline peaks were closely matched to that of eulytine crystal structure. Small 2-theta angle shifts were observed compared to the BGO single crystal source and indicated that crystals grew from composition richer in SiO_2 than GeO_2. The inset shows a magnification of the peak at 26.8° for clarity.

The crystal plane orientations of the grains were also investigated using EBSD analysis. Figure II-7 depicts the IPF orientation maps along the X, Y and Z axis. Crystals were found to grow along one single orientation as seen from the single color obtained in each direction. The crystal plane orientations were found to be [-461], [-6-41] and [106] in the X, Y and Z directions respectively. These crystal plane orientations were seen to differ from those observed for the BGO single crystal source indicating that crystal growth occurred from a random plane. In addition, these planes do not seem to indicate that crystal growth took place from low-index crystallographic directions (such as [100] or [110] or [111]). It is interesting to note that even though the core was found polycrystalline in terms of

microstructure, each crystal was grown along the same direction, indicating that the core was single crystal-like.

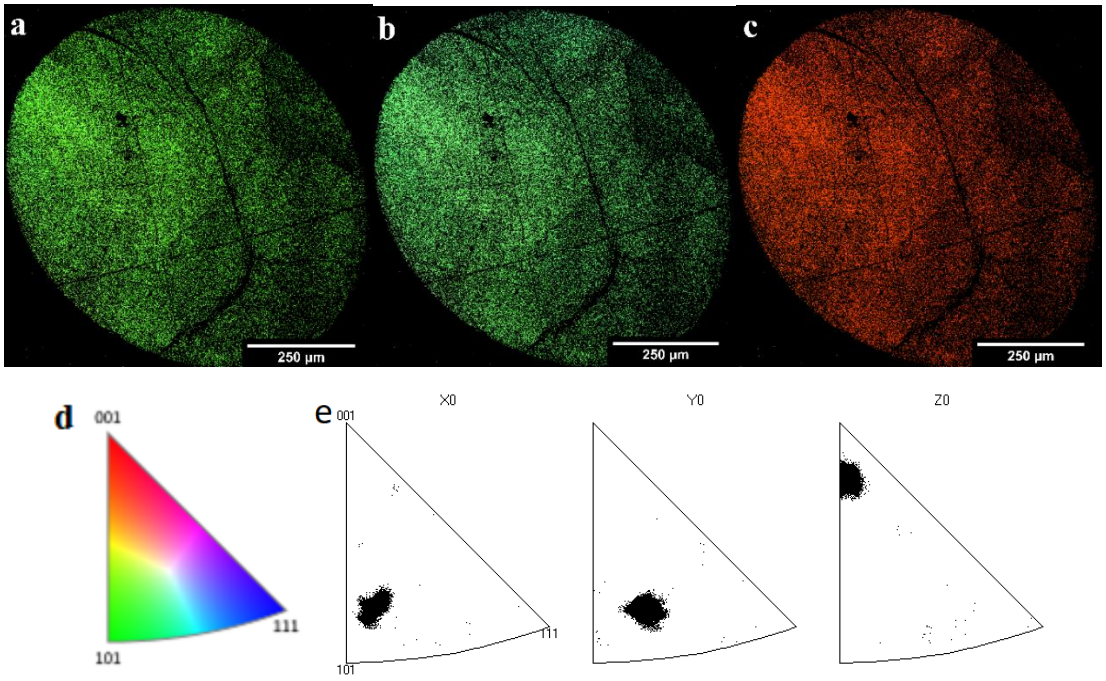

Figure II-7. IPF orientation maps along the a) X-, b) Y- and, c) Z-axis for the white core cane drawn using the first design. d) Stereographic triangle showing the orientation color scale and, e) Color matching between each pixel of the IPF orientation map and the orientation color-scale, showing heavy preferred crystal orientation along each axis (i.e., single crystal-like).

II.3.3. Second design: BGO single crystal surrounded by Bi_2O_3 powder

As was observed previously with the first design, the Bi_2O_3 core content was found to be below the BGO (or BGSO) stoichiometric value, which prevented the growth of a single microstructural phase. This second design investigated in this section explored the use of additional Bi_2O_3 around the BGO single crystal to better preserve the stoichiometry. The concept was to use the material incorporation to one's advantage and have the surrounding Bi_2O_3 melt incorporated in the BGO single crystal melt to increase the Bi_2O_3 melt content. This could, in turn, lead to a closer stoichiometric BGSO melt and hence a single phase core.

II.3.3.1. Microstructure analysis

A white core cane of 1.5 cm length was observed with a cladding diameter of 3.8 mm. Figure II-8 provides the SEM micrograph of the resultant white core cane cross-section whose core diameter was 1.02 mm. The observed cracks in the core originated from the coefficient of thermal expansion (CTE) mismatch between the crystal core and the glass cladding. The CTE of the BGO crystal is ~$63x10^{-7}$ K^{-1} [12] and that of the glass cladding is ~$33x10^{-7}$ K^{-1} [13]. Hence, stresses were likely built upon cooling and the core that was in tension was released the stresses upon cleaving/polishing the cane. Large uniform grains were observed in the core center while single phase regions were noticed in the periphery of the core center. One notes that neither dendrite-like nor line-like grains were observed in the core, which are structures known to form from a large off-stoichiometric melt [6] as discussed above in section II.3.2.1. This demonstrates that the grains were grown from a melt possessing a closer stoichiometry to that of BGO, and that the Bi_2O_3 content in the core melt was effectively raised. This is additionally supported by the findings that the grain boundaries were now Bi_2O_3-rich (48 to 57 mol% as one moves towards the core center), indicating crystal growth from a bismuth-rich melt. Hence, the Bi_2O_3 powder surrounding the BGO single crystal melt was effectively incorporated into the latter and allowed for the formation of a core microstructure closer to a single phase. It is interesting to note that in this case the thermal gradient across the core was not shown to affect the core microstructures. Thus, the core microstructures observed in the 1st design solely originated from the variation in composition across the core.

It is worth noting that the EDX results showed that the composition of the grains varied from the outer edge of the core (22.2SiO_2-46.8GeO_2-29.0Bi_2O_3-0.7Al_2O_3-

1.4Na_2O) to the center of the core (13.7SiO_2-50.6GeO_2-34.1Bi_2O_3-0.6Al_2O_3-1.0Na_2O), a trend that was also observed in the first experiment. One notes that the values at the outer edge of the core represent a larger amount of GeO_2 and lower amount of SiO_2 compared to that in the 1st design experiment, indicating that the glass cladding incorporation was reduced. This can be explained by the Bi_2O_3 powder acting as a "buffer" between the glass cladding and the BGO crystal melt. Perhaps the difference in chemical potentials and viscosities between the glass cladding and the Bi_2O_3 melt reduced the magnitude of interaction between the BGO single crystal and the glass cladding.

Interestingly, it was noted that the concentration at core center was similar to that obtained with the 1st design experiment and thus does not give a significant increase of Bi_2O_3 content in the crystal grains despite the more homogeneous (and single) phase obtained here. As discussed in the previous paragraph, the microstructures clearly implied that crystal growth in the core took place from a composition closer to the BGO stoichiometry. Perhaps, the EDX values were skewed due to the inability of the instrument to detect boron oxide. The latter is found in a non-negligible amount in the glass cladding (~11 mol%) and was certainly incorporated into the core during drawing. Hence, it is unknown which element the boron would substitute for in the composition and this makes the EDX analysis less reliable.

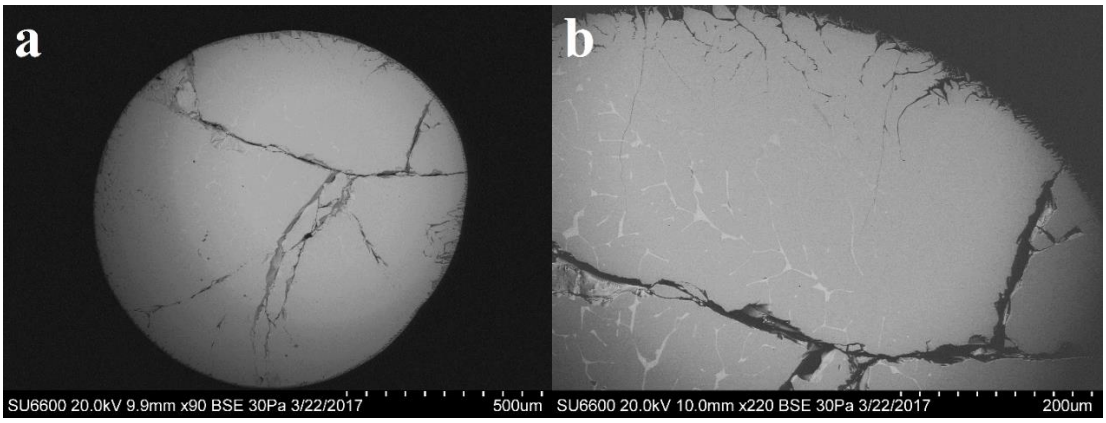

Figure II-8. (a) SEM micrograph of the core cane cross-section resulting from a BGO single crystal surrounded by Bi_2O_3 powder drawn inside the DURAN® borosilicate glass cladding (2nd design). (b) SEM micrograph of the same core at higher magnification, showing the presence of large uniform grains with single phase region.

II.3.3.2. Crystal structure analysis

Figure II-9 provides the PXRD diffractogram performed on the same white core cane. The positions of the observed peaks were matched closely to that of the BGO single crystal source, confirming that the grains crystallized with the eulytine crystal structure. It was noted that the peaks were shifted to large 2-theta degree angles (from ~0.2° to ~1.0° as one goes towards higher 2-theta degree angle) compared to the BGO single crystal source. Similar to the 1st design experiment, the shift likely originated from the substitution of silicon for germanium in the eulytine structure. It is worth noting that in this case (2nd design) the peaks were shifted to larger 2-theta degree angles than in the 1st design experiment, indicating that a larger amount of glass compounds was incorporated in the grown crystal. The peak shift differences observed from JCPDS cards between BGO [2] and BSO [11] crystals in the studied 2-theta angle range vary from ~0.2° to ~1.7° as one goes towards higher 2-theta degree angle. Knowing that BGSO solid solutions exists over the whole composition range [7], one can calculate the silica content incorporated in the eulytine structure using the

peak shifts. This can be done assuming that the difference in 2-theta angle peak positions between BSO and BGO correspond to a full silica substitution from germania (i.e., a full peak shift from BGO to BSO corresponds to 60 mol% SiO_2 in the BGO crystal). For example, BGO crystal possess a peak at 20.73° while the similar BSO crystal peak is found at 21.16°. The difference between these two peaks (0.43°) is then assumed to correspond to a full silica substitution from germania (i.e., 60 mol% SiO_2). Then, assuming linearity between peak shift and silica content, one can calculate the (theoretical) silica content substitution from the various peak shifts observed in the PXRD diffractogram. Calculations of the silica content derived from this method are gathered in Table II-1. The silica content was calculated from the shift of the four main peaks observed in Figure II-9. Note that the peaks exhibited a "continuum" in peak shifts, hence the lower and upper values in peak shift in Table II-1. The averaged silica content calculated from the lower peaks shift was found to be 23.1 ± 2.7 mol% and that from the upper value of the peak shift was found to exceed the theoretical 60 mol% SiO_2 substitution. In comparison, the silica content value obtained by EDX on crystals at core center was of 13.7 mol% and that on crystals at the core-clad interface was of 22.2 mol%. Although the calculated silica content was shown to overlap with the EDX values of the core-clad interface, there are uncertainties on the calculated silica content values from the peak shifts as these latter could vary significantly as seen in Table II-1. The exceeding theoretical silica substitution values calculated from the upper value of the peak shift may indicate that other atoms such as boron and aluminum were substituted and/or inserted in the lattice. Clearly, further studies on elemental substitution (B, Al, Na) in the eulytine structure would be necessary to confirm this.

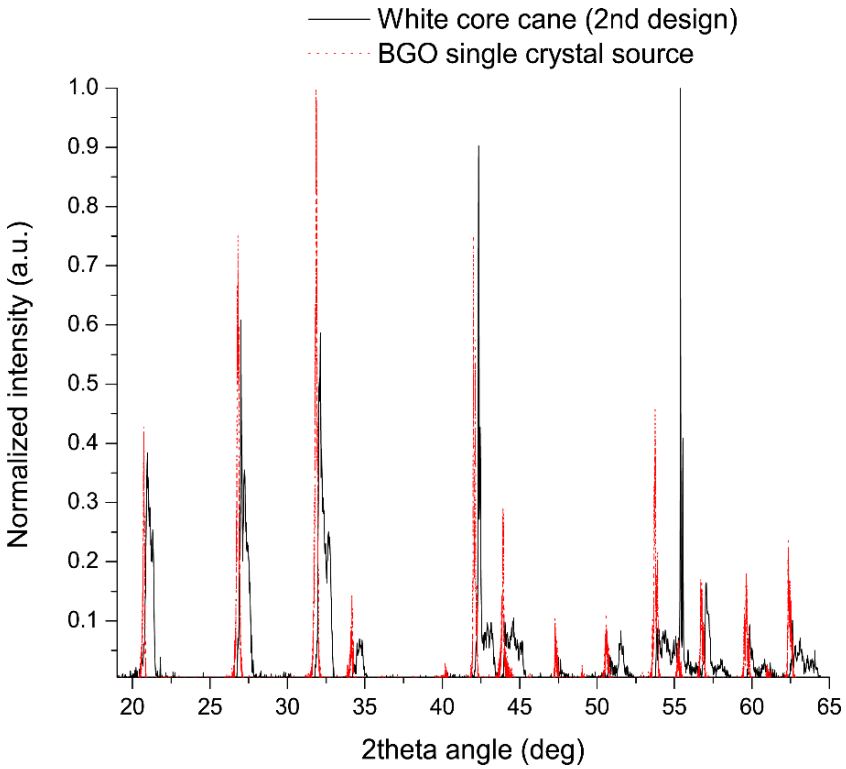

Figure II-9. PXRD diffractogram of the core cane resulting from a BGO single crystal surrounded by Bi_2O_3 powder drawn inside the DURAN® borosilicate glass cladding. The crystalline peaks were matched to that of eulytine crystal structure. Large 2-theta angle shifts were observed compared to the BGO single crystal source and indicated that crystals grew from composition richer in SiO_2 than GeO_2.

Table II-1. 2-theta angle peak values of the BGO crystal source and BSO crystal (JCPDS 01-080-1596) and peak shifts in the PXRD diffractogram (Figure II-9) used to derive the silica content in the grown BGSO crystals (2nd design).

BGO source crystal 2-theta angle (deg)	BSO card 2-theta angle (deg)	Peak shift (deg)	Peak shift in Figure II-9	Derived SiO_2 content (mol%)
20.73	21.16	0.43	0.22 - 0.61	30.7 - >60
26.80	27.42	0.62	0.20 - 0.81	19.0 - >60
31.86	32.57	0.71	0.18 - 0.88	22.0 - >60
42.13	43.08	0.95	0.33 – 1.23	20.8 - >60

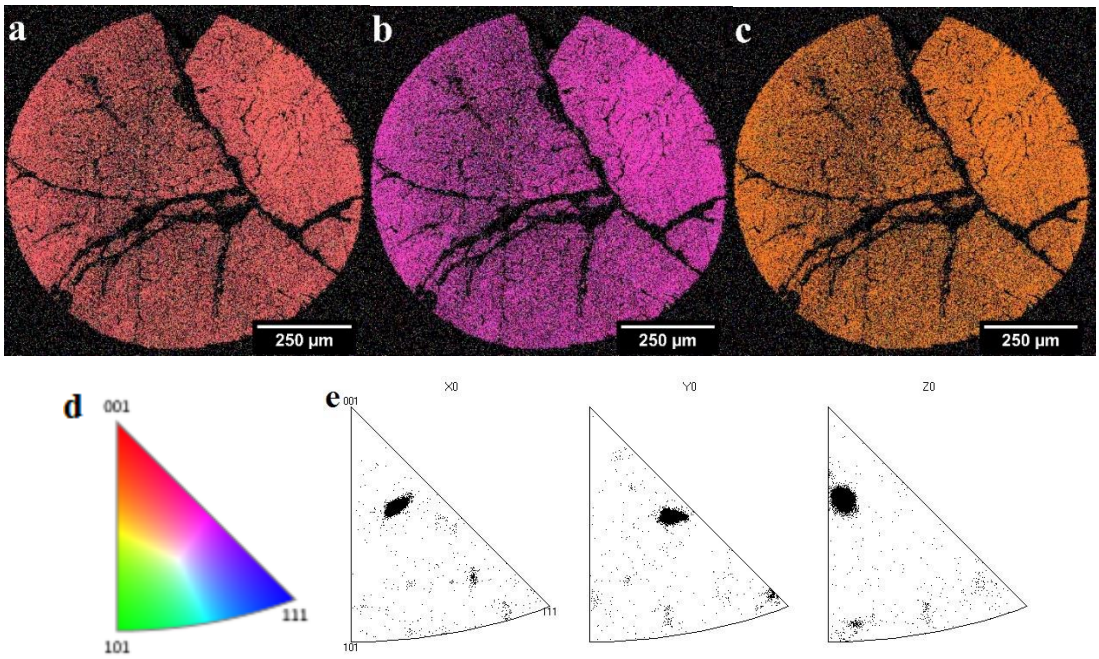

Figure II-10. IPF orientation maps along the a) X-, b) Y- and, c) Z-axis for the white core cane drawn using the second design. d) Stereographic triangle showing the orientation color scale and, e) Color matching between each pixel of the IPF orientation map and the orientation color-scale, showing heavy preferred crystal orientation along each axis (i.e., single crystal-like).

The crystal plane orientations of the grains were investigated using EBSD analysis. Figure II-10 depicts the IPF orientation maps along the X, Y and Z axis. Crystals were found to grow along one single orientation as seen from the single color obtained in each direction. The crystal plane orientations were found to be [26-1], [-311] and [103] in the X, Y and Z directions respectively. Similarly to the core crystal planes observed in the previous drawn cane in section II.3.2.2, these crystal plane orientations were seen to be different from those observed for the BGO single crystal source indicating that crystal growth occurred from a random plane. Plus, these planes do not seem to indicate that crystal growth took place from low-index crystallographic directions (such as [100] or [110] or [111]). It is interesting to note, once again, that even though the core was found polycrystalline in terms of microstructure, each

crystal was grown along the same direction demonstrating that the core was single crystal-like.

Perhaps the most intriguing observation from both experiments was the melt crystallizing to the same eulytine structure as BGO. The BGO single crystal melted during the draws and interacted with the glass cladding, thus leaving a non-stoichiometric melt in the core. Nonetheless, BGO single crystals have not been reported to form spontaneously from a melt and researchers mentioned that BGO cannot nucleate on its own [5], [14], [15] (when starting from Bi_2O_3 and GeO_2 powder mix), which would indicate that the crystals observed here were not formed through homogeneous nucleation. The mechanisms for crystal growth will be further investigated and discussed in the next Chapter III.

II.4. Conclusions

In conclusion, the molten core approach was used to fabricate crystalline core canes in the bismuth germanosilicate family. Two designs were investigated and shared structural similarities. The first design showed various crystal morphologies, which were shown to originate from compositional gradients across the cane core cross section due to the interaction dynamics of the BGO core melt with the soft glass cladding. Line-like and dendritic-like grain structures were found for crystals grown from bismuth-poor melts (25-33mol% Bi_2O_3), while more homogeneous grains were grown from melts close to the BGO stoichiometry (>33mol% Bi_2O_3). The second design employed showed a core microstructure closer to a single phase with a more homogeneous phase, which was attributed to the higher amount of Bi_2O_3 retained in the melt. In both cases, the cores were found to be polycrystalline and it was observed

that the grown crystals were of the form $Bi_4(Ge_{1-x}Si_x)_3O_{12}$ where silica would substitute for germania in the lattice. The crystal structure was shown to possess a larger amount of silica substitution when using the second design. Both designs also showed the possibility of fabricating crystalline core possessing heavy-preferred plane orientation (single crystal-like).

In this Chapter, the ability of the core to react with the glass cladding to form a crystal phase was demonstrated. The silica incorporation from the glass cladding was not shown to be an impediment due to the similar structures shared by germanium and silicon atoms, and one can use the silica incorporation to crystallize phases (solid solution) comprising silica. The Bi_2O_3 material transport was found to be the limiting factor towards the fabrication of a single crystalline phase in cane and control of the Bi_2O_3 content, and hence crystal morphology, through preform design was demonstrated. Future work will focus on the understanding of the eulytine crystal structure formation mechanisms during optical fiber draw employing the molten core method.

II.5. References

[1] V. Chani, K. Lebbou, B. Hautefeuille, O. Tillement, and J. M. Fourmigue, "Evaporation induced diameter control in fiber crystal growth by micro-pulling-down technique: $Bi_4Ge_3O_{12}$," *Crystal Research and Technology*, vol. 41, no. 10. pp. 972–978, 2006.

[2] S. F. Radaev, L. A. Muradyan, Y. F. Kargin, V. A. Sarin, V. N. Kanepit, and V. I. Simonov, "Neutron-diffraction investigation of single crystals of $Bi_4Ge_3O_{12}$ with the eulytine structure," *Sov. Phys. - Crystallogr. (English Translation)*, vol. 35, no. 2, pp. 204–206, 1990.

[3] Z. G. Zhang, Z. Y. Jiang, X. F. Wang, and Q. Q. Tian, "Correlation between grain deviation angles and the partial ordering transformation of grain line in $Bi_4Si_3O_{12}$ microcrystals," *Sci. Sinter.*, vol. 44, no. 3, pp. 257–264, 2012.

[4] J. B. Shim, J. H. Lee, A. Yoshikawa, M. Nikl, D. H. Yoon, and T. Fukuda,

"Growth of $Bi_4Ge_3O_{12}$ single crystal by the micro-pulling-down method from bismuth rich composition," *J. Cryst. Growth*, vol. 243, no. 1, pp. 157–163, 2002.

[5] G. Gévay, "Growth and characterization of $Bi_4Ge_3O_{12}$ single crystals," *Prog. Cryst. Growth Charact. Mater.*, vol. 15, no. 7, pp. 145–186, 1987.

[6] F. Smet and W. J. P. Van Enckevort, "In situ microscopic investigations of crystal growth processes in the system Bi_2O_3-GeO_2," *J. Cryst. Growth*, vol. 100, no. 3, pp. 417–432, 1990.

[7] L. Dimesso, G. Gnappi, A. Montenero, P. Fabeni and G. Pazzi, "The crystallization behaviour of bismuth germanate glasses" *J. Mater. Sci*, vol. 26, no. 15, pp. 4215–4219, 1991.

[8] A. Durif-Varambon, "Etude de la substitution du silicium dans quelques types d'orthosilicates (Study of the substitution of silicon in some types of orthosilicates)," *Bulletin de la société française de minéralogie et de cristallographie*, vol. 82, pp. 285–314, 1959.

[9] R. Nitsche, "Crystal Growth and Electro-Optic Effect of Bismuth Germanate, $Bi_4(GeO_4)_3$," *J. Appl. Phys.*, vol. 36, no. 8, pp. 2358–2360, 1965.

[10] H. Jiang, H. J. Kim, G. Rooh, H. Park, S. Kim, U. Fawad, and J. Cheon, "Czochralski growth and scintillation properties of bismuth germanium silicon oxide (BGSO) single crystals," *IEEE Nucl. Sci. Symp. Conf. Rec.*, pp. 1580–1582, 2011.

[11] H. Xie, F. Li, C. Chen, H. Xi, X. Wang, and X. Zhu, "Sol–gel preparation and characterization of $Bi_4(Si_{1-x}Ge_x)_3O_{12}$ solid solutions," *J. Sol-Gel Sci. Technol.*, vol. 72, pp. 37–42, 2014.

[12] J. Barbier, J. E. Greedan, T. Asaro, and G. J. McCarthy, "Neutron diffraction study of disorder in eulytite-type $Sr_3La(PO_4)_3$," *Eur. J. Solid State Inorg. Chem.*, vol. 27, no. 6, pp. 855–867, 1990.

[13] A. A. Kaminskii, S. N. Bagayev, N. V Kravtsov, S. N. Chekina, N. I. Ivannikova, K. Ueda, J. Lu, H. J. Eichler, G. M. A. Gad, J. Hanuza, J. Fernandez, and P. Reiche, "Spectroscopy and cw Laser Action, Magnetooptics and Nonlinear Optical Frequency Conversion in Ln^{3+} Doped and Undoped $Bi_4Ge_3O_{12}$ and $Bi_4Si_3O_{12}$ Crystals," *Laser Phys.*, vol. 11, no. 8, pp. 897–918, 2001.

[14] Schott glass, "Schott DURAN® tubing brochure." [Online]. Available: http://www.us.schott.com/tubing/english/products/DURAN.html.

[15] Y. Fei, S. Fan, R. Sun, and M. Ishii, "Study on phase diagram of Bi_2O_3-SiO_2 system for Bridgman growth of $Bi_4Si_3O_{12}$ single crystal," *Prog. Cryst. Growth Charact. Mater.*, vol. 40, no. 1, pp. 183–188, 2000.

[16] W. J. P. Van Enckevort and F. Smet, "In situ microscopy of the growth of bismuth germante crystals from high temperature melts," *J. Cryst. Growth*, vol. 82, no. 4, pp. 678–688, 1987.

CHAPTER III

INVESTIGATION OF THE FABRICATION OF BISMUTH SILICON OXIDE $Bi_4Si_3O_{12}$ (BSO) CRYSTALLINE FIBERS VIA THE MOLTEN CORE METHOD

It was previously demonstrated in Chapter II that incorporation of glass cladding compounds involved in the molten core method was significant and impeded the conservation of a BGO stoichiometry in the core. This prevented nucleation and growth of a pure BGO single crystalline phase. An alternative to the formation of BGO crystals was shown with the formation of BGSO crystals. Since BGO and BSO crystals have similar structures, let alone physical, thermal and optical properties (including high refractive index and high electro optic coefficient [1]), it was thus in this context that $Bi_4Si_3O_{12}$ single crystalline formation, utilizing the inherent silica cladding, was attempted in order to understand the mechanisms of the eulytine crystal formation during fiber draw.

This chapter focuses on the growth of BSO crystalline core fibers. The first section will explain how this is performed. The second section will state the materials and methods used. Then, the third, fourth and fifth sections, respectively, will gather the results of each experimental design on the formation of BSO crystals through homogeneous nucleation, heterogeneous nucleation and phase transformation reactions, respectively. Finally, the sixth section will provide an overall comprehension of the fiber draw dynamics investigated in this chapter.

III.1. Nucleation and growth theory

The kinetic theory of glass formation dictates that there are two main barriers imposed on a system that will control the formation of a crystalline phase from a melt: a thermodynamic and a kinetic barrier. The thermodynamic barrier relates to the net free energy change the system experiences after a nucleus has formed (W). This dictate if the system experiences enough of a driving force for the nucleation process to take place (i.e., formation of a stable nuclei). On the other hand, the kinetic barrier relates to the activation energy required for an atom/molecule to cross the melt/solid interface (ΔE_D) and thus it will control cluster formation as well. Both barriers are described in the nucleation rate I as follow:

$$I = n\nu e^{(-N_A W^*/RT)} e^{(-\Delta E_D/RT)} \tag{2.1}$$

where n is the number of atoms per unit volume, υ is the atomic vibration frequency, N_A is the Avogadro's number, R is the gas constant and T the absolute temperature. The first exponential in Equation 2.1 relates to the thermodynamic barrier and the second exponential relates to the kinetic barrier. If no barriers existed in the nucleation process, then all vibrating atoms would join the nucleus and the nucleation rate would sum to $n\upsilon$.

We can see that these barriers are a function of temperature, which could become a critical factor to control in the crystal formation process. Perhaps the most interesting point of the kinetic theory of glass formation is the role of the thermodynamic barrier, which can be controlled to some extent. The thermodynamic energy barrier W is described as follow:

$$W = \frac{4}{3}\pi r^3 \Delta G_x + 4\pi r^2 \sigma \tag{2.2}$$

where r is the nuclei radius, ΔG_x is the free energy of crystallization (i.e., the change of free energy to transform one unit of liquid into one unit of crystal) and σ is the surface energy of the melt/solid interface. It is seen that the volume energy term (first term in Equation 2.2) is a negative term ($\Delta G_x<0$ below the melting point) while the surface energy (second term in Equation 2.2) is positive ($\sigma>0$). Hence, both terms compete against each other as nuclei are formed, and the surface energy term dominates at small nuclei radius sizes while the volume energy term dominates at large nuclei radius size. Below a critical radius size, the nuclei will experience a high constraint for growth due to the high surface energy needed to be overcome. If it survives above the critical size (about 50% chance survival according to Varshneya [2]), the nuclei will freely grow. This case is known as homogeneous nucleation. Of particular interest is the fact that one can lower the thermodynamic energy barrier through the surface energy term. When a foreign substrate surface is present in the liquid melt, the supercooled liquid attempts to nucleate onto the substrate. The supercooled liquid wets the substrate surface and a contact angle between the substrate, the supercooled liquid and the crystal is formed. When the contact angle is 0°, the surface energy term is nullified and there is no more constraint for the formation of a nuclei (viz., fully wetting conditions). As the wetting angle value is found to be higher, the surface energy of the system will be increased and the thermodynamic barrier will increase accordingly. Hence, the overall surface energy of a system can be lowered through addition of foreign surfaces. In general, the foreign surface added to the system is a crystal of the same nature as the liquid melt so that there are no lattice strain constraints for growth, such as seen in single crystal growth techniques (Czochralski, micro-pulling down or hydrothermal…). This case is known

as heterogeneous nucleation. It is worth mentioning here that homogeneous nucleation is a stochastic process whereby multiple spontaneously nucleated nuclei adopt random crystal plane orientations throughout the matrix (unless special post-processing conditions are used such as laser recrystallization [3]–[5]), while heterogeneous nucleation is a non-stochastic process and the melt in contact with the seed takes the same crystal plane orientation as the seed (cf. single crystal growth techniques).

Once a nucleus is formed, crystal growth is the next mechanism to take place. Atoms are deposited layer by layer at the crystal surface and the growth front advances steps by steps. Varshneya [2] shows that the growth rate is controlled by the kinetics of mass transport, i.e., how rapidly atoms can diffuse from the liquid to the crystal growth front. The net crystal growth rate u is shown as:

$$u = a(\upsilon_{lx} - \upsilon_{xl}) \tag{3}$$

where a is the distance between liquid and crystal region (on the order of molecular diameter), υ_{lx} is the atomic jump frequency from liquid to crystal and, υ_{xl} is the atomic jump frequency from crystal to liquid. A further derivation of Equation 2.3 using the Wilson-Frenkel theory and Stokes-Einstein relation gives the crystal growth rate as [2]:

$$u = \left(\frac{fRT}{3N\pi a^2 \eta}\right)\left(1 - e^{\frac{\Delta H_f \Delta T}{RTT_m}}\right) \tag{2.4}$$

where f is the fraction of the surface area on which growth sites may be available, η is the viscosity, ΔH_f is the heat of fusion and ΔT is the degree of supercooling ($\Delta T = T - T_m$). From Equation 2.4, it is seen that crystal growth can be controlled by the

viscosity of the melt at the crystal interface, where viscous melt will tend to diminish the crystal growth rate. Additionally, the degree of supercooling is another parameter towards the control of crystal growth, where temperature close (or far) from the melting point will simply preclude crystal growth. Figure III-1 shows a classical view of the competition between nucleation rate (Equation 2.1) and crystal growth rate (Equation 2.4) as a function of temperature in a typical system. It is seen that the (spontaneous) nucleation process takes place at lower temperature than crystal growth and that the overlap of both curves allows the crystallization process to take place. Some system may not exhibit a strong overlap between both curves and then will easily tend to form a glass. It is also worth noting that time is another parameter controlling the crystallization process, whereby long time at certain temperature will allow the crystallization process to occur (Time-Temperature-Transformation or TTT curves).

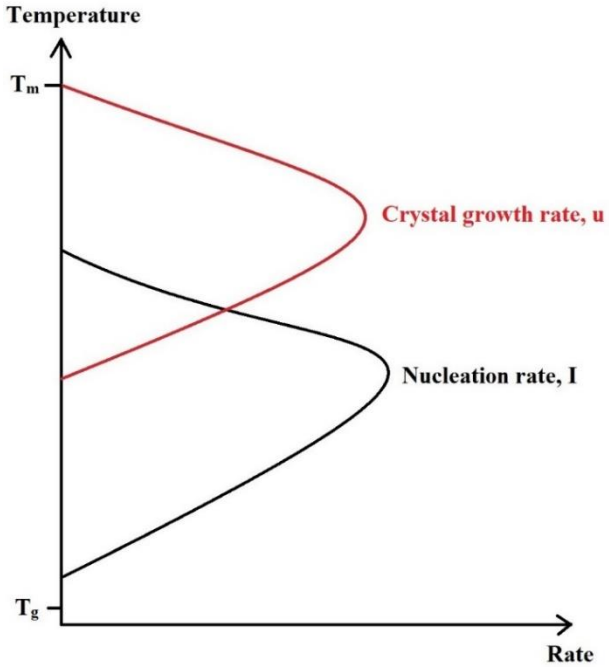

Figure III-1. Rate dependence of crystal growth and nucleation with temperature.

III.2. Experimental designs

From the previously described kinetic of glass formation and the literature review on BSO (and BGO) crystal formation, one can envision three ways to crystallize BSO crystals in an optical fiber. The first is to produce a BSO stoichiometric core melt from which nuclei will spontaneously form and grow as large crystals (homogeneous nucleation). The second is the formation of BSO crystals onto a pre-existing crystal seed (preferentially of the same nature as the aimed crystal such as BGO), which will allow a decrease in the thermodynamic barrier to nucleation and favor the crystallization process (heterogeneous nucleation). Finally, the third possibility is to use a phase transformation path from a specific reaction whereby BSO (and BGO) crystals could be grown. The reaction is the following: $2Bi_2SiO_{5\ (s)} + SiO_{2\ (glass)} \rightarrow Bi_4Si_3O_{12\ (s)}$ (similarly with BGO) [6]–[8].

The first experimental design thus explored the crystallization of BSO crystals through homogeneous nucleation. Although difficulties in observing spontaneous nucleation of BSO crystals have been mentioned [7], this was reported using the Bridgman method and will be investigated using the molten core method. This experimental design employed the powder-in-tube method where Bi_2O_3 precursor powder was inserted in the hollow core of a borosilicate glass cladding tube from atop. The interaction between the glass cladding and Bi_2O_3 melt would bring a core composition close to the BSO stoichiometry, which could subsequently crystallize.

The second experimental design investigated the crystallization of BSO (or BGSO) crystals through heterogeneous nucleation. For this purpose, BGO crystal powder was mixed with Bi_2O_3 powder so that the former offered nucleation sites. The drawing

temperature was above the melting point of Bi_2O_3 and below that of the BGO crystal powder to preserve the integrity of the seeds. Additionally, a similar design to that of single crystal growing techniques (i.e., micro-pulling down method) was investigated, whereby a BGO seed pellet was loaded at the bottom of the hollow core of a borosilicate glass cladding tube and Bi_2O_3 powder was inserted on top of it.

Finally, the third experimental design explored the phase transformation reaction. This design aimed at the formation of Bi_2SiO_5 metastable crystals in cane using a powder "confinement effect" (more details in Chapter IV). The cane containing the metastable crystals was then redrawn to fiber to investigate the possible reaction.

III.3. Materials and Methods

III.3.1. Sample preparation

In the following experiments, two silica-based commercial cladding glass tubes were used: borosilicate glass cladding tubes (denoted DURAN®) of dimensions 3x30 mm and 3x18mm (inner diameter x outer diameter) and composition $81SiO_2$-$13B_2O_3$-$4Na_2O$-$2Al_2O_3$ in wt%; and a soda-lime-silicate cladding glass tube (denoted AR-GLAS®) of dimensions 3x18 mm and composition $69SiO_2$-$13Na_2O$-5CaO-$4Al_2O_3$-$3K_2O$-3MgO-2BaO-$1B_2O_3$ in wt%. The DURAN® cladding glass draw range is 950-1100°C while the AR-GLAS® draw range is 850-885°C. The former requires special processing where two drawing steps are needed: the preform is drawn to a large diameter "fiber" size on the order of millimeters (called "cane") that is then redrawn to fiber size (125 µm). This two-step processing prevents crystallization of the fibers at the surface that would take place if the preform was drawn directly to fiber; thus, this increases the mechanical properties of the drawn fibers. AR-GLAS® does not necessarily require this additional processing unless desired for specific reasons. High

purity commercial powders were utilized for draws requiring powder precursors (Bi_2O_3, 99.9995%; B_2O_3, 99.995%; CeO_2, 99.5%). The powder was introduced in the hollow core of the cladding glass tube whether as-is (inserted from atop) or as three millimeter hand-pressed pellets.

In the first experimental design, the precursor material employed high purity Bi_2O_3 powder inserted in a 3x30mm DURAN® preform. The latter was drawn at 1060°C and a speed of 0.3 $m.min^{-1}$.

In the second experimental design, the precursor material was a mixed powder of BGO and Bi_2O_3. The BGO powder was obtained from a BGO single crystal that was crushed in a silica mortar with a pestle. The proportion used was 50wt%BGO-50wt%Bi_2O_3. This powder mix was packed in a 3x30mm DURAN® preform. This latter was held in the drawing tower at 860°C for five minutes and then brought at a temperature of 1000°C for drawing (about 50°C below the melting temperature of the BGO single crystal). The drawing speed employed was of 0.45 $m.min^{-1}$. In the experimental design resembling closely to that of the micro-pulling down method, a BGO single crystal of 3 mm diameter and 3.8 mm height was inserted in a 3x30 mm borosilicate preform and high purity Bi_2O_3 powder was inserted atop the BGO single crystal (Figure III-2). The preform was then drawn at 1080°C to a four millimeter cane at a speed of 0.32 $m.min^{-1}$.

In the third experimental design, three millimeter hand-pressed pellets of composition $99.5Bi_2O_3$-$0.5CeO_2$ were stacked in a 3x30mm DURAN® preform. The preform was drawn at 960°C to four millimeter cane diameter at a speed of 0.3 $m.min^{-1}$. The obtained cane was redrawn to fiber at 950°C and a speed of 20 $m.min^{-1}$. A

3x18mm AR-GLAS® preform was also used to investigate the reaction path and employed three millimeter hand-pressed pellets of composition $89.8Bi_2O_3$-$10B_2O_3$-$0.2CeO_2$ stacked in its hollow core. The preform was drawn at 885°C to 2.5 mm cane at a speed of 5 $m.min^{-1}$. The cane was then redrawn to fiber at 885°C with a speed of 3 $m.min^{-1}$.

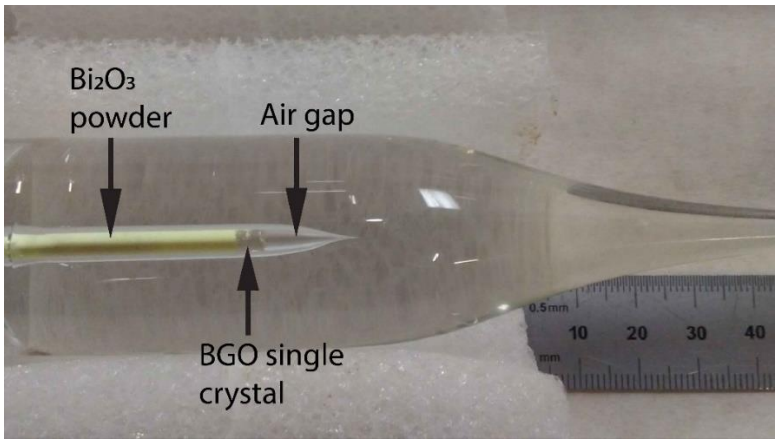

Figure III-2. Picture of the employed second design preform, closely resembling to that of micro-pulling down method. The air gap was a result of the preform preparation.

III.3.2. Electron microscopy

A Hitachi SU-6600 Scanning Electron Microscope (SEM) with Energy-Dispersive X-ray spectroscopy (EDX) in secondary electron (SE) mode was utilized to observe the morphology and analyze the composition of the core. The SEM was operated with electron beam energy of 20 kV in a variable pressure environment of 30 Pa. The working distance was about 10 mm. The canes were manually polished to a 2.5 µm finish or mechanically polished to a 0.05 µm finish. In all experiments, EDX is not able to detect the boron element and therefore, all compositions obtained are not true compositions but rather provide insights into changes from the original core phase to the final fiber. Herein, all compositions are mentioned in mol%. The starting crystals' structure, orientation and spatial arrangement were also investigated using the Hitachi

SU-6600 SEM with an attached Oxford Instruments Electron Backscattered Diffraction (EBSD) camera. The samples were polished to a 0.05 µm mirror-like finish in a silica colloidal solution before analysis, and were mounted on a 45° pre-tilted holder. The samples were analyzed at a 70° angle in the chamber (with respect to the horizontal), a working distance of 18 mm and a 20 kV accelerating voltage. EBSD patterns were taken with a resolution of 334 x 256 pixels. It is important to underline that EBSD is not an accurate technique to detect (new) crystalline phases since it detects the phases that the experimenter input before the measurement is performed, which are then matched with the detected Kikuchi bands.

III.3.3. Powder X-ray diffraction

Powder x-ray diffraction was performed in order to verify the crystallinity of the obtained canes and fibers. A Rigaku Ultima IV diffractometer was used for this purpose, using the Cu Kα radiation (λ=1.5408Å) for X-ray generation. Canes and fibers were crushed into powder in a silica mortar. The obtained powder contains both cladding and core material. The scan speed was set to 0.6-0.7 deg.min^{-1} and the 2-theta scan range was set between 5° and 70°. The obtained XRD diffractogram were analyzed using the OriginPro 8 software, and this latter was utilized to subtract baselines.

III.4. Formation of BSO crystalline optical fibers through homogeneous nucleation

Figure III-3 depicts the beginning of a cane drawn at 1060°C from Bi_2O_3 powder drawn in a 3x30 mm borosilicate preform (using “poured powder design”, see Chapter IV section IV.2) and a speed of 0.3 mm.min^{-1}. A homogeneous yellow core was observed at the beginning of the draw then followed by a brown core. The cane

core results are summarized in Table III-1. The core at position A was well circular as depicted by the SEM image cross-section (Figure III-4a) with a concentration gradient along its cross-section as illustrated by the EDX compound concentration profile (Figure III-4b). As seen from Table III-1, the core composition had a large amount of Bi_2O_3 (~50 mol%) that was close to the Bi_2SiO_5 stoichiometric composition. The metastable Bi_2SiO_5 crystals were shown to crystallize over a wide range of concentration [7], [9], as seen from Figure III-5. Yet, the core did not show any crystalline structures here and was demonstrated as glassy.

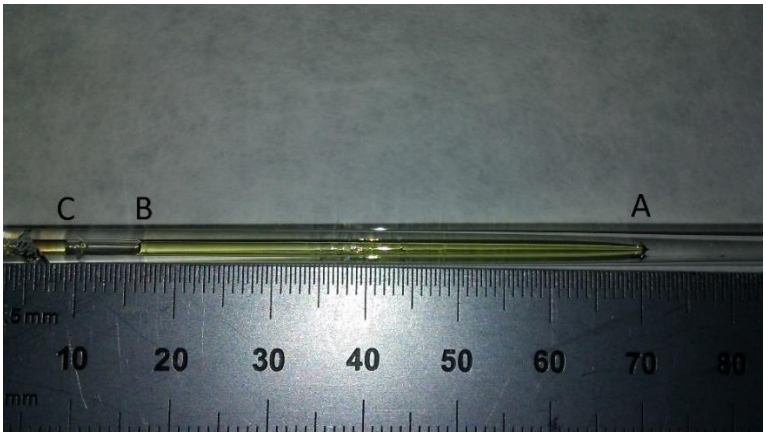

Figure III-3. Picture of the beginning of a cane drawn from a Bi_2O_3 core powder poured in borosilicate glass cladding. Position A corresponds to the beginning of the draw.

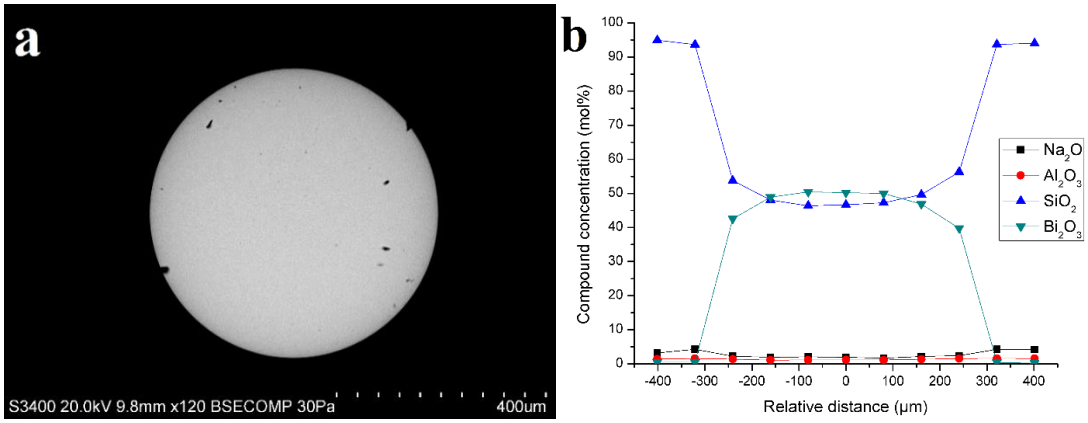

Figure III-4. (a) SEM micrograph of the yellow core cane cross-section at position A in Figure III-3. (b) EDX compound concentration profile across the same core.

Similarly, the core at position B (Figure III-6a) showed a concentration close to BSO and yet, the core was shown to be amorphous. This indicates that the core compositions have been kinetically trapped and crystal growth could not take place. Perhaps small nuclei were formed but could not grow due to the high surface energy barrier imposed in this system. Thus, homogeneous nucleation of BSO crystals is refuted as a mechanism for fiber crystal growth using the molten core method. It is worth noting that the large quenching rate employed here was not the reason for preventing crystal growth as previous canes drawn in Chapter II demonstrated crystallinity despite similar quenching rates.

Interestingly, the compositions observed here are similar to that described in the first design experiment in Chapter II employing a BGO single crystal, and yet a crystal phase was obtained in the latter case. This indicated that a different mechanism took place in the design employing the BGO single crystal and will be discussed later in this Chapter. Moreover, it is worth mentioning that the distinct core-cladding interface did not offer nucleation sites in the present case. Crystal nucleation at liquid-liquid interfaces has been reported for various material systems in the literature (see for example [10]). The core is in a liquid state and the cladding is in a low viscosity glassy state, and both core and cladding have distinct compositions. Hence, one could think that the cladding could offer a foreign surface for growth upon drawing. However, this process was not observed and the energetic requirements were likely not met (low interfacial energies, specific chemical interactions…).

Table III-1. Cane properties from that observed in Figure III-3. The compositions are given at the core center. Ø=diameter. All compound concentrations are expressed in mol%.

Position	Core color	ØCane (mm)	ØCore (µm)	Core-cladding ratio	SiO_2	Bi_2O_3	Al_2O_3	Na_2O
A	Yellow	3.5	560	0.16	46.7	50.1	1.2	2.0
B	Yellow	3.5	1260	0.36	54.4	40.7	1.5	3.4
C	Brownish*	3.5	1000	0.29	56.2	38.6	2.0	3.2
D**	Brownish*	3.5	105-150	0.04	69.5	25.7	1.1	3.7

*: The difference in color will be explained in Chapter IV.
**: This core was taken further down the cane length and is thus not shown in Figure III-3.

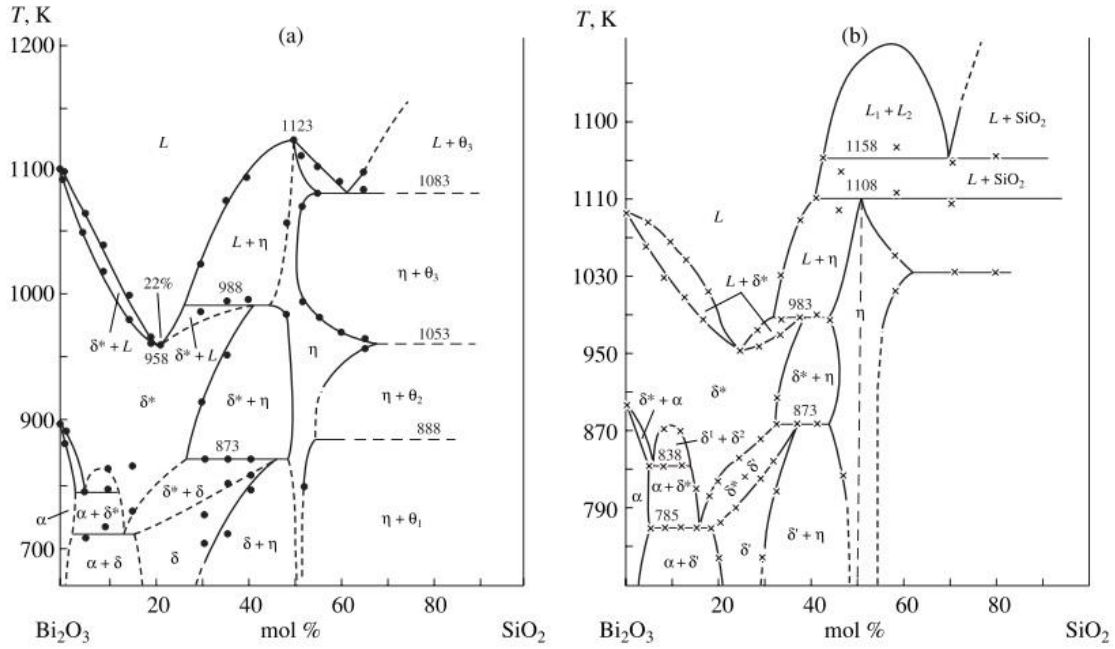

Figure III-5. Phase diagram of the metastable phases in the Bi_2O_3-SiO_2 system, taken from [9]. Legend: L = liquid, δ = δ-Bi_2O_3-based solid solution, η = Bi_2SiO_5.

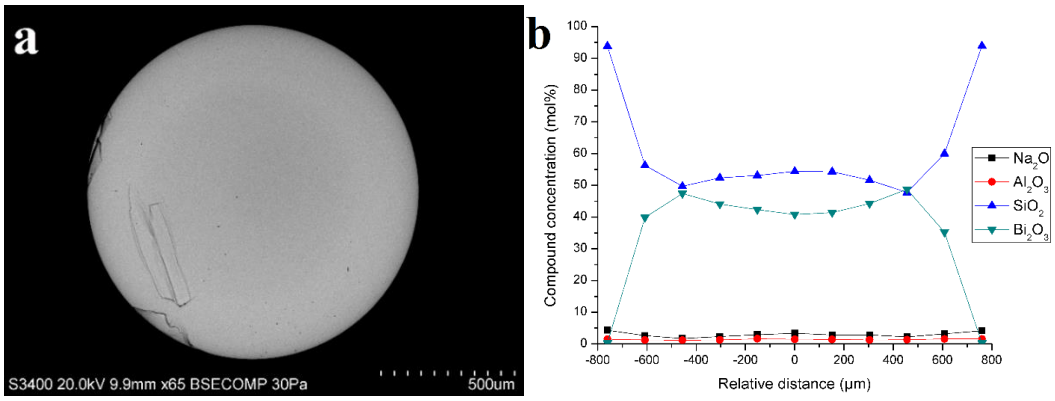

Figure III-6. (a) SEM micrograph of the yellow core cane cross-section at position B in Figure III-3. (b) EDX compound concentration profile across the same core.

Furthermore, it is interesting to note the unusually large core size (1.26 mm) following the very beginning of the draw, which is a third of the diameter of the cane. The core-clad ratio of the preform should be kept during draw (in this case 0.1) and a core size of 350 μm would have been expected for a 3.5 mm cane diameter. The α-Bi_2O_3 crystal precursor is known to experience a volume expansion of ~7% upon its solid-solid transformation at 730°C in addition to the volume expansion upon melting (unknown value). Additionally, the α-Bi_2O_3 powder possesses a high coefficient of thermal expansion (CTE), on the order of ~100x10^{-7} K^{-1} [11]–[13], while the CTE of the glass cladding is ~33 x10^{-7} K^{-1} [14]. Hence, as the precursor powder is heated up, it expands with a larger magnitude than the glass cladding. The powder melt is confined in a viscous glass and will thus generate lateral forces against the cladding as it expands. This causes the glass cladding to flow around a large core volume as the cane is drawn, and thus generates a large core. Note that the small core size at position A originates from the preform initial preparation. The bottom of the core preform was slightly tapered during preform preparation and thus the preform had a smaller core diameter at its bottom. Hence, the molten core was drawn from a smaller initial core diameter resulting in a smaller core size after draw.

It was observed here that the Bi_2O_3-SiO_2 system studied with the molten core method behaves the same way as in all single crystal growth techniques, i.e., nuclei in this system cannot form spontaneously from the melt upon cooling. The growth mechanism likely requires a seed to start the growth from a melt (heterogeneous nucleation) and this will be the topic of the next section. Despite the amorphous nature of the obtained canes, these latter are still of interest for their nonlinear optical properties.

III.5. Formation of BSO crystalline phase through heterogeneous nucleation

We have seen previously that despite the use of the silica cladding incorporation to obtain a homogeneous phase close to BSO stoichiometry, the thermodynamic energy barrier was likely too large for the close stoichiometric melt composition to nucleate seeds that could subsequently grow. In order to reduce this thermodynamic energy barrier, heterogeneous nucleation was forsaken. Similarly to the standard single crystal growth techniques (such as Czochralski, µ-PD [15]–[18]), the presence of a BGO seed for the precursor powder melt to grow onto will lower the thermodynamic energy barrier and promote nucleation and growth. In our case, the aim was to offer nucleation points to the surrounding Bi_2O_3-SiO_2 melt to attach to and grow from. For this matter, two different designs were employed. The first design made use of a precursor powder composed of BGO crystal seeds mixed with Bi_2O_3 powder. As the precursor powder melts and reacts with the silicon dioxide introduced by the glass cladding, the molecules from the melt attaches onto the crystal seeds during fiber draw, thus triggering the growth process upon cooling. The draw temperature employed was below the melting temperature of the seeds to avoid their melting. The second design employed a similar design as the µ-PD method, whereby a BGO single

crystal seed was introduced at the bottom of the core preform and Bi_2O_3 powder was placed on top of it (using the "poured powder" design).

III.5.1. First design: Bi_2O_3-BGO powder mix

White core canes were obtained at different positions during the draw and analysis on two of them was performed. Their lengths were on the order of ~3-4 cm. Figure III-7 shows a SEM micrograph of a white core cane cross-section. The cane was 2.5 mm diameter and the core was 285 µm diameter. The core microstructure was seen to contain small grains as well as dendrite-like and line-like grains similar to that obtained in Chapter II section II.3.2. The composition of the grains varied from $56.6SiO_2$-$15.5GeO_2$-$25.4Bi_2O_3$-$0.7Al_2O_3$-$1.8Na_2O$ to $47.9SiO_2$-$20.2GeO_2$-$30.0Bi_2O_3$-$0.6Al_2O_3$-$1.3Na_2O$ as one goes towards the center of the core. The crystal composition was not close to the BGSO stoichiometric composition due to the inherent core-cladding interaction. Again, the composition values are skewed due to the EDX technique not detecting the boron element, as discussed in Chapter II section II.3.2.1.

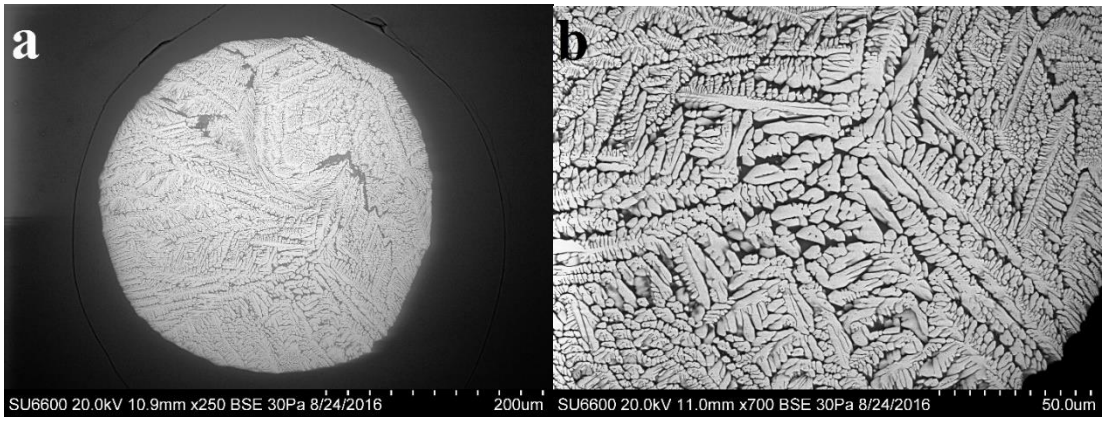

Figure III-7. (a) SEM micrographs of a white core cane cross-section derived from a BGO-Bi_2O_3 powder mix precursor. (b) SEM micrograph of the same core with enhanced magnification. The core is polycrystalline with small grains as well as dendrite- and line-like grains.

Comparison with the draw performed for homogeneous nucleation in previous section III.4 demonstrates that the addition of BGO seeds to the Bi_2O_3 powder triggered the growth of BGSO crystals. The core cross-section surface was quasi-full of BGSO crystals with a quasi-circular shape. One could think that the powder mix was not well homogenized and that the observed grains were a result of non-melted BGO seeds. SEM analysis of the powder mix showed that even though the BGO particles were aggregating over small areas in the powder mix (on the order of tens of microns square, see Figure B-1 in Appendix B), this would not account for the large amount of crystals observed here. Additionally, a draw of BGO crystal in powder form was performed in the same conditions as here. Two observations refuted the hypothesis that the observed crystals here were a result of non-melted BGO seeds: a non-circular core shape and the difference in observed microstructures (see Figure B-2 in Appendix B). Hence, the observed crystals here were confirmed as being the result of crystal growth, asserting the mechanism of heterogeneous nucleation. The BGO crystal seeds were effectively used to lower the thermodynamic energy barrier for crystal growth by offering a pre-existing nucleation surface for the surrounding Bi_2O_3-SiO_2 melt to grow onto. Furthermore, one notes that the matrix (or grain boundaries) was silica-rich, indicating that the crystals were grown from a bismuth-poor melt. This is likely due to two factors: first, a large amount of seeds was introduced in the powder mix (roughly in a 50-50 volume%) thus lowering in the first place the possible amount of bismuth available for attachment at the growth front; and secondly, the inherent core-cladding interaction that takes place in the molten core method further decreases the amount of bismuth in the core melt. A subsequent draw employing a 10BGO-90Bi_2O_3 (wt%) precursor powder mix was performed in order to

increase the amount of bismuth available in the core. The canes were drawn at 1000°C and a speed of 0.3 $mm.min^{-1}$. Interestingly, the core canes were shown to be glassy. This draw employed the "poured powder" design mentioned in Chapter IV section IV.2 and this design likely influenced the obtained end phase of the core (i.e., it allowed the dissolution of the BGO seeds). Hence, there would be a necessity of controlling the BGO particle sizes to avoid their dissolution when using the "poured powder" design. In contrast, the "powder packed" design shown above proved its ability in retaining the integrity of the precursor seeds as a crystalline core was demonstrated. This experiment revealed the importance of the materials' processing during the preform preparation. A similar experiment with a powder packed precursor design should help in retaining the integrity of the seeds.

The crystal structure of the core crystals was analyzed using PXRD and EBSD techniques. Figure III-8 shows the PXRD diffractogram, and the crystalline peaks were matched with the eulytine structure. Large peaks shifts were noted (~0.4°-1.0°) compared to those of the BGO single crystal source. As explained in previous Chapter II, solid solutions $Bi_4(Ge_{1-x}Si_x)_3O_{12}$ can be fabricated [19]–[21] due to the similar atomic structure of the germanium and silicon atoms, which can easily substitute for each other in the eulytine structure; and, peak shifts to higher 2-theta angle indicate the substitution of germanium by silicon atoms. The peak shifts observed here on the first peaks were larger than that shown in the previous Chapter II and thus indicated that the crystal growth in the present experiment likely took place from a large silica content melt.

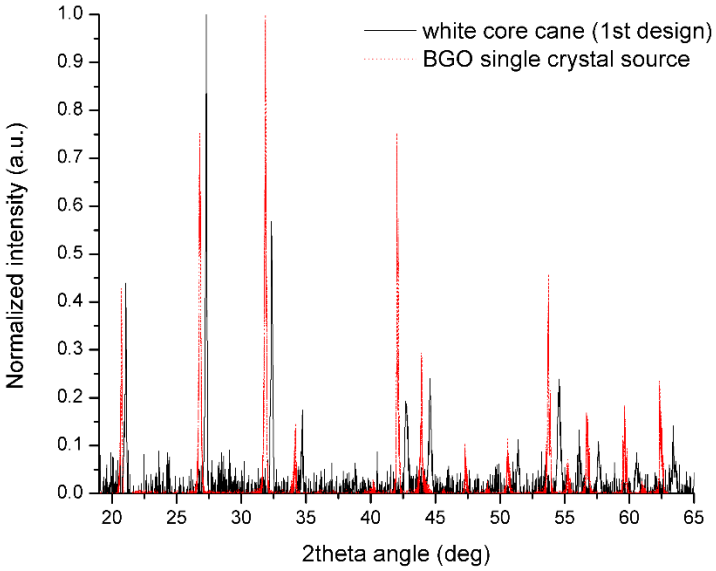

Figure III-8. PXRD diffractogram of the white core cane derived from the BGO-Bi_2O_3 powder mix design (1st design). Crystalline peaks were observed and matched with the BGO eulytine structure.

EBSD analysis provided additional insight about crystal plane orientation. Figure III-9 depicts the inverse pole figures (IPF) orientation maps in the X, Y and Z axis. Random crystal plane orientations were noticed in the core, as seen in Table III-2. It is worth noting that large areas of the core showed nonetheless similar orientation. These large areas were shown to be polycrystalline and hence crystals in these same areas were grown along the same direction. This single crystallinity-like trend found here was similar to that observed in Chapter II.

Table III-2. Plane orientations of the grown BGSO crystals observed in the EBSD pictures in Figure III-9. Grain 1 corresponds to the pink grain in Figure III-9b and next grains are labeled clockwise from the pink grain.

Grain	Plane grown in X axis	Plane grown in Y axis	Plane grown in Z axis
1	16-1	-412	205
2	3-1-1	26-1	104
3	66-5	-231	416
4	-5-46	4-6-1	536
5	-5-45	3-5-1	314

Interestingly, the design employed here revealed that single crystallinity was not obtained throughout the whole core, as compared to all previously discussed results in Chapter II (see Table III-3 for a summary). This difference could be originating from the initial precursor design (BGO powder vs BGO single crystal), where the larger surface area offered by the BGO powder particles could statistically lead to random plane growth, in a similar manner to what would be seen in a homogeneous nucleation process. However, each crystal grain grown from a different seed would have led to a different orientation and thus each grain would have been observed with a different color on the IPF maps. Since this was not observed, this hypothesis was refuted. Furthermore, another draw employing the same BGO powder precursor design demonstrated a single crystalline-like core (see Figure B-3 in Appendix B). Thus, the precursor design (BGO powder or BGO single crystal) was not a sufficient parameter to say to influence the single crystallinity outcome of the core canes. When comparing the two draws involving the same BGO powder design (see first two rows in Table III-3), it is seen that the difference in single crystallinity could only arise

from the draw speed and the cane sizes drawn (which are interconnected parameters). A different cane size and draw speed would mean that different cooling rates were experienced by the two cores, where the core drawn from the smaller cane size would be quenched more rapidly due to the larger surface-to-volume ratio. Hence, a larger thermal gradient was experienced in the smaller size cane and may be at the origin of the single-crystallinity difference. Although the quenching rate is known to affect the crystal sizes in materials, it is unknown if the quenching rate influences the crystal plane orientation. From the analysis and annealing experiment of silicon optical fibers drawn with the molten core method [3], it seems that the ability of the core to demonstrate single-crystallinity is an arbitrary process. Silicon fibers demonstrated polycrystalline regions with and without the same plane orientation, and this behavior was shown despite identical quenching rates. Perhaps the inherent directionality of the optical fiber drawing process promotes crystal growth in a coherent manner, i.e., in the same plane direction.

It is worth noting here that both canes compared here were drawn at 1000°C and even though the core was in a molten state, the crystal growth can take place upon heating the preform. Indeed, the Bi_2O_3 powder melted at 820°C and interacted with the glass cladding. Thus, the conditions for the bismuth silicate melt to grow onto the pre-existing BGO seeds were likely gathered before cooling. Knowing that the crystal growth rate range is found at a slightly lower temperature than the melting point, the temperature at which the Bi_2O_3 powder melted (820°C) was likely in the range for crystal growth. Hence, in this case, the cooling rate was likely an irrelevant parameter that could influence single-crystallinity. One could imagine that the thermal gradient upon heating could play a role, whereby the core-cladding interface would be the first

area to encounter the crystal growth conditions. This could be supported by the fact that the different crystal plane orientation seems to converge towards the core center; however, this hypothesis is refuted by the similar draw that showed a single crystal-like core. Hence, the origin of differences in single crystalline behavior is unexplained.

Table III-3. Comparison of draw parameters for different precursor designs employed for the fabrication of BGSO crystals and the single crystal-like outcome behavior of the obtained core cane.

Precursor design	Preform size (mm)	T_{draw} (°C)	Draw speed (m/min)	Cane size (mm)	Core size (µm)	Single crystalline-like core?
50BGO-50Bi_2O_3 wt% powder	3x30	1000	0.45	2.5	285	No
50BGO-50Bi_2O_3 wt% powder	3x12	1000	0.7	0.7	165	Yes
1.2 mm BGO single crystal	3x30	1080	0.3	3.8	865	Yes
1.2 mm BO single crystal + Bi_2O_3 powder around	3x30	1080	0.3	3.8	1020	Yes
3 mm BGO pellet + Bi_2O_3 on top	3x30	1080	0.3	4.4	1450	Yes

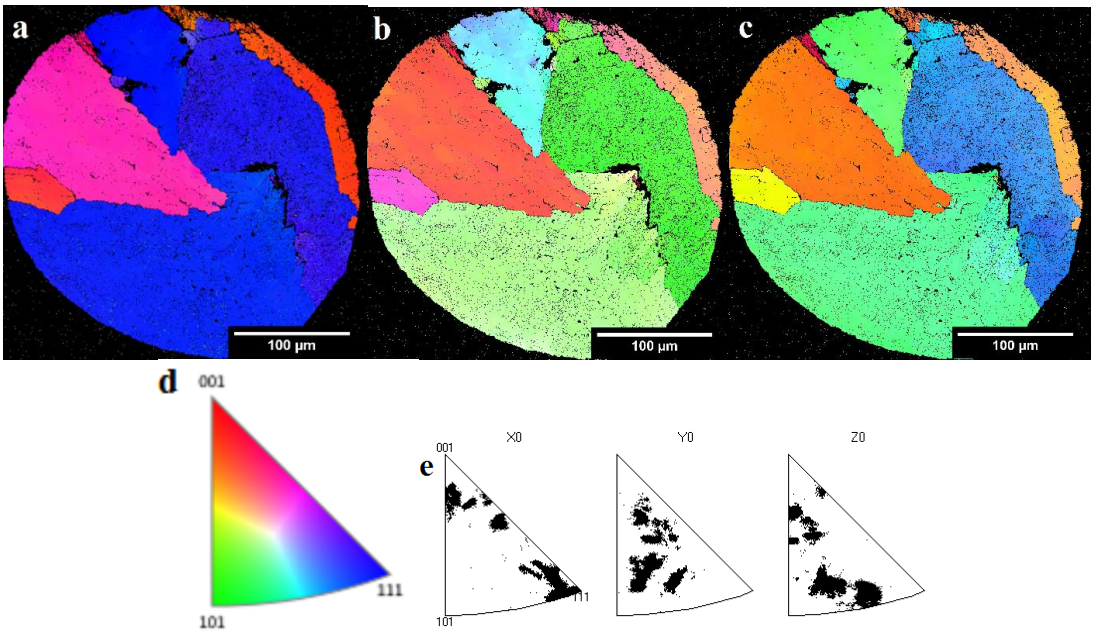

Figure III-9. IPF orientation maps along the a) X-, b) Y- and, c) Z-axis of the white core cane drawn using the first design. d) Stereographic triangle showing the orientation color-scale. e) Color matching between each pixel in each orientation map and the orientation color-scale, showing random plane orientation along each axis.

A tapering experiment was performed to investigate the recrystallization behavior of the newly formed BGSO crystals into a single-phase core. Laser recrystallization is a post-processing technique that has shown to be powerful to produce single phase fibers (see for example [4]). Its operation is similar to zone melting (or refining), whereby a CO_2 laser is used (rather than a heater or induction coils) to scan along the fiber's core to melt the core and recrystallize it. Figure III-10a shows an optical micrograph of the BGSO cane tapering process. The bright orange color corresponds to the core being melted and reshaped. Figure III-10b depicts an optical micrograph of the obtained taper, showing a clear and homogeneous core. The taper was analyzed with SEM and EDX (Figure III-11). The core diameter was 76-105 µm and the cladding taper diameter was 950 µm. The taper was seen with an asymmetrical shape due to the high power employed that was necessary to melt the large cane volume (the

cladding evaporated from the heat provided). EDX analysis revealed a core concentration of $62.7SiO_2$-$21Bi_2O_3$-$11.2GeO_2$-$3.2Na_2O$-$1.9Al_2O_3$ at core center (Figure III-11c).

It is interesting to note that no microstructures were observed with SEM in the core taper. The core was shown to be glassy with EBSD (not shown) and this indicated that the core melted during the tapering process. During the melting, the core melt was likely interacting with the glass cladding as evidenced by the lower amount of Bi_2O_3 (and larger amount of SiO_2) observed by EDX. Hence, the core composition was driven further away from that of the BGSO crystals. The crystal units were fully melted during the tapering process and crystal seeds were not available for further growth through heterogeneous nucleation, nor did recrystallization at the heated front take place. As a preliminary step, and despite the difficulties to control the conditions during the tapering process, the laser recrystallization was not shown to be a valuable process towards the recrystallization of the BGSO core cane.

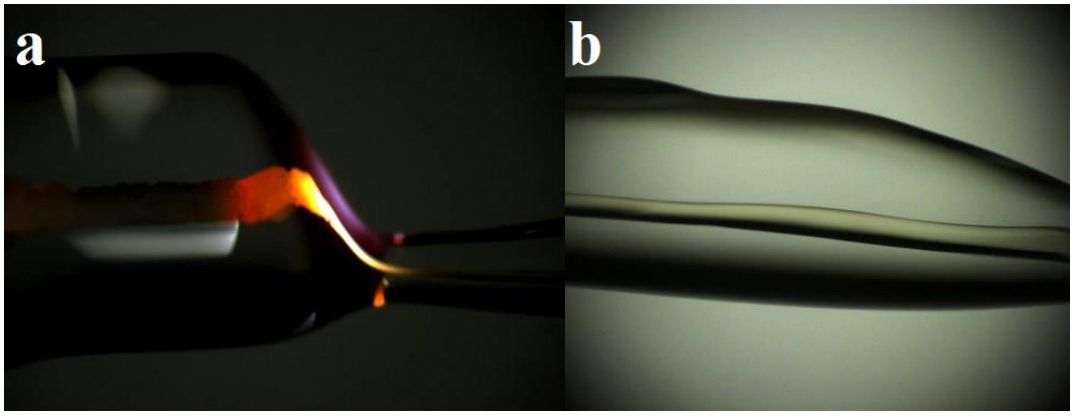

Figure III-10. a) Optical micrograph of the cane drawn with the first design (containing BGSO crystals) and its tapering process. The orange/yellow color shows a molten core. b) Optical micrograph of the obtained taper showing a clear and homogeneous core.

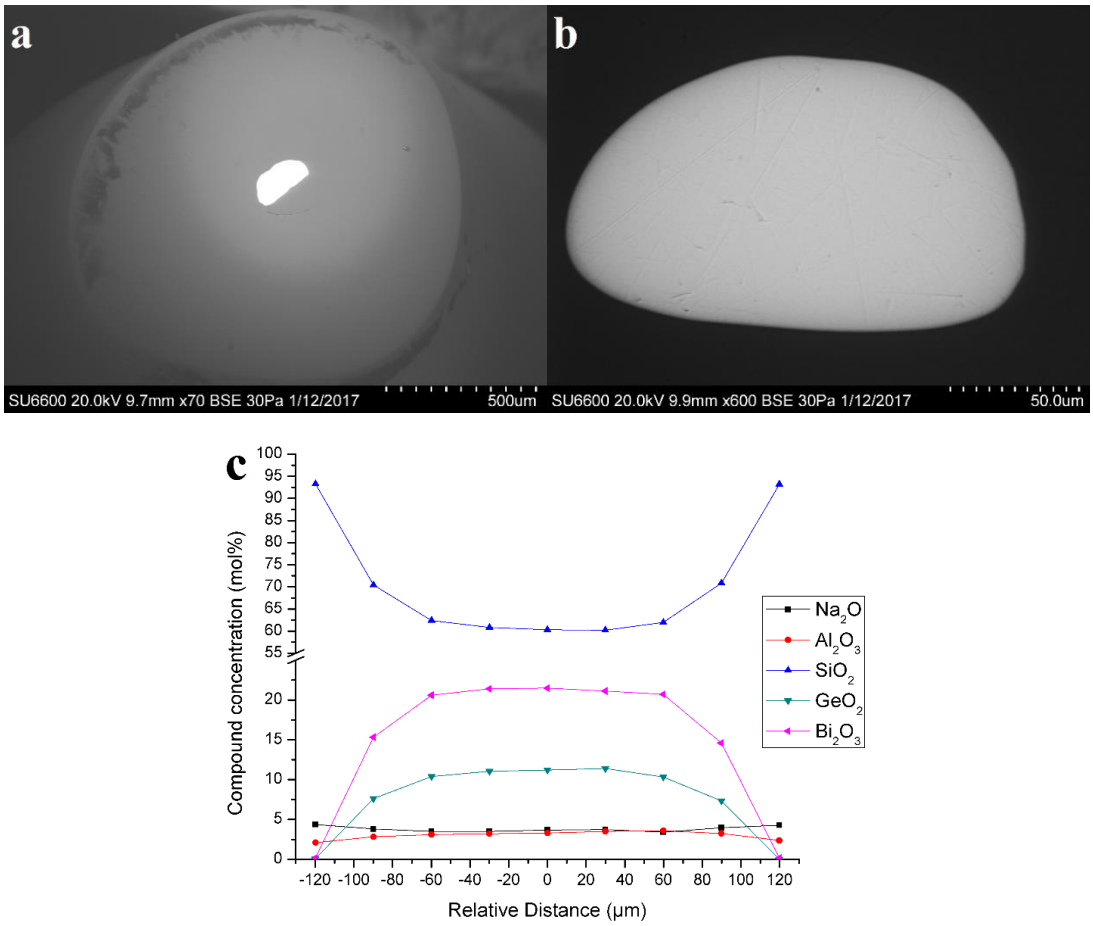

Figure III-11. a) SEM micrograph of the cross section from the tapered core seen in Figure III-10b. b) SEM micrograph of the tapered core, taken at higher magnification. c) EDX compound concentration profile across the tapers' core showing a composition gradient. The concentration at core center was found to be 62.7SiO_2-21Bi_2O_3-11.2GeO_2-3.2Na_2O-1.9Al_2O_3 at core center.

III.5.2. Second design: BGO pellet with Bi_2O_3 powder

In this second draw design, a white opaque core was observed first (approximate length of ~6 mm), connected to a large white core with a yellow tint (approximate length of ~15 mm), and followed by a golden clear core with large cracks in the cladding. Figure III-12 illustrates the SEM micrograph of the white opaque cane cross-section that was first obtained during draw. The cane was 4.4 mm diameter and the core was 400 µm diameter. Different types of microstructure were observed (line-like, dendrite-like and small homogenenous grains) and the composition of the grains was found to vary from the edge (40.7SiO_2-30.4GeO_2-26.7Bi_2O_3-0.9Al_2O_3-0.7Na_2O)

to the core center ($27.0SiO_2$-$41.6GeO_2$-$29.4Bi_2O_3$-$0.9Al_2O_3$-$0.9Na_2O$). The microstructures observed were similar to that observed in previous experiment employing solely a BGO single crystal (Chapter II section II.3.2). Hence, this part of the cane was attributed to the crystallization of the melt from the BGO single crystal precursor pellet.

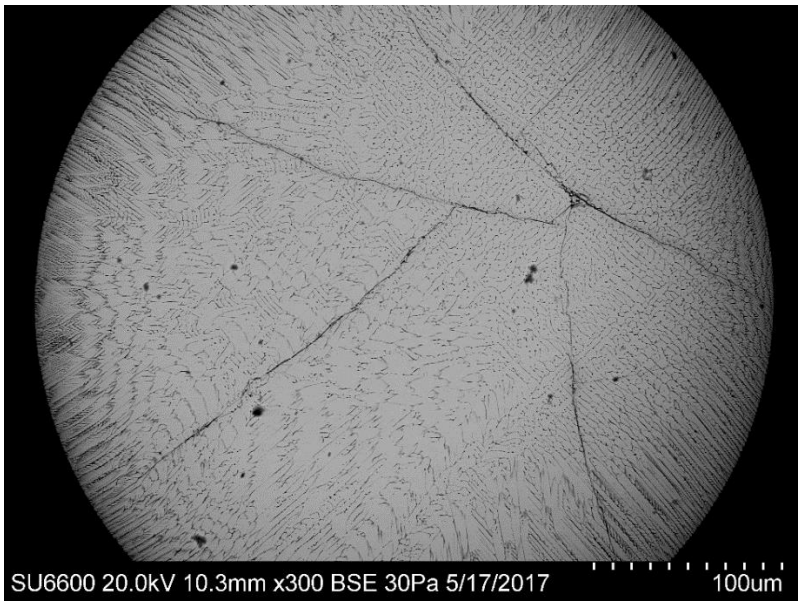

Figure III-12. SEM micrograph of a white core cane cross-section derived from the second design. Similar grain microstructures were observed to that obtained in Chapter II section II.3.2.

Figure III-13 depicts the core microstructure from the end of the white core cane with a yellow tint. The cane was 4.4 mm diameter and the core was 1.45 mm diameter. The observed core microstructures were seen to evolve from long elongated grains (~68 µm length) to smaller grains (~10 µm length) to line-like grains as one moves outwards from the core center. As was shown in Chapter II, the microstructure evolution across the cross-section was a consequence of the gradual change of bismuth oxide concentration across the core melt, whereby large homogeneous grains were grown from bismuth-rich melt and line-like grains were grown from bismuth-poor melt. The gradual change in bismuth concentration across the core was further

demonstrated by EDX composition analysis, where the composition of the large grains at core center was found to be $54.7SiO_2$-$4.0GeO_2$-$40.3Bi_2O_3$-$0.6Al_2O_3$-$0.4Na_2O$ and that of the line-like grains to be $40.5SiO_2$-$29.6GeO_2$-$28.0Bi_2O_3$-$0.9Al_2O_3$-$0.8Na_2O$. Furthermore, it was observed that the matrix (or grain boundaries) were bismuth-rich over the major part of the core (with >60mol% Bi_2O_3 around core center), indicating that the grains were grown from a (very) bismuth-rich melt composition. Interestingly, this demonstrated that the melt composition was too rich in Bi_2O_3 to be able to form a single phase over the whole core volume. Further tuning of the initial preform composition and/or design should allow obtaining a closer core melt composition to that of BSO. One further notes that there was a composition in the core that demonstrated a BSO stoichiometry as seen from the single phase "crystal ring" close to the cladding interface. Again, this shows that the control of the diffusion/extraction of the Bi_2O_3 molecules in the core was the limiting mechanism towards the formation of a single phase BGSO crystal core.

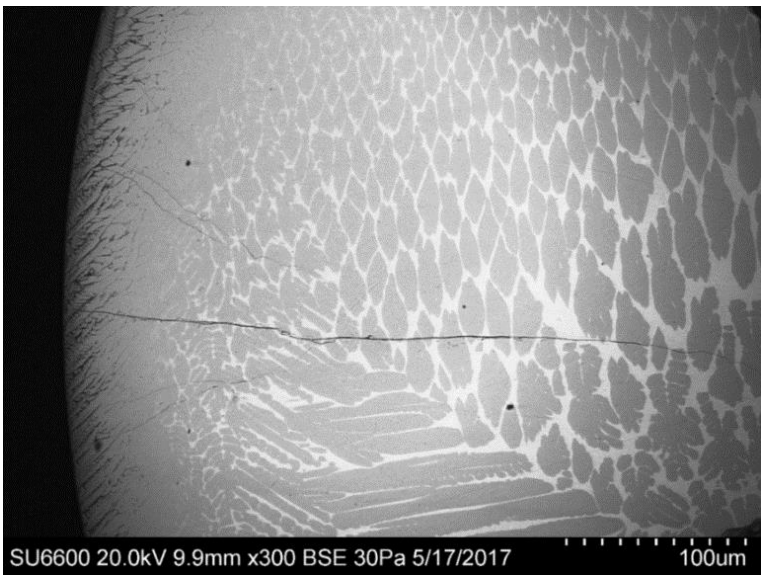

Figure III-13. SEM micrograph of the white core (with yellow tint) cane cross-section end derived from the second design. Grains were observed to be grown from a bismuth-rich melt.

Information about the microstructure evolution along the longitudinal axis between the white core cane (beginning of draw, Figure III-12) and the white core cane with a yellow tint (end of draw, Figure III-13) was gathered using SEM. The white core cane was polished at different stages starting from the end of the cane (Figure III-13) in order to study the microstructure evolution along the longitudinal axis. Figure III-14 illustrates the SEM micrographs of the different core cane cross-sections obtained at different positions along the longitudinal axis of the core starting from the end of the cane. The core exhibited small homogeneous grains and few elongated grains first, surrounded by bismuth-rich grain boundaries (Figure III-13, Figure III-14a and Figure III-14b). Then, large homogeneous grains were observed in the core with a structure close to a single phase core (Figure III-14c). Next, the core showed a full single phase core (Figure III-14d and Figure III-14e). Finally, the core exhibited very small homogeneous grains surrounded by bismuth-poor grain boundaries. It was observed that the surface area occupied by the bismuth-rich grain boundaries decreased as one goes towards the beginning of the cane, and consequently, the surface area occupied by crystals in the core increased to leave a single phase core at a certain point during draw. This clearly showed that there was a moment during draw where the composition of the core was in the very vicinity of the BGSO stoichiometric composition. Figure III-15 illustrates the composition evolution of the core center grains along the longitudinal axis. The grains' composition was seen to evolve from a low GeO_2 content towards a larger GeO_2 content as one goes towards the beginning of the cane. This demonstrated that, during the draw, the grains grew from a melt composition that was germanium-rich at first and then towards a melt composition that was silica-rich at last.

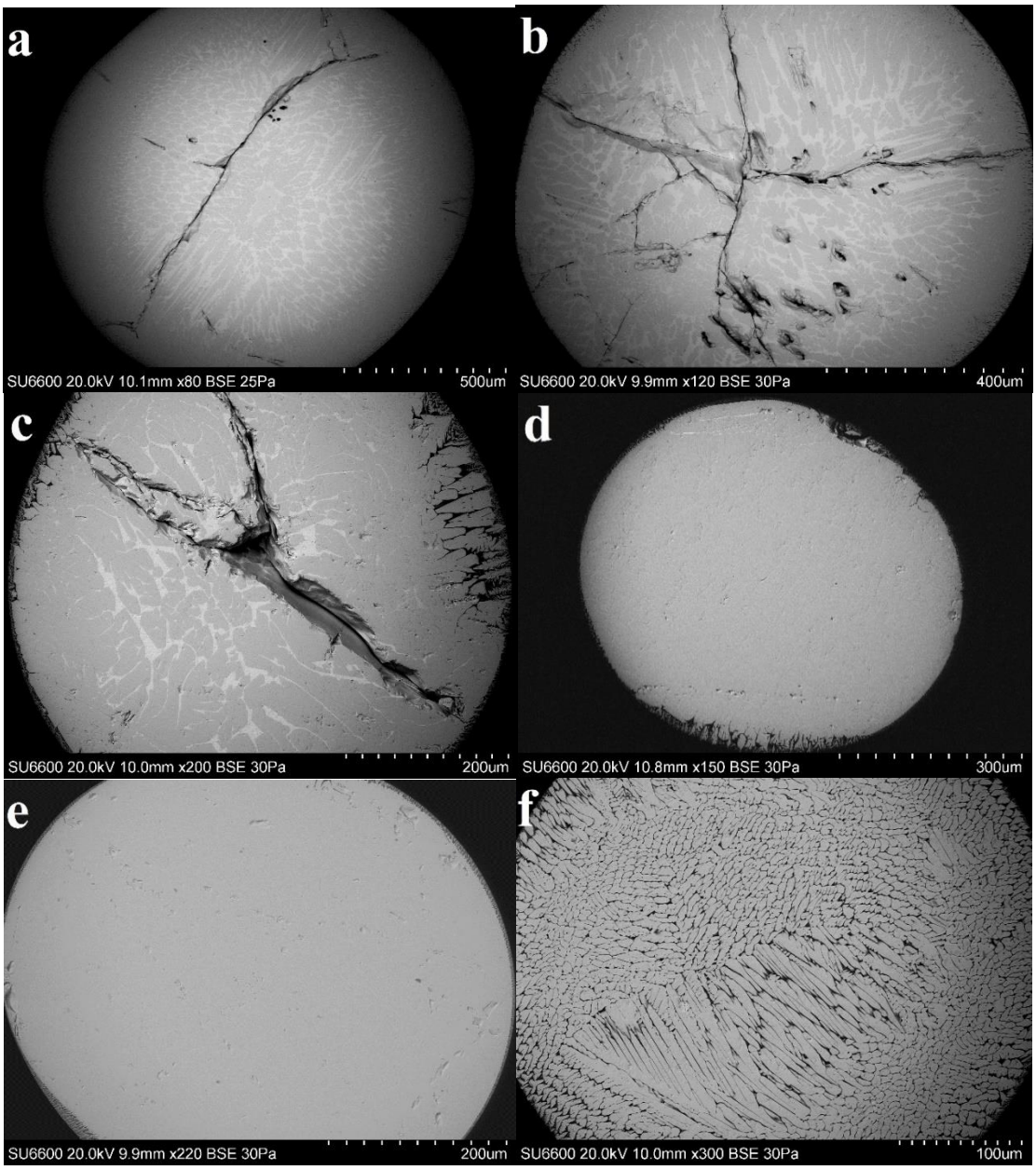

Figure III-14. SEM micrographs of different core cross-section taken along the white core cane (with yellow tint) derived from the second design. Cross-section micrographs taken at a position of (a) 1500 µm, (b) 3500 µm, (c) 6500 µm, (d) 7000 µm, (e) 7500 µm, (f) 9000 µm along the length of the white core cane, starting from the micrograph sample seen in Figure III-13. The core sizes were 1320 µm in (a), 1065 µm in (b), 700 µm in (c), 610 µm in (d), 560 µm in (e), 470 µm in (f).

The observed microstructure and grain composition evolutions allowed to explain the draw as follows. The BGO single crystal pellet melted and interacted with the glass cladding, leaving a melt enriched in SiO_2 and depleted in Bi_2O_3 and GeO_2. This

lead to the formation of BGSO crystals upon draw with the observed characteristic microstructures of crystal growth taking place from a bismuth-poor melt (i.e., line-like, dendrite-like and small homogeneous grains) as explained in Chapter II section II.3.2.1. Then, the BGO melt interacted with the bismuth-rich melt that was on top of it. This bismuth-rich melt provided a surplus of Bi_2O_3 molecules in the vicinity of the BGO melt and allowed the formation of a single BGSO crystal phase as seen in Figure III-14d and Figure III-14e[3]. Next, the BGO melt was gradually depleted (as seen by the gradual replacement of GeO_2 by SiO_2 in Figure III-15), and crystal growth took place from the bismuth-rich melt that was on top of it. This lead to the crystallization of large BGSO grains grown from a slightly bismuth-rich melt, and the apparition of bismuth-rich grain boundaries (Figure III-14c). At this point, the core melt was too rich in Bi_2O_3 to be able to form a single phase. From there (Figure III-14b and Figure III-14a), crystal growth took place solely from the bismuth-rich melt (as seen from the large SiO_2 content of the grains in Figure III-15) and, as a result, elongated grains and small homogeneous grains were grown in the core, surrounded by bismuth-rich (>60mol% Bi_2O_3) grain boundaries. For completion, it is worth noting that the yellow tint of the white core cane appeared at the position where bismuth-rich grain boundaries were seen, which was also the position were the core size was seen to increase. A large core size is known to originate from the melting of the Bi_2O_3 precursor powder due to its large volume expansion. This is an additional information that indicated that crystal growth took place from the bismuth-rich melt that was on top of the BGO melt.

[3] The EDX analysis did not give a stoichiometric BGSO composition for this single phase, and this was likely a result of the EDX instrumentation not detecting boron as mentioned in Chapter II section II.3.2.1.

Further observation of the composition profile of the grains across the core cross-section showed a very unusual trend (see Figure B-9 in Appendix B). SiO_2 (and GeO_2 respectively) was found in a larger (respectively lower) amount at the core center and a lower (respectively higher) amount at the core-cladding interface. This concentration trend was opposite to all drawn canes (SiO_2 is in most cases found in a lower amount at core center). This trend could be explained by the design employed, where the bismuth-rich melt being "poured" and drawn in the center of the BGO melt, in a similar way to the double-crucible method. Perhaps one can imagine that upon drawing, the BGO melted and adhered to the soft glass cladding with a shape that would be that of a positive meniscus in the neckdown region (due to surface tension between melt and glass clad). Upon drawing, this meniscus from the BGO melt could leave a "crucible-like" shaped melt with the bismuth-rich melt on top of it. This would thus leave a high amount of germanium at the core clad interface, and a high amount of silica at core center.

Overall, during this draw, the Bi_2O_3-rich melt above the BGO single crystal pellet interacted with the glass cladding to give a composition largely above the stoichiometry of BSO (or BGSO) in terms of Bi_2O_3 content (similarly to that observed in the homogeneous nucleation experiment in section III.4). This Bi_2O_3-rich melt further nucleated and grew on the grown crystals originating from the BGO single crystal pellet. Hence, this latter likely provided a path for reducing the thermodynamic energy barrier for nucleation of the Bi_2O_3-rich melt and confirmed the mechanism of heterogeneous nucleation. It is worth noting that the crystals were formed here upon cooling down as the core was drawn above the melting point of the BGO single crystal.

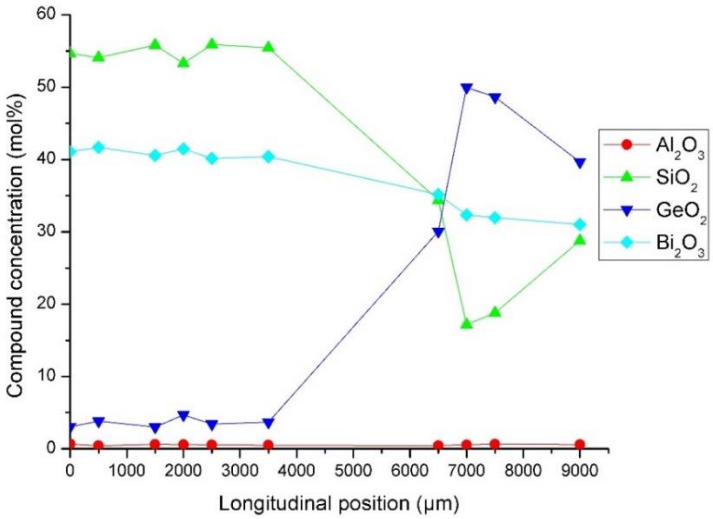

Figure III-15. EDX compound concentration profile of the center core grains along the length of the white core cane with a yellow tint. The position "0" corresponds to the center core grain composition obtained from EDX analysis carried on the core of Figure III-13; and it refers to the last section of the sample exhibiting crystallinity (i.e., end of the draw).

EBSD analysis gave further insight on the crystal plane orientation. Figure III-16 shows the IPF orientation maps along the X, Y and Z axis of the white core cane with a yellow tint shown in Figure III-13. The observed single color showed that the crystals grew along one single and common direction, indicating that the core was single crystal-like. Crystals were found to be grown in the [-230], [-5-32] and [115] directions along the X, Y and Z axis respectively. These planes were different than those of the BGO single crystal precursor and thus showed that crystals were grown from the melt, and the observed plane direction indicated that the starting plane surface from which they grew was random. Although Figure III-16e shows that there were three main different directions along which crystals were grown, more than 99% of the crystals analyzed grew along the same direction and this confirms the single crystal-like behavior of the core.

Further study of sample drawn from this design showed that the part of the cane following the crystalline core was a golden clear core, with a cane diameter of 4.1 mm

and a core diameter of 1.32 mm. This golden clear core was found to be amorphous and this suggested that there was a break in crystal growth. The composition at core center was found to be $50.1SiO_2$-$0.4GeO_2$-$46.6Bi_2O_3$-$1.2Al_2O_3$-$1.7Na_2O$. This composition indicated that the melt was still bismuth-rich and that crystal growth should have sustained (as was seen in the preceding white cores showing crystal growth from a bismuth-rich melt). Obviously, the driving force conditions were not met anymore and a change in growth rate took place where it was nullified. From the nucleation and growth theory, a few cases can be envisioned. One could think that there was not enough energy provided for the molecules to attach at the growth front. This is refuted by the fact that the drawing parameters were kept constant (temperature, draw speed, cane diameter) and thus, if there was enough energy to grow crystals in the core volume adjacent to it, this means that there was enough energy provided for the reaction to take place at all times. Thus, the nullification of crystal growth was likely a kinetic factor. Hence, this means that there was a large decrease in the concentration of reactants at the liquid-crystal interface that prevented crystal growth to sustain (i.e., kinetics of mass transport to the growth front). Perhaps the crystal growth became a diffusion-limited mechanism due to an increase in viscosity of the melt. An increasing SiO_2 content from the silica cladding incorporation increases the viscosity in the Bi_2O_3-SiO_2 system from 10^{-2} Pa.s to $10^{-0.35}$ Pa.s at 1080°C (values deduced from [22]). Thus, the growth rate was lowered by more than one-fold and could have prevented further crystal growth. A slower drawing speed would likely improve the kinetics of crystallization (i.e., mass transport), as diffusion is a time-dependent phenomenon and would allow more time for the atoms to diffuse to the growth front by lowering the quenching rate.

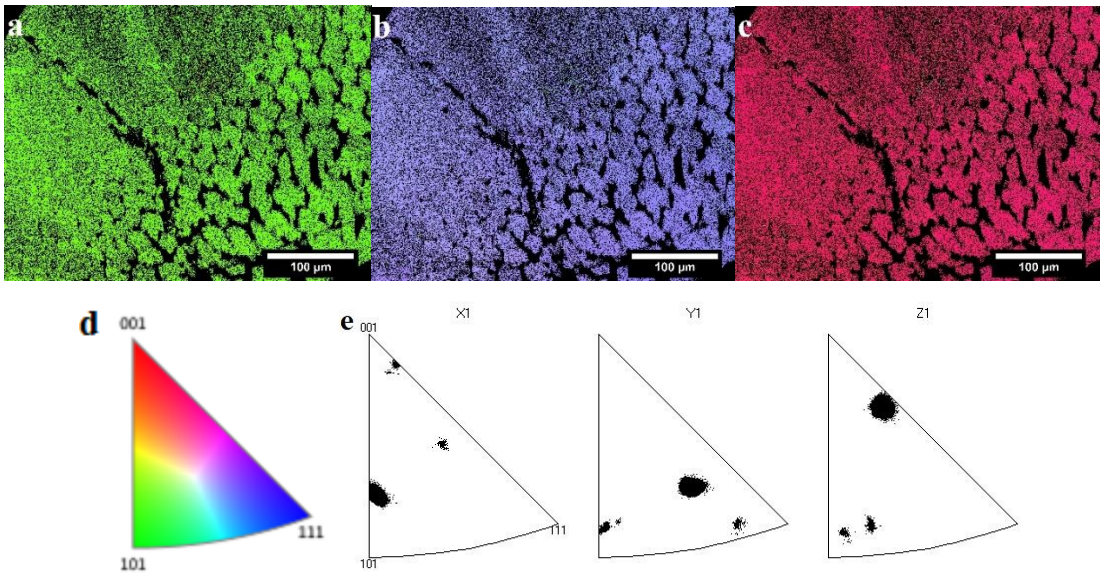

Figure III-16. IPF orientation maps along the a) X-, b) Y- and, c) Z-axis of the white core cane with yellow tint drawn using the second design. d) Stereographic triangle showing the orientation color-scale. e) Color matching between each pixel in IPF each orientation map and the orientation color-scale, showing heavy preferred crystal orientation along each axis (i.e., single crystallinity-like).

Interestingly, the mechanism of crystallization from the BGO crystal pellet melt itself was very intriguing (as was also seen in Chapter II section II.3.2). Two mechanisms can be envisioned for this observation: whether the precursor BGO single crystal did not fully melt and crystal seeds remained in the melt for heterogeneous nucleation process to take place; or, the structure of the melt closely resembled that of BGO such that the thermodynamic barrier for homogeneous nucleation was reduced. The non-melting of the BGO single crystal precursor was refuted due to the obtained core dimensions (400 µm diameter while starting with a 3 mm diameter crystal). Additionally, a different core structure would have been observed if the crystal precursor did not melt as was seen in another experiment (see the "complementary experiment for the interaction of a large BGO single crystal precursor in Appendix B). Hence, the crystallization likely took place from a molten core phase. Different authors mentioned that the melt structure influenced the

formation of metastable and/or stable phases (see Gévay [23] and references therein, and Zhereb, et al., [24]), whereby the overheating magnitude of the melt and the quenching rate played a role on the crystallization behavior. Small overheating magnitude and larger quenching rates were mentioned to be favoring the crystal growth of stoichiometric BGO. Although in their experiment the precursor material was a Bi_2O_3-GeO_2 powder mix rather than a BGO crystal, it was mentioned that near the melting point of BGO a network of [GeO_4] tetrahedrons and distorted [BiO_6] octahedrons close to the eulytine structure was likely to remain in the melt, thus leaving a pre-crystalline order. In our case, the starting material was a BGO single crystal rather than a stoichiometric powder mix and, perhaps in a similar fashion to Zhereb, et al. [24] findings, some pre-crystalline order remained in the melt and favored nucleation and growth upon cooling.

It is worth mentioning that BGO crystals were grown from a BGO stoichiometric glass [25], meaning that BGO crystals can be grown through homogeneous nucleation since no seeds were introduced in the glass. In contrast, it was mentioned in the literature that BGO cannot be grown from a melt using the standard single crystal growth techniques [7] despite the very slow growth rate employed ($mm.hr^{-1}$). These two cases, in turn, means that the growth of BGO/BSO seems to be sensitive to cooling and heating stages, where homogeneous nucleation upon cooling cannot take place, perhaps because the structure of the melt is not close enough to that of the eulytine structure. On the other hand, perhaps the structure of a glass brings a very short crystalline order that allows the structural units formed to act as seed and thus "homogeneous" nucleation can take place upon heating.

III.6. Formation of BSO crystalline optical fibers via phase transformation in DURAN®

As mentioned in the introduction, a phase transformation reaction reported in the literature could be used as a path for the fabrication of BSO crystalline core fibers. For that purpose, a two-step process was necessary where the first part consisted in the fabrication of a cane containing Bi_2SiO_5 crystals, and the second part consisted in redrawing the cane to fiber size and investigate if the reaction could be favored.

In order to fabricate a cane with the desired Bi_2SiO_5 crystals in its core, three millimeter pellets of composition $99.5Bi_2O_3$-$0.5CeO_2$ were drawn in DURAN® at 960°C to a four millimeter cane diameter (CeO_2 was added as an oxidizing agent, see details in Chapter IV). Figure III-17a, Figure III-17b and Figure III-17c depicts SEM micrographs of a yellow core cane cross section (760 µm core). Various microstructures were observed in the core: large homogeneous phases at the core-clad interface of the core (in lower left part of Figure III-17a and Figure III-17c), needle-like microstructures in Figure III-17b and, blob-like microstructures in between needles in Figure III-17c. EBSD analysis was performed to observe the crystalline nature of each microstructures. Figure III-18 illustrates the EBSD phase match picture obtained on the same core as Figure III-17. The large homogeneous phases were found to correspond to the stable BSO crystals, the needle-like microstructures to the metastable Bi_2SiO_5 crystals, and the blob-like microstructures to δ-Bi_2O_3 (also confirmed with XRD, see Figure B-4 in Appendix B). Note that in this case no BGO single crystal was utilized as part of the precursor in the draw design, and hence the grown crystals were entirely of the BSO nature as compared to all crystalline phases previously obtained in Chapter II and this Chapter.

All the various crystalline phases observed portray the dynamics of the crystallization in draw and the reactions that took place in the core. An explanation for this dynamic behavior may be found as follows. First, the Bi_2O_3 precursor powder did not melt entirely and left blob-like microstructures in the core. The observed phase (δ-Bi_2O_3) is the stable high temperature phase that results from the solid-solid $\alpha \rightarrow \delta$ phase transition of the Bi_2O_3 powder precursor [11]. Hence, this solid-solid phase transformation took place, but not enough energy was brought to the system to reach the melting temperature of the δ phase. Thus, these crystals were not melted and this was shown to be a result of the powder processing design employed ("pressed powder" vs "poured powder") as explained in Chapter IV. Secondly, the starting precursor powder did not include Bi_2SiO_5 nor BSO crystals, and thus the Bi_2SiO_5 and BSO crystals were formed through the reaction of Bi_2O_3 with SiO_2, which was incorporated from the glass cladding. BSO crystals seemed to be formed solely at the core-cladding interface, whereas the Bi_2SiO_5 crystals were seen to grow throughout the whole core. This difference in spatial arrangement could originate from a compositional gradient, whereby the silica content at the core cladding interface was close to the BSO stoichiometry and favored their formation. Nonetheless, Bi_2SiO_5 crystals were also seen at the core-cladding interface where the composition was similar, and, in addition, both crystal phases can crystallize from off-stoichiometric melt as seen in previous sections. Hence, this difference in spatial arrangement was not justified by compositional gradient and, the reason for this difference is unknown. Perhaps this observation does not find any explanation and, the BSO crystal growth was random and appeared to be as it is.

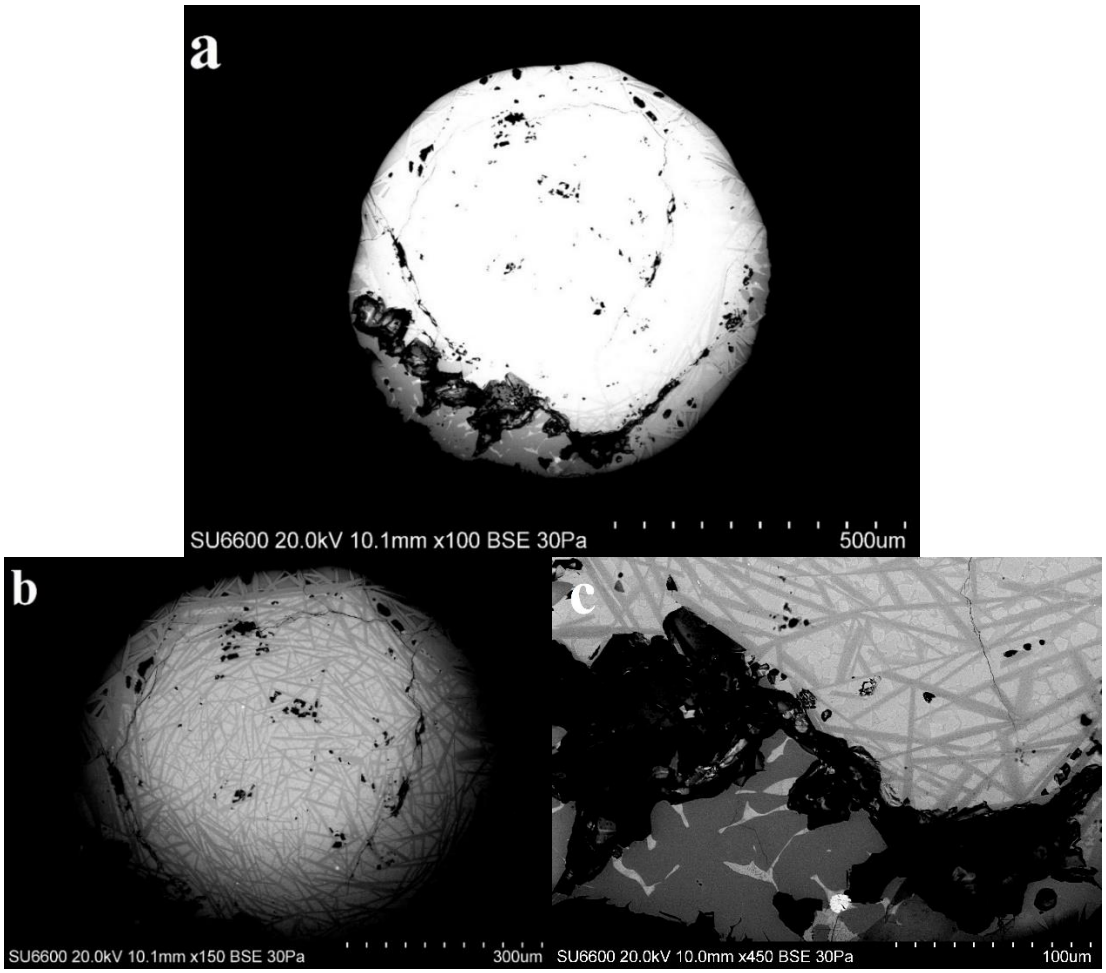

Figure III-17. a) SEM micrograph of a yellow core cane cross section of Bi_2O_3 powder drawn in a borosilicate glass cladding. The cane was 4.0 mm diameter and the core was 760 µm diameter. b) SEM micrograph of the same core with higher contrast and, c) SEM micrograph taken at the core-clad interface of the same core with higher magnification. Various microstructures were observed: homogeneous grains, needles and, blob-like structures in between needles.

It is worth noting the crystallization mechanism of the metastable Bi_2SiO_5 crystals. Various reports have mentioned the crystallization and growth of the metastable phase, whether it was from the cooling of a melt [7], [26] or through the annealing of a glass [6], [25], [27]. The crystals were thus grown spontaneously without the necessity of a seed. In our case, it was previously observed in section III.4 that the quenching of a melt in the crystallization range of Bi_2SiO_5 crystals did not lead to the formation of the metastable phase. Hence, it is unlikely that the metastable crystals

observed here were grown through homogeneous nucleation, as the quenching rate was shown to be too large for spontaneous nucleation (and growth) to take place. Perhaps the surface of the δ-Bi_2O_3 crystals provided enough driving force for the Bi_2SiO_5 crystals to crystallize onto. One face (b or c) of the orthorhombic Bi_2SiO_5 unit cell (a=15.21 Å, b=5.48 Å, c=5.33 Å) could have grown on that of the cubic δ-Bi_2O_3 phase (a=5.66 Å) such that the lattice mismatch between the two crystals was not an impediment to crystal growth. It is also worth mentioning that the Bi_2SiO_5 and BSO crystals were formed using the "pressed powder" design, which likely involved an increased pressure in the core as explained in Chapter IV section IV.2. This increased pressure in the core may be at the origin of the observed Bi_2SiO_5 and BSO crystal formation. It is generally known from the Clausius-Clapeyron equation (and associated P-T phase diagram) that an increase in pressure correlates with an increase in melting (or crystallization) temperature. And hence, at constant temperature, a sufficient increase in pressure can allow one to cross the liquid-solid coexistence curve of a compound from the liquid region to the solid region in the P-T diagram. Hence, the increase in pressure in the core was perhaps large enough to induce crystallization of the observed BSO and Bi_2SiO_5 phases. Note that in this case, the crystallization would have taken place spontaneously. Although not refuted, it is unlikely that the BSO crystals were grown heterogeneously due to the large lattice mismatch between the cubic BSO crystals (a=10.28 Å) and the cubic δ-Bi_2O_3 phase (a=5.66 Å).

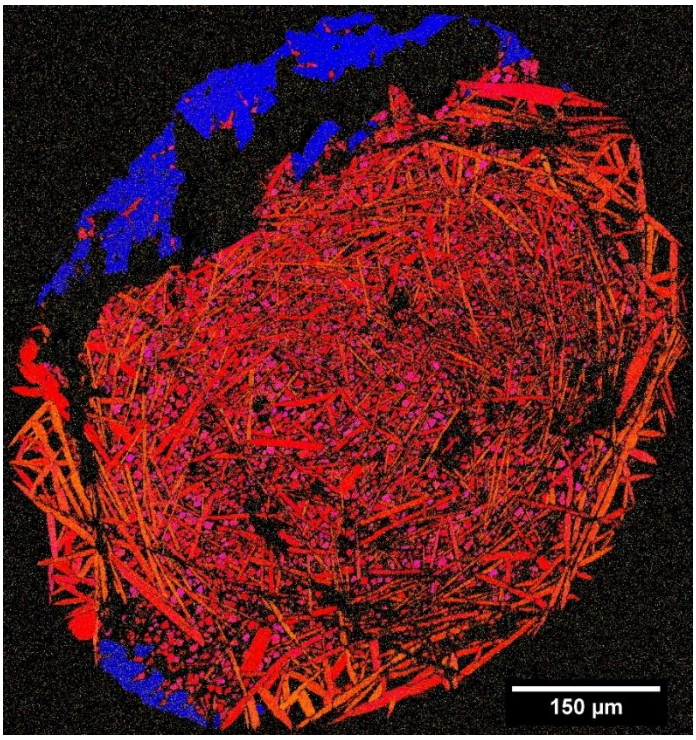

Figure III-18. EBSD phase color matching micrograph of the yellow core cane cross section in Figure III-17. Legend: blue = $Bi_4Si_3O_{12}$, red = Bi_2SiO_5, pink = α-Bi_2O_3, orange = δ-Bi_2O_3. The homogeneous grains, needles, and blobs in Figure III-17 were matched respectively with BSO, Bi_2SiO_5 and δ-Bi_2O_3, and α-Bi_2O_3.

The cane was redrawn to fiber at 950°C and a speed of 20 $m.min^{-1}$. A coating was not applied on these fibers as they exhibited lumps upon drawing (Figure III-19a), which got stuck in the coating die and prevented drawing fibers in normal conditions. Figure III-19b illustrates a SEM micrograph of a fiber core cross section, and a single grain phase was observed (in bright). The fiber was 130 µm diameter and the core was 50-80 µm diameter with a highly-deformed shape.

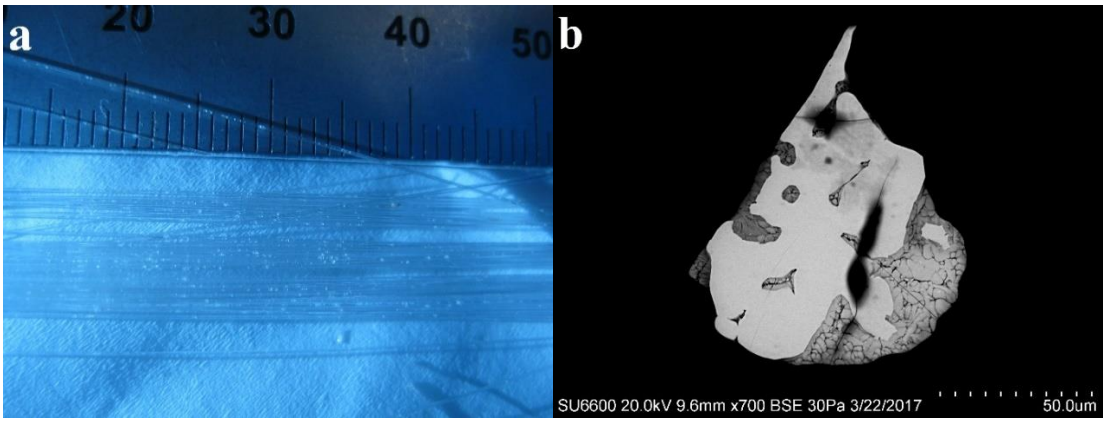

Figure III-19. a) Picture of the drawn fibers from the cane. White small chunks were seen in the fibers. b) SEM micrograph of a fiber cross section drawn from the cane seen in Figure III-17. The core was highly deformed and showed a single BSO grain (in bright).

Figure III-20 illustrates the PXRD diffractogram carried out on the fibers. The peaks were matched with the eulytine structure of BSO (JCPDS card 01-076-1726) and no other phases were detected. The peaks were seen to be shifted from the reference card by 0.03°. These shifts are very small and might indicate the substitution of boron, soda or alumina in the crystal structure. Durif-Varambon [19] mentioned that the formation of eulytine structures possessing different molecular groups than the known bismuth and silica groups was feasible. However, he mentioned two conditions: the first one is that the substitution of the $(SiO_4)^{4-}$ tetrahedral groups needed to be performed using other tetrahedral groups (XO_4) that would be as regular as possible (X= P, As, V, S, Cr); the second condition is to compensate the charge balance induced by the (XO_4) group by replacing the bismuth cation by another cation of close ionic radius and that can adopt the same oxygen coordination. In our case, the boron or aluminum atom could form regular tetrahedral group $(BO_4)^{5-}$ and $(AlO_4)^{5-}$ that could replace the $(SiO_4)^{4-}$ (sodium atoms do not form tetrahedral groups with oxygen) with the following substitution scheme: $3(SiO_4)^{4-} + 4Bi^{3+} => 3(XO_4)^{5-} + Bi^{3+} + 3M^{4+}$ with X=B, Al and M a tetravalent cation. As seen,

the need of a tetravalent cation with similar ionic radius to Bi^{3+} is necessary to compensate for charges. However, no atoms in the draw satisfy these requirements. Thus, it is unlikely that boron and aluminum substitute in the eulytine structure here. Furthermore, bismuth atoms are known to take a +5 oxidation state and the charge balance could be satisfied if bismuth atoms acquired a pentavalent state [$3(SiO_4)^{4-}$ + $4Bi^{3+}$ => $3(XO_4)^{5-}$ + $3Bi^{5+}$]; however, this would require the oxidization of the trivalent atom, which is unlikely as the bismuth atoms easily thermally reduce even in air as mentioned in Chapter IV section IV.5.

It is worth noting that, none of the metastable phase Bi_2SiO_5 or the δ-Bi_2O_3 crystals observed in the yellow core canes were seen in the fibers, as confirmed by PXRD. It was seen that in the obtained core canes the core did not melt properly; hence, if the core did not melt as well upon redraw to fiber, this would mean that the Bi_2SiO_5 crystals (similarly with Bi_2O_3 crystals) found in the cane would have not melted and stayed as-is. However, they must have melted since they were not found in the fibers. The Bi_2SiO_5 crystals were reported to melt at 835-850°C (as seen in Figure III-5) or to transform to the more stable crystal upon heating at 885°C [6], [8]. The phase transformation could not be evidenced due to the BSO crystals being already present in the core cane that the fibers were drawn from. The BSO crystals observed from the cane were likely not melted upon redraw due to the low drawing temperature employed (i.e., below their melting point). Hence, the BSO crystals of the cane stayed as-is upon redrawing to fiber (which in turn made the fiber lumpy). Nevertheless, one notices that the size of the crystal observed in the fiber (65-110 µm) was smaller than those observed in the cane (110-450 µm). This could potentially indicate that phase transformation was taking place as larger core crystal would have been observed if

these large BSO crystals did not melt. However, this conclusion cannot be made due to the dynamics of crystallization taking place during cane draw and the unknown about the core phases and crystal sizes in the canes from which the fibers were drawn.

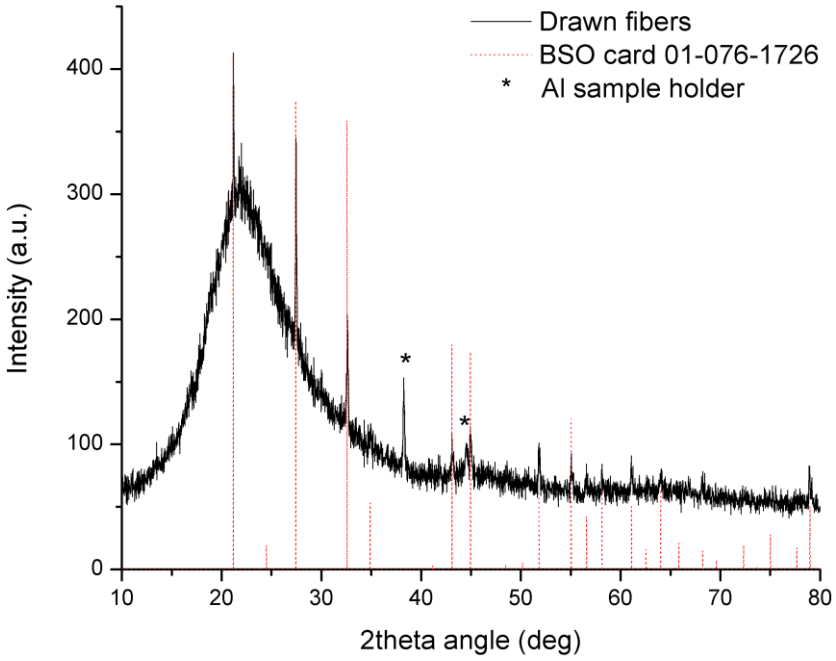

Figure III-20. XRD diffractogram performed on the drawn fibers. Crystalline peaks were observed and matched the eulytine structure $Bi_4Si_3O_{12}$ (JCPDS 01-076-1726). The large halo represents an amorphous phase (glass cladding).

EBSD analysis was performed in addition to XRD in order to investigate the crystal plane orientation. Figure III-21 shows the IPF orientation maps along the X, Y and Z axis. The presence of BSO crystals was noted and the large bright grain observed in Figure III-19b was shown as a single crystal. The single crystal was found to be grown in the [-310], [-1-32] and [135] directions along the X, Y and Z axis respectively. These planes were different than the ones observed in the canes (see Figure B-5 in Appendix B) and could indicate the BSO crystals from the cane were of a different origin (i.e., grew from the phase transformation). Nonetheless, one cannot make this conclusion as the BSO crystal orientation from the drawn canes was unknown.

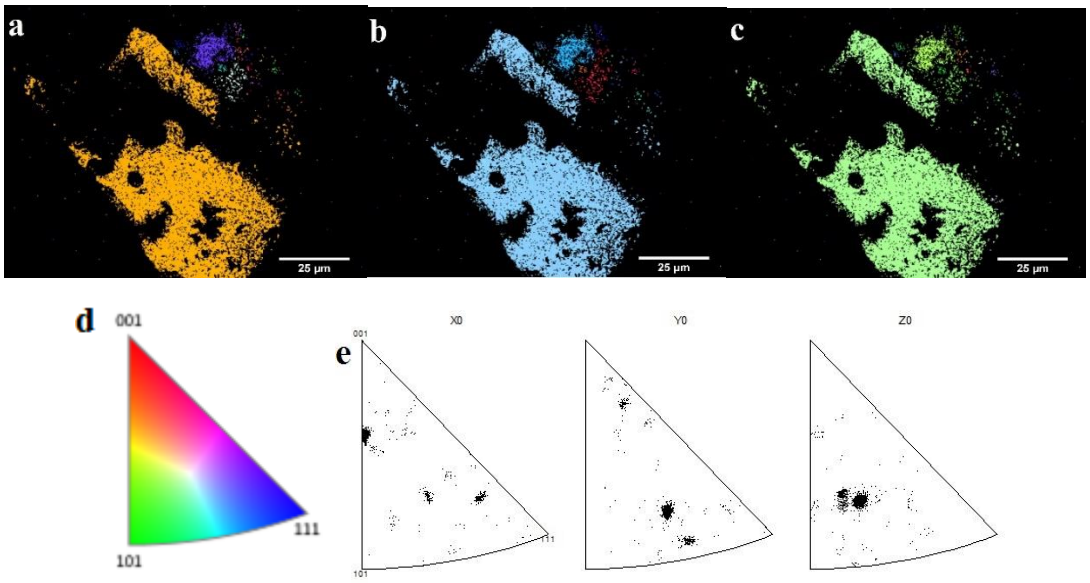

Figure III-21. IPF orientation maps along the a) X-, b) Y- and, c) Z-axis of the fibers drawn from canes containing Bi_2SiO_5 crystals. d) Stereographic triangle showing the orientation color-scale. e) Color matching between each pixel in IPF each orientation map and the orientation color-scale, showing heavy preferred crystal orientation along each axis (i.e., single crystallinity-like).

III.7. Formation of BSO crystalline optical fibers via phase transformation in AR-GLAS®

Further investigation of the phase transformation was carried out, yet employing a soda-lime silicate glass cladding tube. The AR-GLAS® cladding glass was used here for its better mechanical properties and larger coefficient of thermal expansion (CTE) that reduces the CTE mismatch with BSO. Additionally, it offers the opportunity to investigate the effect of temperature (and composition) on the crystallization behavior of the Bi_2O_3-SiO_2 system.

Three millimeters pellets of composition $89.8Bi_2O_3$-$10B_2O_3$-$0.2CeO_2$ were prepared and sleeved inside an AR-GLAS® cladding glass tube (B_2O_3 was added as a melting accelerant), and drawn at 885°C with a speed of 5 $mm.min^{-1}$. Figure III-22a depicts the SEM micrograph of a white core cane with a core of 480 µm diameter. Needle-like and dendrite-like microstructures were observed. Figure III-22b exhibits

the PXRD diffractogram of the white core cane and the metastable γ-Bi_2O_3 phase was detected. The needles were known to correspond to Bi_2SiO_5 metastable crystal from a similar experiment despite not being shown through PXRD (see Figure B-6 in Appendix B), and hence the dendrite-like structures were assigned to the γ-Bi_2O_3 phase. It is interesting to note that BSO crystals were not formed in this case as compared to the cane drawn in the borosilicate system.

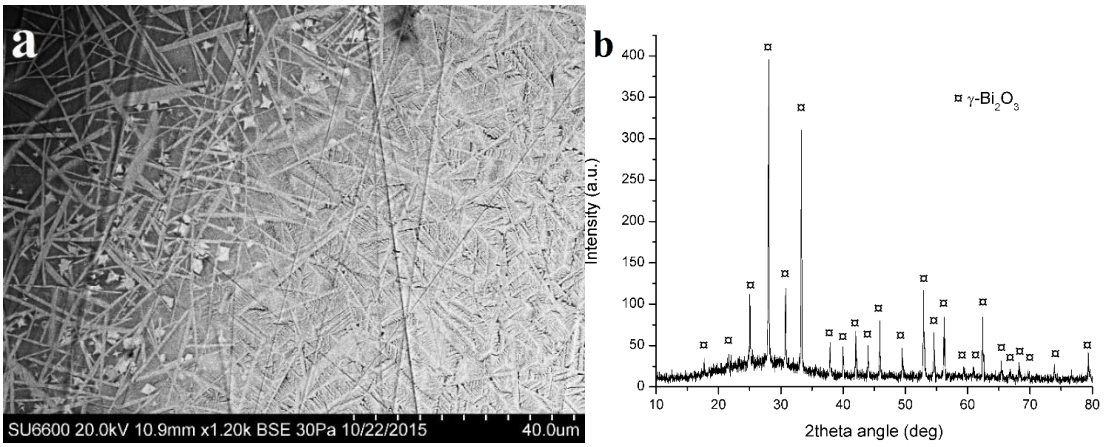

Figure III-22. (a) SEM micrograph of a white core cane cross section derived from Bi_2O_3-B_2O_3-CeO_2 in AR-GLAS®. Needles are observed at the core-cladding interface on the top-left corner, as well as dendrite-like microstructures at the bottom right corner that corresponds to the center of the core. (b) XRD diffractogram obtained from the white core cane drawn from AR-GLAS® preform to 2.5 mm cane. The γ-Bi_2O_3 phase (JCPDS 01-074-1375) was identified.

The cane was redrawn to fiber at 885°C with a speed of 3 $m.min^{-1}$. Figure III-23a depicts the SEM micrograph of the obtained fibers, where needle microstructures were observed. It is interesting to note that no dendrite structures were observed and only needles were seen in the core. This indicated that the Bi_2O_3 crystals observed in the cane were fully melted upon drawing to fiber, and part of the core melt reacted with the incorporated SiO_2 to form the metastable phase. The needles were confirmed as the Bi_2SiO_5 phase due to the characteristic peak at 11.8° as seen from the PXRD diffractogram performed on the fibers (Figure III-23b). Yet, two peaks found in the

XRD diffractogram (at 19.1° and at 28.2° in 2-theta angle) could not be attributed to any phase (whether bismuth silicate or bismuth borate) due to the lack of well-defined peaks.

Although previous reports have demonstrated that the metastable crystals (Bi_2GeO_5/Bi_2SiO_5) could be transformed upon heating to the desired BGO/BSO crystals [6], [8], [27], it is interesting to note that, in this present case, the phase transformation of the Bi_2SiO_5 crystals to the more stable BSO phase did not take place as the BSO crystal phase was not detected with XRD. Instead, further growth of the metastable phase was observed upon redraw. In comparison to the draw performed in the borosilicate preform in the previous section III.6, the drawing temperature of 885°C in the present case was likely too close to the phase transformation temperature. Thus, the thermodynamic driving force for the solid-solid phase transformation was not met. Again, it is worth noting that the crystallization behavior of the metastable phase in the cane was intricately related to the powder precursor design (i.e., pressed powder pellets) since crystallinity was not observed in core composition close to Bi_2SiO_5 as described in section III.4. The crystallization mechanism of the metastable phase was whether through heterogeneous nucleation due to the non-melting behavior of the Bi_2O_3 powder (the latter which offered a surface for the metastable phase to grow onto) or through homogeneous nucleation induced by the pressure phenomena as mentioned in the previous section III.6.

It is worth mentioning that drawing in the soda lime silicate glass cladding offered the opportunity to isolate the crystallization of the metastable Bi_2SiO_5 crystals. The drawing temperature provided sufficient thermal energy to meet the activation energy

requirements for nucleation of Bi_2SiO_5 ($E_{a\ Bi2SiO5}$=14.8 kJ.mol^{-1} [27]), but not enough thermal energy to meet those for nucleation of BSO crystals ($E_{a\ BSO}$=34.1 kJ.mol^{-1} [27]). The metastable phase is polar acentric and could thus also be used as a nonlinear, electro-optic material as mentioned in [28].

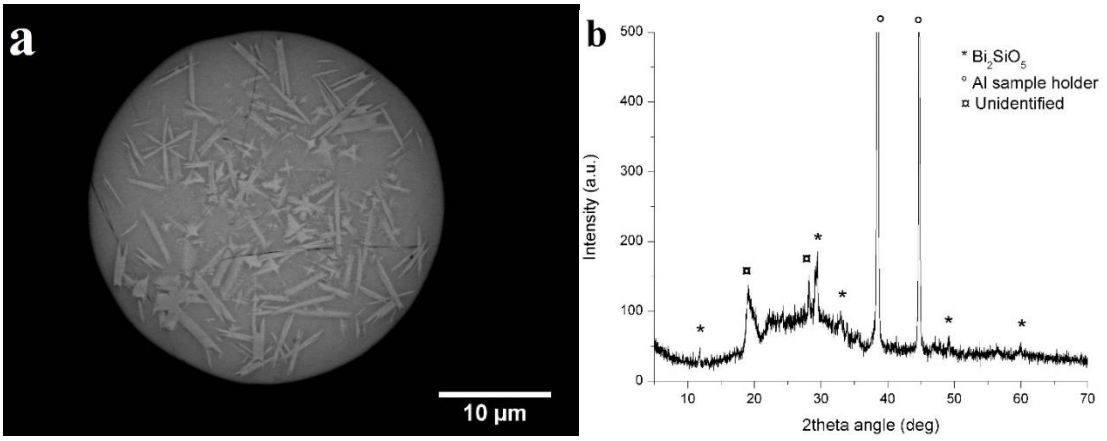

Figure III-23. (a) SEM micrograph of a fiber cross section drawn from the white core cane. Needles microstructures corresponding to Bi_2SiO_5 were discerned. (b) XRD diffractogram obtained from fibers drawn from the cane shown in Figure III-22. The metastable phase Bi_2SiO_5 (JCPDS 01-075-1483) was identified.

III.8. Conclusions

In this Chapter, the mechanisms for BSO (or BGSO) crystallization during cane and fiber draw using the molten core method were investigated through various draw design, and the effect of precursor powder design on the core crystallization behavior was underlined. A first design employing Bi_2O_3 powder inserted in borosilicate cladding tube was used to investigate homogeneous nucleation. Canes were drawn and showed compositions close to that of BSO and Bi_2SiO_5 crystals (46.7SiO_2-50.1Bi_2O_3-1.2Al_2O_3-2.0Na_2O and 54.4SiO_2-40.7Bi_2O_3-1.5Al_2O_3-3.4Na_2O respectively). Despite their close stoichiometry to Bi_2SiO_5 or BSO crystals, these cores were amorphous and homogeneous nucleation was refuted as a mechanism for crystal growth in the Bi_2O_3-SiO_2 system using the molten core method.

Heterogeneous nucleation was investigated using two designs. A first design employing Bi_2O_3 powder along with BGO seeds packed in a borosilicate glass cladding and a second design employing Bi_2O_3 powder inserted on top of a BGO crystal pellet in a borosilicate glass cladding both demonstrated the formation of BGSO crystals in the core cane. It was shown that BGO seeds were necessary to overcome the thermodynamic energy barrier for nucleation and, heterogeneous nucleation was confirmed as a crystal growth mechanism in the Bi_2O_3-SiO_2 system using the molten core method. The crystal growth was shown to be controlled by the thermodynamic barrier imposed on the system rather than by the kinetic barrier imposed by the large quenching rate. Additionally, a single phase core was obtained with the second design, thus showing the possibility of fabricating single phase core canes using the molten core method.

Finally, the growth of BSO crystals through the solid-solid phase transformation $2Bi_2SiO_5 + SiO_2 \Rightarrow Bi_4Si_3O_{12}$ was investigated using Bi_2O_3 pressed powder pellets in a borosilicate glass cladding. Although BSO crystals were obtained in fibers, these latter were drawn from canes that contained both stable BSO and metastable phases, and thus the reaction could not be validated. The presence of both stable and metastable phases in cane underlined the complexity of the Bi_2O_3-SiO_2 binary system and its crystallization dynamics. Crystallization of the metastable phase Bi_2SiO_5 was also demonstrated using the pressed powder pellet design in a soda lime silicate glass cladding. In this case, the metastable phase was only grown and it was shown that its formation in the Bi_2O_3-SiO_2 phase diagram can be achieved through control of the drawing temperature.

III.9. References

[1] D. P. Bortfeld and H. Meier, "Refractive indices and electro-optic coefficients of the eulitities $Bi_4Ge_3O_{12}$ and $Bi_4Si_3O_{12}$," *J. Appl. Phys.*, vol. 43, no. 12, pp. 5110–5111, 1972.

[2] A. K. Varshneya, *Fundamentals of Inorganic Glasses*, 1st edition. Academic Press, New York, NY, 1994.

[3] N. Gupta *et al.*, "Annealing of silicon optical fibers," *J. Appl. Phys.*, vol. 110, no. 9, 2011.

[4] N. Healy *et al.*, "CO_2 Laser-Induced Directional Recrystallization to Produce Single Crystal Silicon-Core Optical Fibers with Low Loss," *Adv. Opt. Mater.*, vol. 4, no. 7, pp. 1004–1008, 2016.

[5] D. Savytskii, B. Knorr, V. Dierolf, and H. Jain, "Demonstration of single crystal growth via solid-solid transformation of a glass," *Sci. Rep.*, vol. 6, no. March, pp. 1–7, 2016.

[6] G. Aldica and S. Polosan, "Investigations of the non-isothermal crystallization of $Bi_4Ge_3O_{12}$ (2:3) glasses," *J. Non. Cryst. Solids*, vol. 358, no. 9, pp. 1221–1227, 2012.

[7] Y. Fei, S. Fan, R. Sun, and M. Ishii, "Study on phase diagram of Bi_2O_3-SiO_2 system for Bridgman growth of $Bi_4Si_3O_{12}$ single crystal," *Prog. Cryst. Growth Charact. Mater.*, vol. 40, no. 1, pp. 183–188, 2000.

[8] Y. T. Fei, S. J. Fan, R. Y. Sun, and J. Y. Xu, "Crystallizing behaviour of Bi_2O_3-SiO_2 system," *J. Mater. Res. Lett.*, vol. 19, pp. 893–895, 2000.

[9] V. P. Zhereb and V. M. Skorikov, "Metastable states in bismuth-containing oxide systems," *Inorg. Mater.*, vol. 39, no. Suppl. 2, pp. S121–S145, 2004.

[10] A. Elsen *et al.*, "In situ X-ray studies of adlayer-induced crystal nucleation at the liquid-liquid interface.," *Proc. Natl. Acad. Sci. U. S. A.*, vol. 110, no. 17, pp. 6663–8, 2013.

[11] E. M. Levin and R. S. Roth, "Polymorphism of bismuth sesquioxide. I. Pure Bi_2O_3," *J. Res. Natl. Bur. Stand. Sect. A Phys. Chem.*, vol. 68A, no. 2, p. 189, 1964.

[12] M. Yashima, D. Ishimura, and K. Ohoyama, "Temperature dependence of lattice parameters and anisotropic thermal expansion of bismuth oxide," *J. Am. Ceram. Soc.*, vol. 88, no. 8, pp. 2332–2335, 2005.

[13] F. H. El Batal, "Gamma ray interaction with bismuth silicate glasses," *Nucl. Instruments Methods Phys. Res. Sect. B Beam Interact. with Mater. Atoms*, vol. 254, no. 2, pp. 243–253, 2007.

[14] Schott glass, "Schott DURAN® tubing brochure." [Online]. Available: http://www.us.schott.com/tubing/english/products/DURAN.html.

[15] K. Takagi, T. Oi, T. Fukazawa, M. Ishii, and S. Akiyama, “Improvement in the scintillation conversion efficiency of $Bi_4Ge_3O_{12}$ single crystals,” *J. Cryst. Growth*, vol. 52, pp. 584–587, 1981.

[16] V. Vaithianathan *et al.*, “Growth and structural study of bismuth germanate single crystal and its energy resolution,” *Mater. Chem. Phys.*, vol. 74, no. 2, pp. 121–125, 2002.

[17] V. Chani, K. Lebbou, B. Hautefeuille, O. Tillement, and J. M. Fourmigue, “Evaporation induced diameter control in fiber crystal growth by micro-pulling-down technique: $Bi_4Ge_3O_{12}$,” *Crystal Research and Technology*, vol. 41, no. 10. pp. 972–978, 2006.

[18] S. Wildermuth, K. Bohnert, H. Brändle, J. M. Fourmigue, and D. Perrodin, “Growth and characterization of single crystalline $Bi_4Ge_3O_{12}$ fibers for electrooptic high voltage sensors,” *J. Sensors*, vol. 2013, pp. 1–7, 2013.

[19] A. Durif-Varambon, “Etude de la substitution du silicium dans quelques types d’orthosilicates (Study of the substitution of silicon in some types of orthosilicates),” *Bulletin de la société française de minéralogie et de cristallographie*, vol. 82, pp. 285–314, 1959.

[20] H. Xie, F. Li, C. Chen, H. Xi, X. Wang, and X. Zhu, “Sol–gel preparation and characterization of $Bi_4(Si_{1-x}Ge_x)_3O_{12}$ solid solutions,” *J. Sol-Gel Sci. Technol.*, vol. 72, pp. 37–42, 2014.

[21] J. H. Cho, S. J. Kim, and Y. S. Yang, “Structural change in $Bi_4(Si_xGe_{1-x})_3O_{12}$ glasses during crystallization,” *Solid State Commun.*, vol. 119, no. 7, pp. 465–470, 2001.

[22] S. Inaba, H. Tokunaga, C. Hwang, and S. Fujino, “Viscosity of Bi_2O_3–B_2O_3–SiO_2 melts,” *Phys. Chem. Glas. Eur. J. Glas. Sci. Technol. B*, vol. 50, no. 3, pp. 153–155, 2009.

[23] G. Gévay, “Growth and characterization of $Bi_4Ge_3O_{12}$ single crystals,” *Prog. Cryst. Growth Charact. Mater.*, vol. 15, no. 7, pp. 145–186, 1987.

[24] V. P. Zhereb and V. M. Skorikov, “Metastable States in Bismuth-Containing Oxide Systems,” vol. 39, 2003.

[25] S. Polosan, F. Nastase, and M. Secu, “Structural changes during the crystallization of the $Bi_4Ge_3O_{12}$ glasses,” *J. Non. Cryst. Solids*, vol. 357, no. 3, pp. 1110–1113, 2011.

[26] F. Smet and W. J. P. Van Enckevort, “In situ microscopic investigations of crystal growth processes in the system Bi_2O_3-GeO_2,” *J. Cryst. Growth*, vol. 100, no. 3, pp. 417–432, 1990.

[27] H. W. Guo, X. F. Wang, and D. N. Gao, “Non-isothermal crystallization kinetics and phase transformation of Bi_2O_3-SiO_2 glass-ceramics,” *Sci. Sinter.*, vol. 43, no. 3, pp. 353–362, 2011.

[28] P. S. Halasyamani and K. R. Poeppelmeier, “Noncentrosymmetric Oxides,”

Chem. Mater., vol. 10, no. 10, pp. 2753–2769, 1998.

CHAPTER IV

HIGH BISMUTH CONTENT GLASS OPTICAL FIBERS

This chapter focuses on the fabrication of bismuth oxide-containing glass core optical fibers using the molten core method in order to study their nonlinear properties. It was observed in previous chapters that an amorphous bismuth silicon oxide phase could be obtained. As stated in the Introduction (Chapter I), this phase is of interest for all-optical signal processing applications. The molten core method is an optical fiber fabrication technique that is less evaluated, and difficulties in obtaining glass core optical canes or fibers were encountered (i.e., melting during draw). This was linked to the inherent thermodynamics of the bismuth oxide powder, and this chapter will provide an understanding of the precursor materials' processing with the molten core method using soft glass claddings.

The first section of this Chapter will describe the materials and methods used to fabricate the fibers. The second section will focus on the melting behavior of the powder and describe the different attempts and designs employed to tackle the difficulties in processing the Bi_2O_3 powder precursor. The importance of powder processing design will be underlined. Then, the third section will highlight the importance of coefficient of thermal expansion (CTE) mismatch on fiber transmission, while the fourth section will investigate the thermo-reduction behavior of the Bi_2O_3 powder. Finally, the fifth section will conclude this chapter and give an overall comprehension of the fiber draw dynamics involving the bismuth oxide precursor that were investigated in this chapter.

IV.1. Materials and Methods

IV.1.1. Sample preparation

In the following experiments, two silica-based commercial cladding glass tubes were used: borosilicate glass cladding tubes (denoted DURAN®) of dimensions 3x30 mm and 3x18mm (inner diameter x outer diameter) and composition $81SiO_2$-$13B_2O_3$-$4Na_2O$-$2Al_2O_3$ in wt%; and a soda-lime-silicate cladding glass tube (denoted AR-GLAS®) of dimensions 3x18 mm and composition $69SiO_2$-$13Na_2O$-5CaO-$4Al_2O_3$-$3K_2O$-3MgO-2BaO-$1B_2O_3$ in wt%. The DURAN® cladding glass draw range is 950-1100°C while the AR-GLAS® draw range is 850-885°C. The former requires special processing where two drawing steps are needed: the preform is drawn to a large diameter "fiber" size on the order of millimeters (called "cane") that is then redrawn to fiber size (125 µm). This two-step processing limits crystallization of the fibers at the surface that would take place if the preform was drawn directly to fiber; thus, this increases the mechanical robustness of the drawn fibers. AR-GLAS® does not necessarily require this additional processing unless desired for specific reasons. High purity commercial powders were utilized for draws requiring powder precursors (Bi_2O_3, 99.9995% purity; B_2O_3, 99.995% purity; CeO_2, 99.5% purity). The powder was introduced in the hollow core of the cladding glass tube whether as-is (inserted from atop) or as three millimeter hand-pressed pellets.

IV.1.2. Electron microscopy

A Hitachi SU-6600 Scanning Electron Microscope (SEM) with Energy-Dispersive X-ray spectroscopy (EDX) in secondary electron (SE) mode was utilized to observe the morphology and analyze the composition of the core. The SEM was operated with electron beam energy of 20 kV in a variable pressure environment of 30 Pa. The

working distance was about 10 mm. The canes were manually polished to a 2.5 µm finish or mechanically polished to a 0.05 µm finish. In all experiments, EDX is not able to detect the boron element and therefore, all compositions obtained are not true compositions but rather provide insights into changes from the original core phase to the final fiber. Herein, all compositions are mentioned in mol%.

Transmission Electron Microscopy (TEM) was used to investigate the presence of nanoparticles in the glass cores. Cane samples of interest were crushed into powder in a silica mortar while removing as much cladding as possible. The fine powder was then mixed with ethanol in an Eppendorf tube and shaken well until cloudy. Solution droplets were dropped on a mesh and dried out in air for five minutes. The mesh containing the glass particles was inserted in a Hitachi 7600 transmission electron microscope for imaging. The electron microscope was operated with an electron beam energy of 110kV.

IV.1.3. Powder X-ray diffraction

Powder x-ray diffraction was performed in order to verify the amorphous structure of the obtained canes and fibers. A Rigaku Ultima IV diffractometer was used for this purpose, using the Cu K_α radiation (λ=1.5408Å) for X-ray generation. Canes and fibers were crushed into powder using a silica mortar and pestle. The obtained powder contains both cladding and core material. The scan speed was set to 0.6-0.7 deg.min^{-1} and the 2-theta scan range was set between 5° and 70°.

IV.1.4. Fiber transmission analysis

Qualitative transmission measurements were carried out on drawn canes and fibers using an optical microscope. The canes and fibers were polished on both ends and

place under an optical microscope. White light was illuminated from the bottom of the optical microscope into the bottom of the cane or fiber and was collected at the other end of the cane/fiber. Pictures were taken using a 10x and 50x objective for canes and fibers respectively, and a camera wired from the optical microscope to a computer with a QSPAK imaging software was used to capture the images. If the core appeared bright on the image, the cane/fiber showed light transmission; if the core was found black, it absorbed and/or scattered the light and thus exhibited very high losses. The canes and fibers length used were less than five centimeters.

IV.2. Precursor powder processing design

Two precursor powder designs were employed in the drawing of bismuth oxide powder in soft glass cladding systems, namely "pressed powder pellets" and "poured powder" designs. Each design influenced the melting behavior of the Bi_2O_3 powder and the results are presented for each design.

IV.2.1. Pressed powder pellets

IV.2.1.1. Draw in borosilicate glass cladding

The first design investigated to fabricate amorphous bismuth oxide core optical fibers employed hand-pressed Bi_2O_3 powder pellets stacked in a 3x30 mm borosilicate tube. The pellet form allows one to obtain a better thermal conductivity throughout the powder by reducing the amount of air pores (that are thermally isolating) and increase physical contact amongst the powder. Hence, this design is used to improve the melting behavior of the processed powder. Additionally, an increase in the green body density is known to increase the fiber core concentration during fiber draw (in silica glass cladding) with the molten core method and hand-

pressed pellets would be favorable to obtain large Bi_2O_3 core concentration useful for nonlinearities.

The preform was drawn at 950°C to cane with a speed of 0.56 $mm.min^{-1}$. The obtained canes were ranging from 1.5 mm to 2.5 mm diameter and showed large powder-like packet segments of cores with a yellow color (Figure IV-1a), as well as homogeneous brown core phases (Figure IV-1b). The core exhibiting a brown color was analyzed with SEM (Figure IV-2a). The core was 416 µm diameter and the cane was 1.8 mm diameter. No microstructures similar to that described in the previous Chapter III were observed and the core was seen as amorphous (see Figure C-1 in Appendix C). The core composition of this brown core cane was found to be $45.1SiO_2$-$52.1Bi_2O_3$-$1.2Al_2O_3$-$1.6Na_2O$ (Figure IV-2b). While the large bismuth oxide content observed in the core is intrinsically favorable for strong nonlinearities, the large core diameter would counterbalance this attribute and decrease the nonlinear parameter γ; hence, smaller core diameters would be preferable. Not enough cane exhibiting a glassy core was available for redraw to fibers. Nonetheless, we will see in section IV.4 that the redraw to fibers of borosilicate glass cladded canes led to cores that would not transmit light due to large cracks forming in the core (as a result of the large CTE mismatch between the glass core and glass cladding).

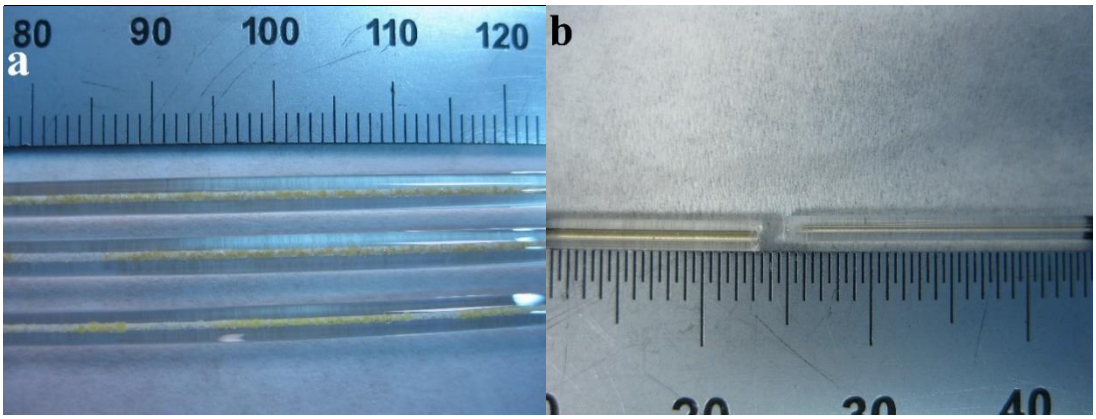

Figure IV-1. Optical image of canes drawn at 950°C from hand-pressed Bi_2O_3 powder inserted in a borosilicate glass cladding. The canes depicted (a) a powder-like core with a yellow color characteristic of non-molten Bi_2O_3 powder precursor, and (b) a homogeneous glassy phase with a brown color. Scale markers are in centimeters, cm.

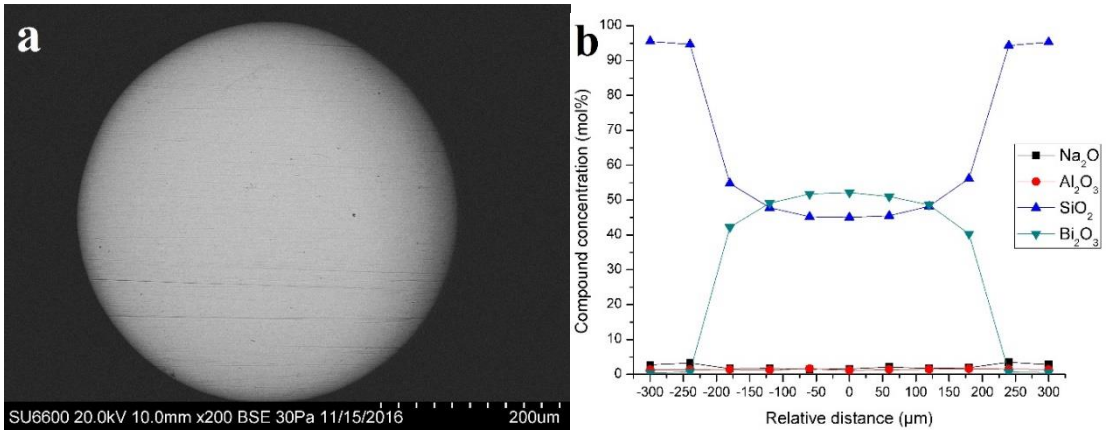

Figure IV-2. (a) SEM micrograph of a cane core cross section obtained from Bi_2O_3 pressed pellets drawn in a 3x30 mm borosilicate glass cladding tube. The bright phase corresponds to the core and the dark phase around is the glass cladding. The core exhibited a brown color with the naked eye. (b) EDX compound concentration profile across the same core. A concentration gradient was observed across the core.

Figure IV-3 depicts the SEM micrograph of the obtained powder-like yellow core cane. The core exhibited microstructures corresponding to δ-Bi_2O_3, $Bi_4Si_3O_{12}$ and Bi_2SiO_5, as discussed in Chapter III[4]. The existence of the stable high temperature crystal structure δ-Bi_2O_3 crystal polymorph indicated that the precursor powder did not fully melt. Thus, despite a drawing temperature about 130°C above the melting

[4] The difference in phases (amorphous vs crystalline) observed within a same draw likely originate from pellets exhibiting different parameters (density, shape, sizes…) that could influence their melting behavior.

point of the precursor powder, this latter did not melt entirely over the whole length of the cane. The Bi_2O_3 compound has a high enthalpy of phase transformation for its solid-solid transition at 730°C (31.547 $kJ.mol^{-1}$) and for its solid-liquid transition at 830°C (16.736 $kJ.mol^{-1}$) in addition to a high heat capacity (>110 $J.mol^{-1}.K^{-1}$) [1]–[4]. These values could suggest that the kinetics of melting involved using the bismuth oxide powder need to be accounted for (in a similar way to quartz [5]) and that, in turn, not enough energy was provided to the powder over time for melting during draw. Further investigations of drawing parameters were performed in order to melt the powder along the whole length of the cane. The effect of drawing temperature, time spent in the furnace heat zone (and combination of the twos) and preform size[5] on the melting behavior of the core were investigated. By holding the preform at 860°C above the melting point of the powder (830°C), one would allow more time and thus more energy for the powder to melt. Table IV-1 gives a summary of the conditions used for each draw and the Bi_2O_3 composition found in the amorphous core phase. Although amorphous cores were obtained in all attempts, the powder did not fully melt over the entire length of the canes and only sparse sections of the canes contained the homogeneous amorphous core. It is seen from Table IV-1 that nor the drawing temperature, holding time or preform size parameters (and their combinations) had a significant effect on the melting behavior of the powder. Longer hold times were not attempted as the hold temperature (860°C) was close to the nominal draw temperature (950°C) and could potentially deform the preform. Interestingly, the investigated parameters did not influence the core concentration

[5] The preform size was investigated as a parameter that could influence the kinetics of melting, where a smaller preform size is thought to provide a smaller path length for the heat to reach the core, which should in comparison to larger glass cladding dimensions provide more energy to the core material over time.

observed in the amorphous phase. For example, the highest Bi_2O_3 concentration was found for the draw that involved the longest holding time in the heat zone with the largest drawing temperature. This is unexpected as the sample had the most amount of time to interact with the glass cladding while it melted, and it would have been expected to obtain the lowest Bi_2O_3 concentration. It is worth noting that the observations (and conclusions made) on the influence of draw parameters only holds in this case (i.e., using the "pressed powder pellets" design) where the melting of the precursor powder was restricted, and these parameters are likely to have an effect when the whole precursor powder melts.

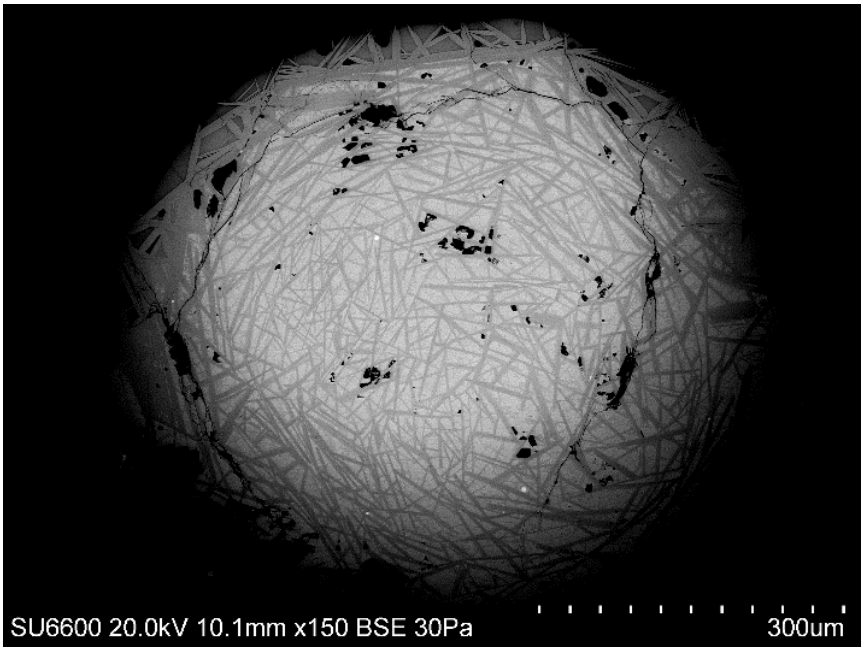

Figure IV-3. SEM micrograph of a yellow powder-like core cane cross-sections obtained from Bi_2O_3 pressed pellets drawn in a borosilicate glass cladding, showing a non-melting and reactive behavior of the core as described in Chapter III.

Table IV-1. Drawing conditions explored to melt Bi_2O_3 pressed powder pellets in borosilicate claddings. Each draw performed had a non-molten core (yellow powder-like) and some amorphous section. The Bi_2O_3 content (mol%) is given for the amorphous core (value at core center). Ø = diameter.

Preform size (mm)	T_{draw} (°C)	Holding time in heat zone[a]	ØCane (mm)	ØCore (µm)	Bi_2O_3
3x30	960	-	1.84	434	34-35
3x30	1060	2 min	2.2	375	24
3x30[b]	1060	6 min	3.15	345-355	36
3x18	950	-	2.0	365	-
3x18	960	5 min	1.35	235-245	33.8
3x18	1060	5 min	1.65	385	38.5

[a]The core of the preform containing the powder precursor was held at 860°C to potentially allow more time for the powder to melt.
[b]This draw showed a larger amount of amorphous cores over its entire length.

It is interesting to note that despite the non-melting behavior of the precursor powder, the glass cladding was incorporated in the core. The Bi_2O_3 crystal powder microstructures were embedded in a silica-rich matrix and were not fully melted nor dissolved. Glass melts are known to be corrosive and one could expect that the borosilicate glass cladding could have dissolved the precursor powder particles. However, this mechanism did not take place and the glass cladding manage to be incorporated inside the non-molten bismuth oxide pellet. This behavior with the molten core method can be explained as follow. First, it was observed that material in the core of the canes were drawn in packets. These packets corresponded to the precursor pellets that did not melt and were compressed down in the neckdown during draw. Indeed, the reduction in cladding diameter in the neckdown region implies that there are radial forces (at least) that induced the change in diameter, and these forces

were likely the reason for which the pellets were able to be compressed (see Figure C-2 in Appendix C). Second, the glass cladding was likely to be forced into the core during draw (i.e., physical mixing). The glass cladding was soft enough that it could flow in the pores of the pellet during the compression stage in the neckdown region.

IV.2.1.2. Draw in soda-lime silicate glass cladding

Further efforts to investigate the melting behavior of the Bi_2O_3 powder were carried out in a soda-lime silicate glass cladding. Although the latter is drawn at a lower temperature than the borosilicate glass cladding, this system has a larger coefficient of thermal expansion, which plays a role on the transmission properties of bismuth oxide containing fibers as described in section IV.4.2. Bi_2O_3 pressed pellets of 3 mm diameter were drawn in AR-GLAS® glass cladding at 885°C. The glass cladding was drawn directly to fiber size, i.e., 125 µm, at a speed of 10 $m.min^{-1}$. The obtained fibers were inhomogeneous and jammed the fiber coating die, and hence were not properly drawn on a spool. Figure IV-4a depicts the SEM micrograph of the core cross section obtained on an inhomogeneous fiber. The cladding was 500 µm and the core was 106-118 µm. Large randomly shaped microstructures were observed in the core, in addition to dendrite-like microstructures that were connected to these latter. Figure IV-4b illustrates the PXRD diffractogram obtained on the drawn fibers. The crystalline peaks were observed to match with the metastable γ-Bi_2O_3 phase (which can crystallize from the δ-Bi_2O_3 phase if heated above 775°C according to [6]) and indicated that the Bi_2O_3 pellets did not melt (not entirely at least), similarly to the draw in the borosilicate glass cladding. Thus, the soda-lime silicate glass cladding did not improve the melting behavior of the Bi_2O_3 precursor powder pellets. It is interesting to note that no crystals were formed in this fiber draw compared to the

previous one in Chapter III section III.7 that showed the formation of Bi_2SiO_5 needles using the same glass cladding. The difference in core crystal formation between these two draws may be explained by the difference in quenching rates. Here, the fibers were drawn at higher speeds (20 times faster) and hence with a higher quenching rate that could have prevented crystal formation.

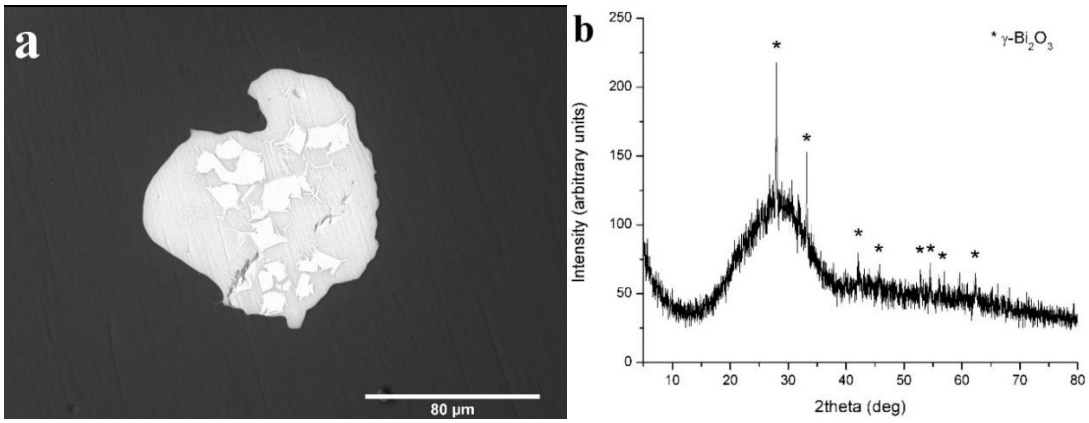

Figure IV-4. (a) SEM micrograph of a fiber core cross-section obtained from Bi_2O_3 powder pellets drawn in a soda-lime silicate glass cladding. The bright phase is the core and the dark phase around is the glass cladding. The core is highly deformed with blob-like microstructures. (b) PXRD diffractogram performed on the same fibers. The metastable phase γ-Bi_2O_3 was observed (JCPDS card #01-074-1375).

Further investigation of the Bi_2O_3 pressed pellets non-melting behavior was carried out in the soda-lime silicate glass cladding, yet using boron oxide (B_2O_3) powder as a melting accelerant (T_m = 450°C). It was mixed with Bi_2O_3 in $10B_2O_3$-$90Bi_2O_3$ mol% proportions, which is a composition in the B_2O_3-Bi_2O_3 phase diagram that lowers the liquidus temperature to ~725°C [7]. Hand pressed pellets of 3 mm diameter were loaded in the soda lime silicate glass cladding and drawn at 885°C at a speed of 10 $m.min^{-1}$. This draw did not experience any lumps and 200 m of fibers were drawn. Figure IV-5a depicts the SEM micrograph of a fiber cross section. The fiber diameter was 127 µm and the core diameter was 27 µm. The core was oblong and possessed a concentration of $46.9SiO_2$-$36.9Bi_2O_3$-$5.5Na_2O$-$5.0Al_2O_3$-$2.6CaO$-$1.9MgO$-$0.6K_2O$-

0.5BaO at its center (Figure IV-5b). It is worth mentioning that the large amount of Bi_2O_3 retained in the fiber (~37 mol%) is an upper value since B_2O_3 cannot be detected and this latter was present in the initial powder in a noticeable amount. Nonetheless, the Bi_2O_3 content was likely to be >25 mol% in the fiber and would thus generate high nonlinearities (relative to silica). No microstructures were observed in the core and the fibers were shown to be amorphous (see Figure C-3 in Appendix C). While one can think that the B_2O_3 powder was effective as a melting accelerant compound, it was noticed after the fiber draw that the top of the preform displayed condensation on the walls of the glass tube. Boron oxide is known to be hygroscopic and further examination of the boron oxide precursor powder was performed using Thermal Gravimetric Analysis (TGA) and Fourier Transform Infrared Spectroscopy (FTIR) (see Figure C-4 and Figure C-5 in Appendix C). It was revealed that the precursor powder was contaminated with water, H_2O, which explains its condensation on the top of the preform as it evaporated upon drawing. Hence, the true effect of the boron oxide on the melting behavior of bismuth oxide could not be asserted since water is also a melting accelerant and a good fluidifying compound. Thus, the boron oxide powder was dried and the same draw was performed. Lumps were observed and their presence refuted the ability of B_2O_3 to work as a melting accelerant. Different compositions in the B_2O_3-Bi_2O_3 phase diagram and different draw parameters were also used in an attempt to melt Bi_2O_3, but were all unsuccessful (see "Investigation of compositional effect on the melting behavior of Bi_2O_3 during fiber draw in a soda lime silicate glass cladding using the pressed pellet design" in Appendix C).

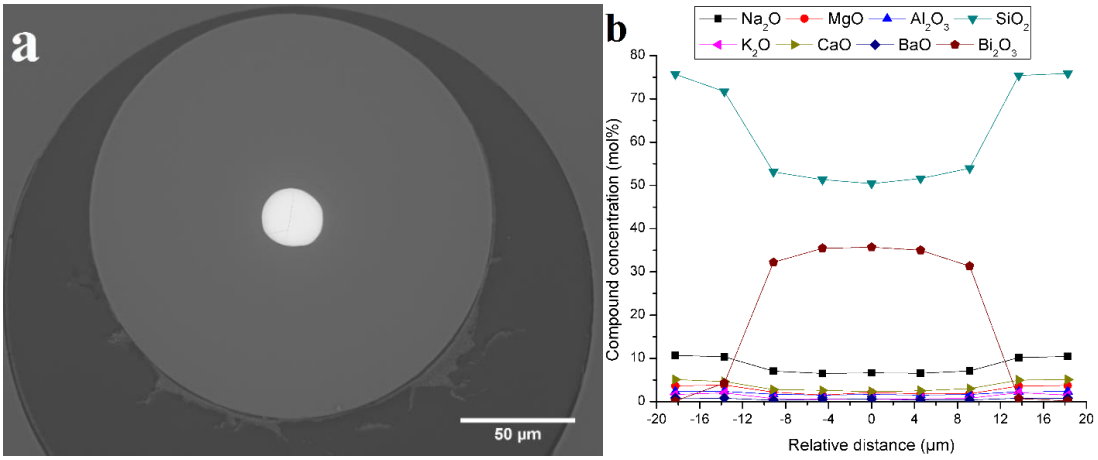

Figure IV-5. (a) SEM micrographs of a fiber cross-section derived obtained from $90Bi_2O_3$-$10B_2O_3$ (mol%) pressed pellets drawn in a soda-lime silicate glass cladding. The fiber core was shown to be homogeneous (i.e., without microstructures). The boron oxide precursor powder contained water, which helped in melting the bismuth oxide precursor powder. (b) EDX compound concentration profile across the core of the same fiber.

IV.2.2. Poured powder

The second design investigated did not make use of powder pellets and the powder was simply inserted atop the borosilicate or soda-lime silicate glass cladding preform. Bi_2O_3 was inserted in a 3x30 mm borosilicate glass cladding and drawn at 1060°C to cane. The pictures in Figure IV-6 illustrate the first parts of the obtained canes and showed that a homogeneous amorphous phase was obtained (as well as air gaps). A yellow homogeneous core was first appearing then followed by a brown homogeneous core. The following canes demonstrated a continuous homogeneous core over a meter length with a slight brownish color. The SEM analysis and EDX compound concentration profiles on these canes were provided in Chapter III section III.4 and showed a homogeneous core with no microstructures, as well as a large Bi_2O_3 content (~40-50mol%). The powder-like core observed with the pressed pellets design was not seen in this case, and all cores were shown to be homogeneous. Thus,

the “poured powder” design offered the ability for the Bi_2O_3 powder to melt entirely during the draw.

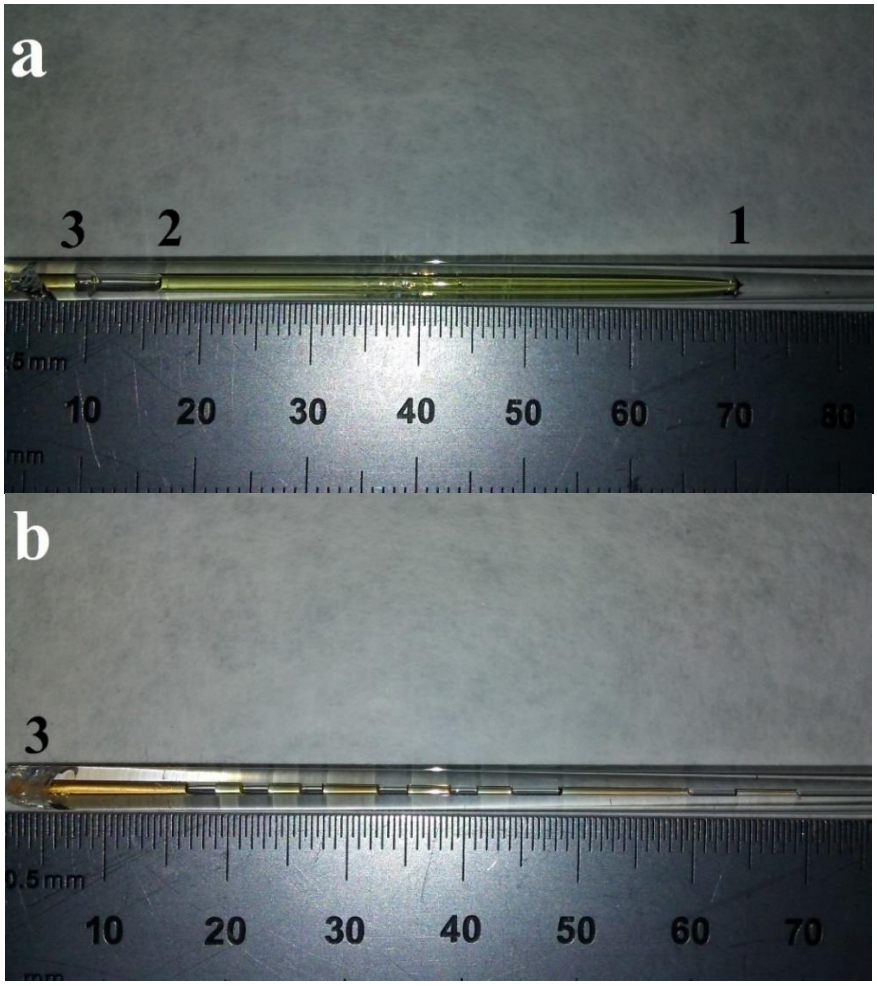

Figure IV-6. Pictures of canes drawn at 1060°C and obtained from a 3x30 mm borosilicate glass cladding with Bi_2O_3 powder inserted atop. (a) First part of the cane to be drawn showing a large yellow core, then followed by (b) a brown core. Position 1 corresponds to the beginning of the draw.

The “poured powder” design was also verified in the soda-lime silicate cladding system. Bi_2O_3 was inserted in a 3x15 mm soda-lime silicate glass cladding and drawn at 885°C to fiber. The fiber could be spooled and did not exhibit lump formation upon drawing. Figure IV-7 illustrates the SEM micrographs obtained across the fiber core cross section from the beginning (Figure IV-7a) and end (Figure IV-7c) of the draw (i.e., after ~200 m). The beginning of the draw showed a more oblong core compared

to the end of draw. The core composition were found to be 57.5SiO_2-27.6Bi_2O_3-7.3Na_2O-1.5Al_2O_3-3.2CaO-1.7MgO-0.7K_2O-0.4BaO at core center (Figure IV-7b) and 63.2SiO_2-17.4Bi_2O_3-9.0Na_2O-2.6Al_2O_3-3.8CaO-2.6MgO-0.9K_2O-0.5BaO (Figure IV-7d). These fibers exhibited a large Bi_2O_3 content of interest for nonlinearities. Despite a lower drawing temperature (compared to that of the borosilicate glass cladding system), the bismuth oxide powder melted entirely and the "poured powder" design was an effective design towards the improvement of the melting behavior of the precursor powder. The reason behind the melting and non-melting behavior observed with the "poured powder" and "pressed powder pellets" designs respectively is discussed next.

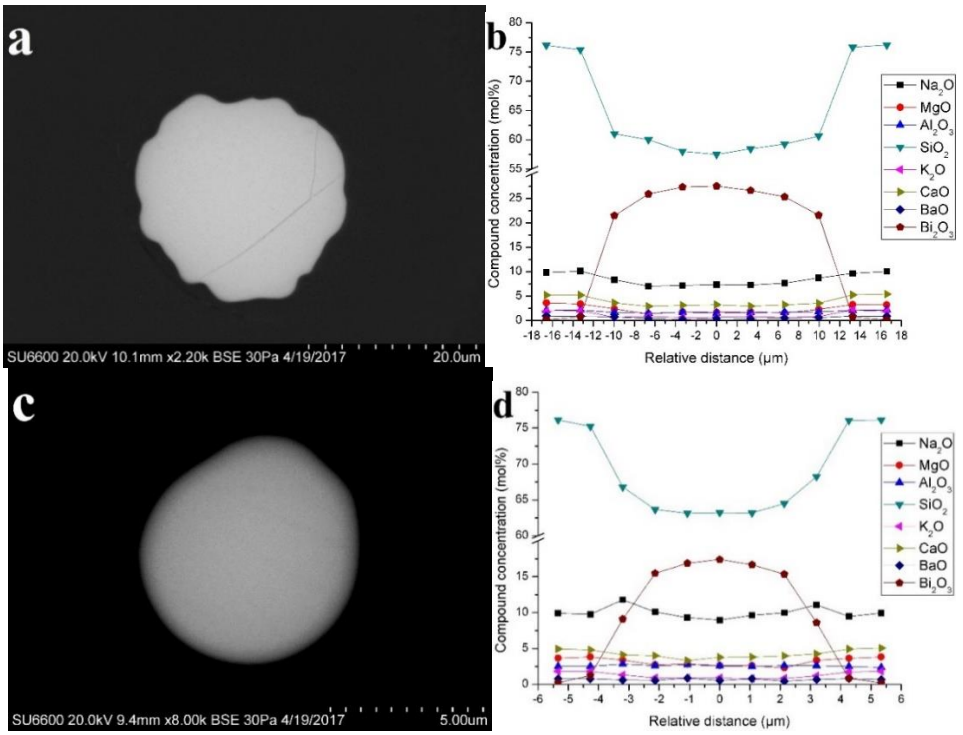

Figure IV-7. (a) SEM micrograph of a fiber core cross section obtained from the "poured powder" design of Bi_2O_3 in soda lime silicate glass cladding. The fiber was taken from the beginning of the draw and was 160 µm in diameter with a 27 µm diameter core. (b) EDX compound concentration profile across the fiber core shown in (a). (c) SEM micrograph of a fiber core cross section obtained from the end of the draw. The fiber was 133 µm diameter with a 7 µm core. (d) EDX compound concentration profile across the fiber core shown in (d).

IV.2.3. Discussion on the origin of the powder non-melting behavior

The non-melting behavior observed in previous section IV.2.1 and its origin are discussed here. Two reasons are envisaged for the non-melting behavior of the bismuth oxide powder. This could indicate whether an increase in kinetics of melting (i.e., not enough energy was provided to fully melt the precursor powder over time) or an actual increase in the melting temperature. In the latter case, an increase in melting temperature could be explained by an increase in pressure. According to Clausius-Clapeyron, an increase in pressure generates an increase of the melting temperature of a compound. Thus, the non-melting behavior of the bismuth oxide powder could be associated with an increase in its melting temperature due to an increase in pressure. Schröder and Bagdassarov [8] reported a significant increase in the bismuth oxide solid-solid ($\alpha \rightarrow \delta$) phase transition temperature (by 32°K-63°K) as a function of pressure (0.5 GPa-2.5 GPa). Additionally, they reported that bismuth oxide crystal under a pressure of 2.5 GPa did not melt when heated at 912°C, which is well above the melting temperature of 825°C at atmospheric pressure. Hence, their experiment clearly showed the effect of pressure on the phase transitions (and hence melting behavior) within the bismuth oxide compound. In our case, the increase in pressure could originate from the following argument. The Bi_2O_3 crystal powder is known to have a large coefficient of thermal expansion (CTE) of ~140×10^{-7} K^{-1} (on average [9]) while that of the borosilicate glass cladding is 33×10^{-7} K^{-1} [10]. Additionally, the Bi_2O_3 crystal powder has a large volume expansion of ~7% upon its solid-solid phase transformation [6], and a volume expansion upon melting (unknown value). Thus, as the Bi_2O_3 powder is heated up, it expands with a larger amplitude than the glass cladding. The vibrational modes of the Bi_2O_3 molecules would likely be more

confined by their surroundings (i.e., the Bi_2O_3 molecules are confined by the neighboring Bi_2O_3 powder particles and the glass cladding). This, in turn, implies that the surroundings apply pressure on the Bi_2O_3 powder particles. This applied pressure originating from the neighboring particles and surrounding glass cladding may prevent the full vibration of the molecules and thus the full volume expansion necessary for the phase transformations (solid-solid and solid-liquid) to take place, thus increasing the melting temperature of the powder. This pressure increase could thus be thought to originate from a volume expansion problem. While a pressure increase is likely to take place, the pressure magnitude increase is unknown and it is unlikely that it was as large as that mentioned by Schröder and Bagdassarov [8] (i.e., on the order of GPa) as this would likely break the glass cladding. Hence, it is believed that the kinetics of melting is the most predominant factor that contributes to the non-melting behavior. A Differential Scanning Calorimetry (DSC) experiment between low-density (i.e., loose powder) and high-density (i.e., pressed powder pellet) powders was carried out at atmospheric pressure in an attempt to probe the kinetics of melting (see "DSC experiment between loose Bi_2O_3 powder and pressed Bi_2O_3 powder pellet" in Appendix C). This experiment demonstrated that an additional energy input seems to be necessary to melt the bismuth oxide powder in the case of the high-density powder (i.e., "pressed powder pellet" design) compared to the low-density powder (i.e., the "poured powder" design). This, perhaps, showed that there could be an increase of the kinetics of melting in the case of the "pressed powder pellet" design. Note that in the case of the DSC experiment, the increase in the kinetics of melting would be demonstrated to originate from the sole effect of the surrounding particles (i.e., due to an increase in density). The DSC experiments were

performed without the glass cladding around the powder, and it is expected that the glass cladding would act as an additional barrier to the volume expansion of the Bi_2O_3 powder, which would thus generate an additional increase in the kinetics of melting.[6]

Thus, it is believed that the "poured powder" design, which possesses the lowest packing density, reduced the kinetics of melting and did not suffer from the volume expansion problem due to the larger free volume surrounding the Bi_2O_3 particles into which they could freely expand. The large unusual core size discussion mentioned in Chapter III section III.4 would support the thought that the non-melting behavior originated from a volume expansion problem. In the case where the powder melted (i.e., using the "poured powder" design), the core-clad ratio largely increased (by more than three-fold compared to the original preform core-clad ratio) and justified that a very large volume expansion was experienced by the precursor powder upon the phase transformations. In the draw cases where the volume expansion was restricted, the phase transformations could thus not take place within the allowed time.

It is worth mentioning that during fiber draw the thermodynamic or kinetic path that the core will undertake was closely related to the ability of the core to retain crystals. It was shown in the two previous sections that crystalline phase or amorphous phases can be obtained by tuning the precursor material density form ("pressed powder pellets" vs "poured powder"). Thus, the powder processing design is a parameter that one can tune in order to modify the outcome phase of the core (amorphous or crystalline). Note that this is only demonstrated for canes/fibers drawn

[6] An experiment involving 1 mm pellet instead of 3 mm pellet was attempted in order to verify this hypothesis but pellet could not be stacked properly (see "Experiment investigating the cladding effect on the non-melting behavior of Bi_2O_3 pressed powder pellets" in Appendix C).

in soft glasses (i.e., multicomponent silica-based glass system drawn at relatively low temperatures) and was not shown for oxide compounds drawn in silica at high temperatures.

IV.3. Core-clad CTE mismatch consideration

The CTE mismatch between core and cladding is an issue encountered in the field of optical fibers using the standard methods of optical fiber making, whereby preform cracking can ensue if a large amount of dopants is incorporated in the core (or cladding) preform . Moreover, the CTE mismatch between the core and the cladding inherent to the doping process leads to internal stresses in the core upon quenching, which could potentially crack the same core and break the fiber upon drawing if the crack reaches the fibers' surface. The molten core method is perhaps unique in its genre as the drawn fibers exhibit a large amount of dopants in the core and hence the drawn fibers possess a large CTE difference. Nonetheless, this large CTE difference between core and cladding does not affect the drawing behavior of the fibers (to some dopant concentration extent), and fibers can be drawn without breaking. For example, fibers containing a large amount of BaO were drawn without breaking upon drawing, and the resultant CTE of the core center was estimated to be ~10.9 times higher than the surrounding silica cladding (using fiber composition at core center from [11] and deduced CTE values of core composition from model in [12]). Additionally, core cracking upon cleaving (due to the possible release of internal stresses [13]) was not observed and did not impinge light transmission testing to be performed on these BaO fibers [11].

In our case, bismuth-containing optical canes and fibers were drawn in two different glass cladding systems (borosilicate, BS, and soda-lime silicate, SLS) and the effect of CTE mismatch was investigated in both systems. The drawn canes and fibers parameters are summarized in Table IV-2. The CTE of the core was roughly estimated using the same model from [12]. Figure IV-8 illustrates the linear coefficient of thermal expansion as a function of the Bi_2O_3 content in the glass for the bismuth silicate SiO_2-Bi_2O_3 binary system, as well as for the BS-Bi_2O_3 and SLS-Bi_2O_3 systems. The model in [12] only applies for binary systems and in order to evaluate the CTE of the compositions obtained in the canes and fibers, the borosilicate and soda-lime silicate system were each taken as behaving as one glass component, from which Bi_2O_3 could then be added. In view of this consideration, it was hence assumed that each oxide compound of the glass cladding was introduced in the core in the same percentage, i.e., the composition ratios of the oxide compounds "i" in the end cane or fiber relative to that of the same oxide compounds "i" in the glass cladding were kept the same. The composition ratios for each oxide compound "i" ($x_{i\ core}/x_{i\ cladding}$) were calculated using the compositions of the core center and the composition of the pure glass cladding obtained from EDX. The obtained values are presented in Table IV-3 and it is observed that this latter assumption was roughly acceptable in the borosilicate glass cladding where, for example, 46% ±3% of each oxide compound from the pure borosilicate glass cladding was incorporated in the cane core of sample BS-1. The assumption seems to be less correlated with the soda-lime silicate glass cladding where larger standard deviations (15-30%) were obtained.

The CTE of each core composition was then estimated from Figure IV-8. In the case of canes and fibers drawn with the borosilicate glass cladding, B_2O_3 was also

incorporated in the core and was not detected with EDX. Hence, it needed to be accounted for as its addition would likely reduce the actual value of Bi_2O_3 detected and used to estimate the CTE. The amount of B_2O_3 was estimated using the average glass cladding oxide compound incorporation calculated in Table IV-3 and multiplying it by the initial B_2O_3 amount in the borosilicate glass cladding (11.5 mol%). Then, the obtained B_2O_3 content was substracted from the Bi_2O_3 content of the composition in Table IV-2 so that a lower limit of CTE can be deduced (this assumes that B_2O_3 would only offset the value of Bi_2O_3 if it was detected with EDX). The CTE of the core canes and fibers drawn in the borosilicate glass cladding were calculated to be ~2.8 and ~1.5-1.7 times higher than the corresponding glass cladding respectively, while the CTE of the fibers drawn in the soda-lime silicate glass cladding was calculated to be ~1.1 times higher than the corresponding glass cladding. In the case of canes and fibers drawn in the borosilicate glass cladding, the CTE differences between core and cladding were much lower than than in the case of the BaO fibers mentioned perviously and yet, qualitatitve light transmission testing revealed very high losses as will be explained in the next section IV.4.

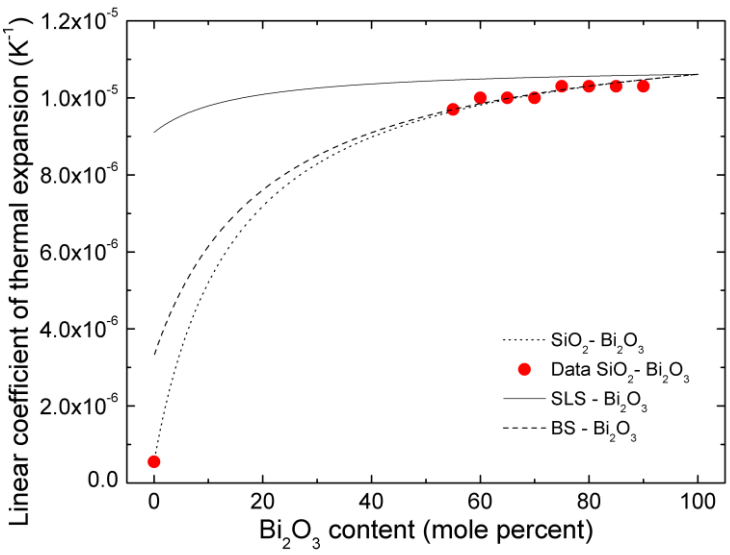

Figure IV-8. Linear coefficient of thermal expansion (CTE) as a function of Bi_2O_3. The curves were obtained using Eq. (6) from [12]**. The SiO_2-Bi_2O_3 binary system was modeled using CTE data from** [14] **and, the BS-Bi_2O_3 and SLS-Bi_2O_3 curves used data from the brochures** [10], [15]**. BS = Borosilicate, SLS = Soda-lime silicate.**

Table IV-2. Properties of drawn cane and fibers (dimensions, composition at core center and the estimated CTE of the composition at core center). The CTE was estimated using the model in [12]. In the case of the compositions in the borosilicate glass system, the estimated B_2O_3 amount was calculated in Table IV-3 and substituted for Bi_2O_3. Note that the estimated CTE in this case is a lower limit value. BS = Borosilicate, SLS = Soda lime silicate. The compound concentrations are expressed in mol%.

Cladding system	Precursor composition (mol%)	T_{draw} (°C)	Cladding diameter (mm)	Core diameter (µm)	SiO_2	Bi_2O_3	Al_2O_3	Na_2O	CaO	BaO	MgO	K_2O	CTE ($x10^{-7}$ K^{-1})
BS-1	Bi_2O_3	1060	3.5	560	46.7	50.2	1.2	2.0	-	-	-	-	93.1
BS-2	Bi_2O_3	960	1.8	420	45.1	52.1	1.2	1.6	-	-	-	-	94.0
BS-3	$99.5Bi_2O_3$-$0.5CeO_2$	1060	3.2	350	60.3	36.0	1.6	2.1	-	-	-	-	90.3
BS-4	$99.5Bi_2O_3$-$0.5CeO_2$	1035	0.136	23	80.0	14.9	1.9	3.2	-	-	-	-	56.3
BS-5	$99.5Bi_2O_3$-$0.5CeO_2$	1035	0.122	17.5	80.5	14.0	2.3	3.2	-	-	-	-	47.7
SLS-1[a]	$90Bi_2O_3$-$10B_2O_3$	885	0.125	26.5	50.4	35.7	1.6	6.6	2.4	0.6	2.1	0.6	>102.7
SLS-2	Bi_2O_3	885	0.160	25	57.5	27.6	1.5	7.3	3.2	0.4	1.7	0.7	102.2
SLS-3	Bi_2O_3	885	0.133	7	63.2	17.4	2.6	9.0	3.8	0.5	2.6	0.9	100.3

[a] The CTE calculated for this fiber composition does not include B_2O_3 in the original precursor composition, which has higher CTE than Bi_2O_3. Hence, the CTE value provided here is a lower limit.

Table IV-3. Calculated percentage of oxide compound incorporated from the initial glass cladding composition into the core center for each composition of Table IV-2. An average of glass cladding oxide compound incorporation was calculated for each composition. This latter value can then be used to determine roughly the amount of B_2O_3 found in the core by multiplying it with the initial amount of B_2O_3 known from the glass cladding manufacturer (i.e., 11.5 mol% [10]). Note that in the case of fiber compositions obtained in the soda lime silicate glass system, the large standard deviation values obtained do not indicate that each compound was incorporated in a similar percentage from the glass cladding into the core. Legend: BS = Borosilicate, SLS = Soda lime silicate.

Cladding system	SiO_2 ratio (%)	Al_2O_3 ratio (%)	Na_2O ratio (%)	CaO ratio (%)	BaO ratio (%)	MgO ratio (%)	K_2O ratio (%)	Average compound incorporation (%)	Standard deviation (%)	Estimated B_2O_3 at core center (mol%)
BS-1	50	44	43	-	-	-	-	46	3	5-5.6
BS-2	49	34	44	-	-	-	-	41	6	4-5.4
BS-3	65	59	45	-	-	-	-	55	9	5.3-7.4
BS-4	86	70	68	-	-	-	-	77	8	7.7-9.8
SLS-2	81	63	57	44	75	46	35	62	17	-
SLS-3	89	108	70	69	63	57	45	80	33	-

IV.4. Light transmission testing

Light transmission is a central requirement in optical fibers and fibers exhibiting high losses (>1 $dB.m^{-1}$) can be considered unpractical. This section provides here a qualitative understanding of the drawn canes and fibers. Simple light transmission experiments (i.e., using an optical microscope) were carried out on canes and fibers exhibiting an amorphous core to study their light transmission behavior. Canes and fibers were drawn in borosilicate and soda-lime silicate glass cladding, and both claddings were shown to have an impact on the light transmission behavior of the cores. The results are presented in this section along with an understanding of the observed differences brought by the two glass cladding systems used.

IV.4.1. Bismuth-containing fibers drawn in borosilicate glass cladding

Figure IV-9a provides an image of an as-drawn cane (cane #1) and a cleaved cane (cane #2) drawn in a borosilicate glass cladding using the "pressed powder pellet" design. The core of the as-drawn cane was shown to be homogeneous (with a light brown color), while the cleaved cane no longer exhibited a homogeneous core and was highly shattered. The shattering behavior of cane#2 upon cleaving observed in Figure IV-9a could be related to the seemingly similar principle as in the "Prince Rupert's drop experiment". The higher CTE of the core compared to that of the glass cladding brought the core in tension while the glass cladding was brought in compression. The high tensile stresses built up in the cane core were relieved upon cleaving [13] and multiple crack bifurcation events took place in the core and shattered it. Figure IV-9b and Figure IV-9c depicts an optical micrograph

transmission picture of cane#1[7] and cane#2 respectively. The red-orange core observed in Figure IV-9b indicated that light was transmitted through the core (the observed color was due to the brown color of the core); and the black core observed in Figure IV-9c indicated that the core fully scattered the light. It was no surprise to find out that the shattered core in cane#2 did not transmit light. The cracks generated in the core highly scattered the light and no light transmission could be demonstrated. Interestingly, high losses were also observed for a cane showing a homogeneous core (i.e., non-shattered core). This was likely due to the presence of bismuth nanoparticles in the core that absorbed and/or scattered the light as will be described in details in section IV.5. In the case of cane#1, it is worth noting that the intensity difference between the bright surrounding glass cladding and the orange core indicated that the latter was absorbing a large amount of light and thus exhibited high losses.

Fibers were drawn from borosilicate glass-cladded canes and the light transmission behavior of the fibers was explored in a similar way to that of the canes. Figure IV-10a shows a representative optical transmission picture of a bismuth-containing fiber drawn in borosilicate glass cladding. The core was shown to be black and thus the core exhibited high losses. The formation of cracks in the fiber core upon cleaving was further investigated. Multiple cracks were formed in the core as seen in Figure IV-11 and the cracks were seen to be formed centimeters away from the cleaved end. Thus, the loss mechanism observed in these fibers was confirmed to be light scattering from cracks induced upon cleaving.

[7] The core of the cane#1 was kept intact upon cleaving by cutting the cane on the outside of the cracks observed in Figure IV-9a, and polishing carefully through the cracks.

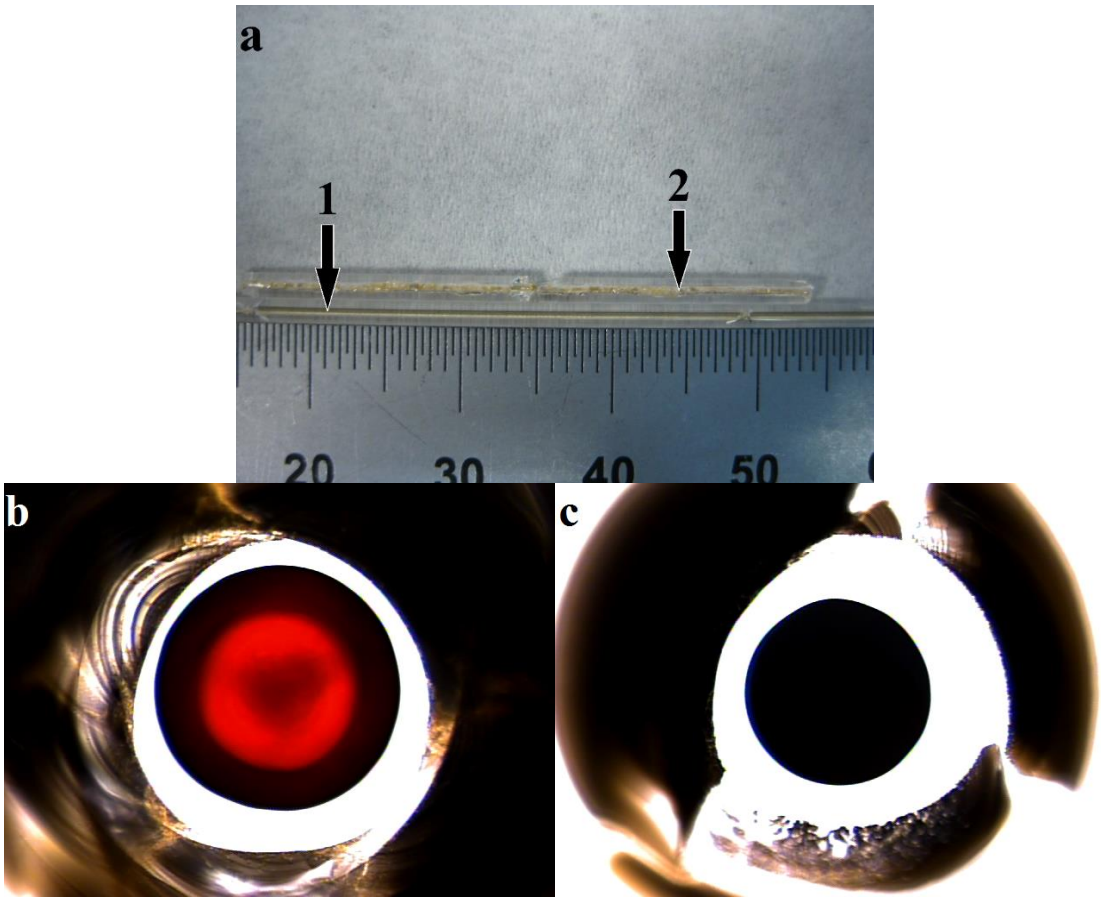

Figure IV-9. (a) Side view optical micrograph of a bismuth-containing borosilicate cane. Cane #1 was an as-drawn cane, and cane #2 was obtained after cleaving the cane. Note the small cracks in cane#1. Light transmission testing picture showing (b) light transmitted through the core (in orange) and (c) light totally absorbed by the core. The glass cladding is the bright white circle around the orange or black core.

The annealing effect on the relaxation of the draw-induced stresses was investigated. For this purpose, fibers were annealed at 500°C in order to relieve the built-in stresses and avoid cracking/shattering upon cleaving[8]. While the fibers used for annealing were already cracked on both ends, centimeter-long portions in the fiber center were not cracked and the effect of annealing was observed by cleaving the fibers in their center region. Long pieces of bare fibers (~15 cm) were annealed in order to retain a long length of non-cracked fiber core. Figure IV-10b shows a

[8] Fibers herein contained up to 15 mol% Bi_2O_3 and the annealing temperature was chosen to be above the T_g of a $30Bi_2O_3$-$60SiO_2$-$10B_2O_3$ that is at 374°C [25].

representative optical micrograph transmission picture of an annealed fiber. The fiber core was found to be illuminated indicating that light was transmitted through the fibers. Hence, the annealing process effectively reduced the draw-induced stresses in the glass fiber and precluded crack propagation upon cleaving[9]. Note that the core-clad interface exhibits a crack in Figure IV-10b but did not seem to prevent light transmission. The improvement of the fiber transmission properties upon annealing showed that, if one desired to use borosilicate glass cladding, an in-line thermal annealing furnace or thermal laser annealing would be of interest to reduce the draw-induced stresses.

It is interesting to note that the core-clad CTE difference of the bismuth-containing fibers drawn in borosilicate glass cladding here was much lower than that of the BaO-derived fibers (by eight times), as seen in previous section IV.3. Based on a CTE argument and the fact that attenuation measurements were made possible on the BaO-derived core fibers [11], one could have expected to observe light transmission in the the as-drawn bismuth-containing fibers. Nonetheless, this was not the case, and the CTE argument in itself is not sufficient to predict the crack behavior (and light transmission capability), and the magnitude of tensile stresses would be more informative instead.

[9] The center regions of the as-drawn fiber pieces were observed to crack when they were not annealed.

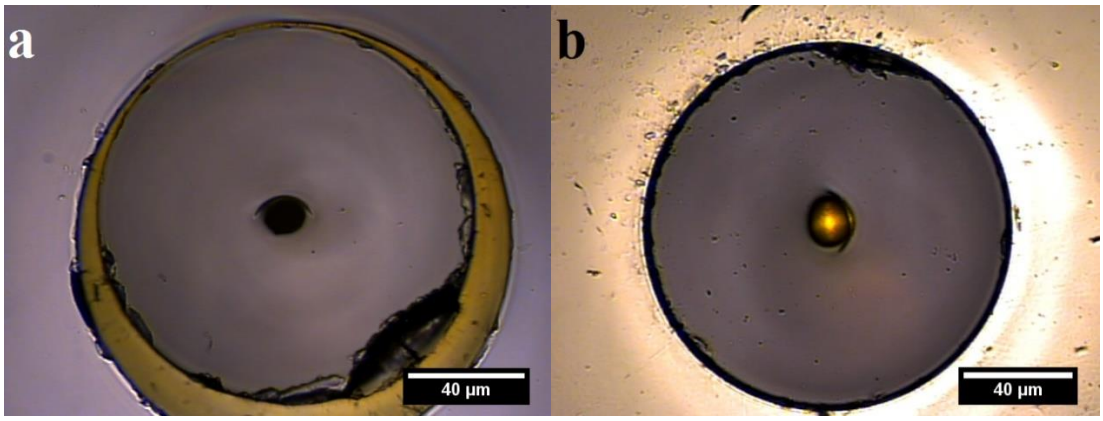

Figure IV-10. Representative optical micrograph of bismuth-containing borosilicate fibers cross section with light illuminated from their bottom. (a) as-drawn fiber and, (b) annealed fiber at 500°C for 4h in air. The as-drawn fiber showed a black core indicating no light transmission, and the annealed fiber showed an orange core indicating that light was transmitted through the core.

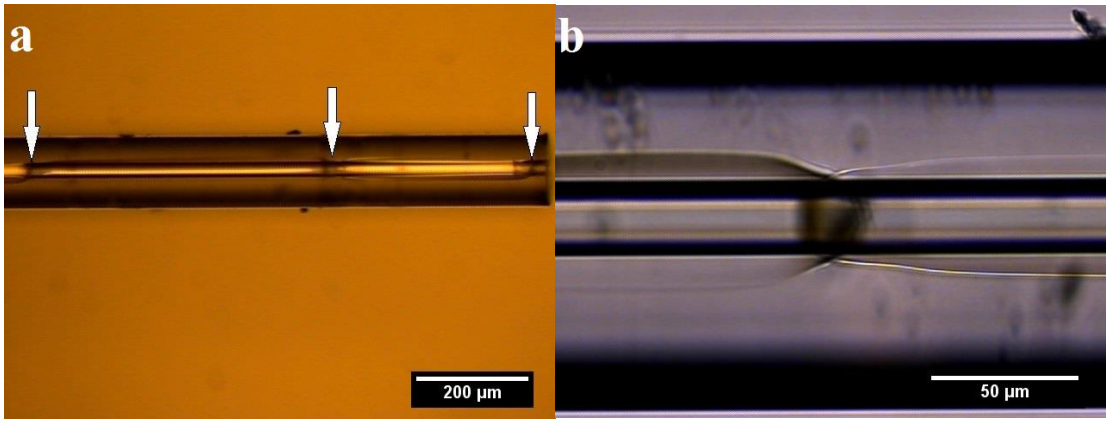

Figure IV-11. (a) Side view optical micrograph of a borosilicate glass-cladded bismuth oxide core optical fibers after cleaving. Multiple crack center points were observed in the core (indicated by arrows) and were propagated along centimeter lengths from the cleaved end. (b) Side view optical micrograph of same fiber magnified on a crack center point. The crack is seen to be localized in the core and propagates along the core-clad interface towards another crack center point.

IV.4.2. Bismuth-containing fibers drawn in soda-lime silicate glass cladding

Figure IV-12 depicts optical micrograph transmission pictures representative of an as-drawn fiber drawn in a soda lime silicate glass cladding. Fibers in Figure IV-12a and Figure IV-12b contain a large amount of Bi_2O_3 (27.6 mol% and 17.4 mol%). The fiber core was seen to be illuminated at its center in both cases, indicating that the

light was transmitted. Note the tight confinement of the light due to the large refractive index difference between core and cladding. Crack formation was observed at the core-clad interface in Figure IV-12a but did not seem to have impacted the light transmission behavior and thus, no cracks must have formed in the core. The formation of cracks in the core was investigated (Figure IV-12c), and no cracks were observed. The observed light transmission behavior of the bismuth-containing fibers drawn in a soda-lime silicate glass cladding thus demonstrated that a decrease in the CTE mismatch difference between the glass core and glass cladding was beneficial towards the diminution of draw-induced stresses, which in turn prevented crack formation in the core.

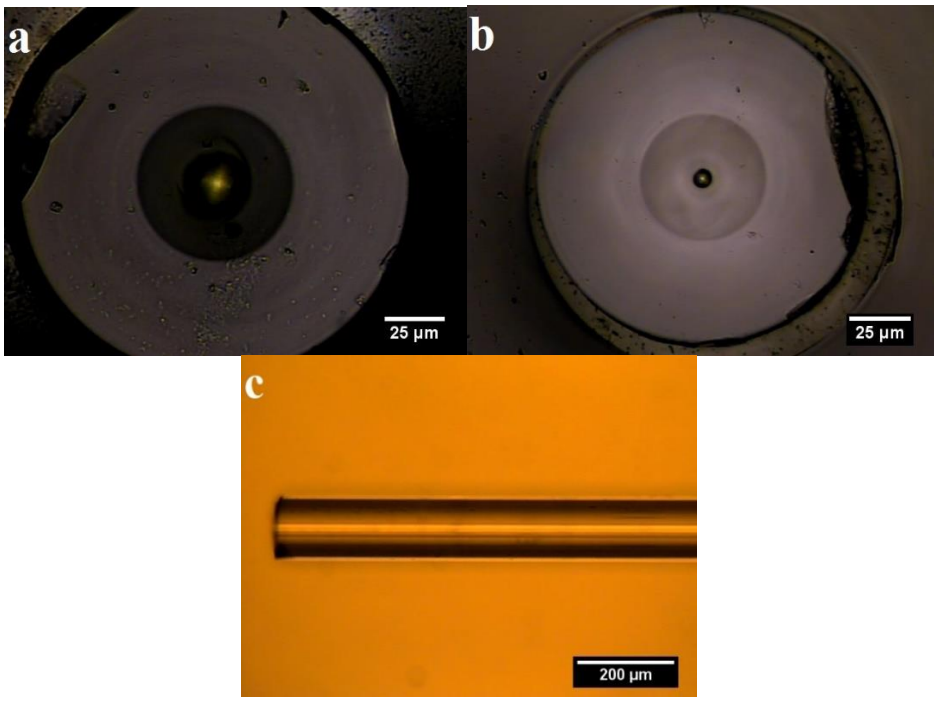

Figure IV-12. Representative optical micrographs of bismuth-containing soda-lime silicate fibers cross section with light illuminated from its bottom. (a) High Bi_2O_3 core content Bi_2O_3 (27.6 mol%) optical fiber and, (b) Lower Bi_2O_3 core content (17.4 mol%) optical fiber. Light is seen through the core of the fibers indicating that cracks were not present in the core to scatter the propagating light. (c) Side view optical micrograph of a soda-lime silicate glass-cladded bismuth oxide core optical fibers after cleaving. No cracks were observed in the core that could have resulted from the relaxation of draw-induced stresses.

IV.5. Reduction behavior of bismuth oxide containing glass optical fibers

Glasses containing bismuth oxide have been shown to display different degrees of coloration (yellow, orange, red, brown and black), which vary depending on glass composition and melting conditions [16]–[20]. For example, an increase in batch melting temperature was reported to impact the glass transmission properties as it can blacken the glass [16], [17]. These changes in color (viz. "darkening effect") were associated to the reduction of trivalent bismuth ions (Bi^{3+}) to elemental bismuth metal (Bi^0), which then aggregate to form bismuth metal colloids Bi_n (dark color) according to the following reactions [16], [17]:

$$Bi_2O_{3\,(s)} \rightarrow 2Bi_{(s)} + \tfrac{3}{2}O_{2\,(g)} \quad (4.1)$$

$$nBi_{(s)} \rightarrow Bi_n\ (colloids) \quad (4.2)$$

This thermal dissociation phenomena present in bismuth-containing glasses degrades the transmission properties of the glass and is unwanted for optical applications in the visible and NIR spectrum regions. Hence, there is a need to control the thermo-reduction behavior of bismuth oxide during fiber draw using the molten core method. In order to avoid thermo-reduction and oxidize the glass, two ways can be envisioned: use oxidizing agents in the precursor composition, or increase the oxygen partial pressure above the melt during draw (i.e., draw under oxygen atmosphere). Strong oxidizing agents such as arsenic oxide (As_2O_5), antimony oxide (Sb_2O_5) and cerium oxide (CeO_2) have been shown to be efficient to improve the transmission properties of the glass [16], [17], [21]. As_2O_5 and Sb_2O_5 are toxic compounds and, therefore, were not dealt with here. The role of CeO_2 as an oxidizing agent was thus investigated, and this was performed using both precursor powder design.

Bismuth oxide precursor powder (without oxidizing agents) was first drawn in the borosilicate glass cladding at 1060°C using the "pressed powder pellet" design and showed a light brown color glassy phase, as observed in Figure IV-9a in section IV.4.1. As discussed previously, this light brown color originates from the thermal dissociation of the trivalent bismuth ions. TEM experiment was performed in order to investigate the possible presence of bismuth nanoparticles in this core. Figure IV-13a clearly shows the presence of nanoparticles in the glass of the core from a cane exhibiting a light brown color. The average diameter of the nanoparticles was 6.3 ± 2.1 nm (Figure IV-13b). The small size and volume fraction of these nanoparticles were likely the reason why they were not observed with XRD (in Figure C-1 in Appendix C). It is worth mentioning that these nanoparticles were seen to grow during TEM imaging when exposed to the high energy beam after only a few minutes (see Figure C-11 in Appendix C), a phenomenon that was also observed by Jiang, et al. [22]. The local heat generated by the electron beam energy triggers the thermo-reduction process to a higher extent and provided enough energy for the bismuth ion to diffuse through the glass and aggregate. Hence, the reported average values herein represent an upper limit of the nanoparticle size. High resolution TEM (HR-TEM) experiment was attempted to truly confirm the nature of the nanoparticles but could not be performed due to the instability of the particles under high beam energies (200-300kV).

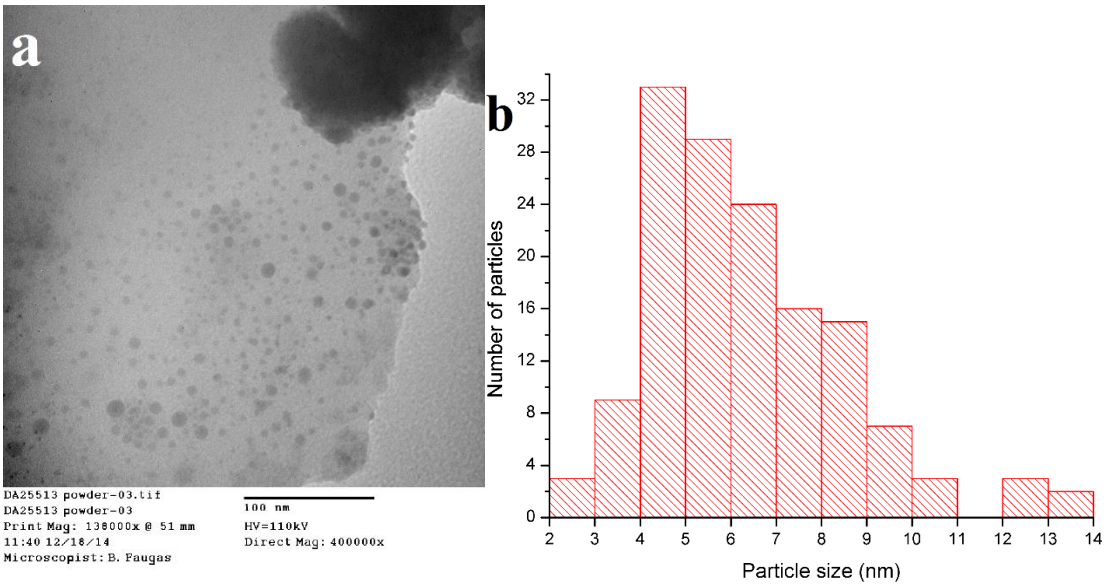

Figure IV-13. (a) TEM micrographs of glass particles obtained from a light brown glass core cane. Nanoparticles were observed and attributed to elemental bismuth metal. The average diameter size of the nanoparticles was found to be 6.3 ± 2.1 nm. (b) Associated histogram showing the particle diameter size distribution of the bismuth nanoparticles.

The effect of cerium oxide as an oxidizing agent was then investigated. The precursor compositions utilized were $99.5Bi_2O_3$-$0.5CeO_2$. These compositions were drawn in the same conditions as the previous draw ("pressed powder pellets" drawn at 1060°C in a 3x30mm borosilicate glass cladding). The color of the obtained core canes was seen to be yellow (see Figure C-12 in Appendix C) compared to the brown color observed without the use of cerium. This change in color indicated a change of the absorption edge of the glass (i.e., a shift towards shorter wavelength)[10] in a similar way to the observation of Sanz, et al., [16]. Although a change in color was observed, this did not necessarily indicate that the formation of bismuth nanoparticles did not take place. TEM experiment was carried out and the presence of nanoparticles (average diameter size of 5.8 ± 2.4 nm) was demonstrated despite the use of cerium

[10] Investigation of the effect of cerium oxide on the transmission properties were attempted by analyzing the brown and yellow core canes with UV-VIS spectroscopy. However, the obtained spectra were unreliable due to too many variable uncertainties (cane geometry, cane core and cladding size differences, aperture shape and size differences in the setup).

oxide (see Figure C-13 in Appendix C). Their average diameter sizes were seen to slightly decrease compared to the draw that did not make use of cerium oxide. One could have expected that with the introduction of cerium oxide in the precursor composition the diameter size of the bismuth metal colloid could be reduced as their formation would be prevented. However, the nanoparticle sizes were similar if one takes into account the standard deviations of the nanoparticle diameter sizes, and cerium oxide did not help in preventing the formation of nanoparticles. Additionally, the use of cerium oxide (in the range of concentration used) did not have a significant effect on the metallic colloid dimensions.

It worth mentioning that while one can think that the change of color was due to the trivalent cerium oxide, which is known to give a yellow color in glasses, another draw that did not make use of cerium oxide exhibited a yellow color as well (see Figure IV-6a and Figure IV-6b in section IV.2.2). Hence, the yellow color observed during cane draw using cerium oxide in the precursor powder composition is the intrinsic color of the glass. The observed change in color of the glass indicated an improvement of transmission properties, in agreement with the observations of Sanz, et al. [16].

It is interesting to note that bismuth nanoparticles still were formed despite the use of cerium oxide. The cerium oxide concentration utilized was likely not sufficient towards the full oxidization of bismuth during cane draw. From redox reactions, a large amount of cerium oxide would be needed to fully oxidize the bismuth ions. Consider the following half redox equations:

$$Bi^0 \leftrightarrow Bi^{3+} + 3e^- \tag{4.3}$$

$$Ce^{4+} + e^{-} \leftrightarrow Ce^{3+} \quad (4.4)$$

The summation of Equations 4.3 and 4.4, and multiplying Equation 4.4 by 4.3 to equilibrate, one arrives with the following equation:

$$Bi^{0} + 3Ce^{4+} \leftrightarrow Bi^{3+} + 3Ce^{3+} \quad (4.5)$$

By transforming this equation into oxide compounds, one gets:

$$2Bi^{0} + 6CeO_2 \rightarrow Bi_2O_3 + 3Ce_2O_3 \quad (4.6)$$

From Equation 4.6, one can see that one needs 6 moles of cerium oxide (IV) in order to fully oxidize bismuth metal to Bi_2O_3. This, in turn, means that a composition of $1Bi_2O_3$-$6CeO_2$ (or $14.3Bi_2O_3$-$85.7CeO_2$ mol%) would be necessary to be drawn. The high melting point of cerium oxide (T_m=2400°C) prevents this composition to be drawn. An attempt at diluting this composition with some glass cladding powder in the precursor mix was made by drawing a powder composition of 50wt%DURAN®-50wt% ($14.3Bi_2O_3$-$85.7CeO_2$ mol%) at 1060°C with the "poured powder" design. However, this draw was unsuccessful as the cerium oxide did not melt (see Figure C-14 in Appendix C).

Furthermore, both yellow and brown cores were observed in a single draw, employing the "poured powder" design (see Figure IV-6). The brown color is known to originate from metallic bismuth nanoparticles, while the origin of the yellow color is unknown. It may be due to the cutoff wavelength of the glass around 400-450 nm (as observed in compositions in Refs. [16], [21]), and yellow could be the complementary color seen from this cutoff absorption wavelength. The difference in color indicates a change in transmission properties, and could originate whether from

a change in concentration, in temperature, in bismuth nanoparticle diameter sizes or, in a reduction in oxygen pressure upon drawing. It has been shown previously that an increase in bismuth oxide concentration in the glass has a tendency to produce darker color glasses and decrease transmission [19]. Interestingly, in the referred draw here, the bismuth oxide concentration was observed to decrease along the length of the cane (see Chapter III section III.4) and the color of the glass changed from yellow (40-50 mol% Bi_2O_3) to light brown (25-39 mol% Bi_2O_3), indicating a reverse trend from that in Ref. [19]. Hence, in this case, the bismuth concentration is not a valid argument to explain the dynamic change of transmission properties. An increase in temperature is also known to produce darker glasses [16] and could be at the origin of the observe change in transmission properties. Nevertheless, the draw temperature was kept constant and, thus, the change did not originate from a difference in temperature. Furthermore, nanoparticles are known to be formed in the yellow and brown core glasses as discussed above. Hence, a difference in nanoparticle sizes could be at the origin of the difference in color (where the color originates from plasmon absorption mechanism or from interband absorption transition of the bismuth nanoparticles that could be considered as semiconductors due to their small size [23], [24]). Analysis of the nanoparticle sizes for that same draw revealed that the yellow and brown core exhibited an average particle diameter size of 4.0 ± 1.8 nm and 5.6 ± 1.9 nm respectively (see Figure C-15 in Appendix C). Hence, the size difference was not seen to be significant such that it could be said to play a significant role in the color changing.

The change in color may be associated with a drop in pressure in (and above) the melt, which can originate from the Venturi effect. This effect relates to fluid flow

through a constricted region, where the fluid experiences a reduction in pressure. In our case, the fluid is the (low viscosity) bismuth silicate oxide melt and the constricted region is the neckdown region where there is a reduction in dimensions of the preform from centimeter to millimeter cane. Hence, the melt is prone to experience a reduction in pressure. From Equation 4.1, a diminution in (oxygen) pressure drives the reaction to the right and thus toward the reduction of the trivalent bismuth ions to bismuth metal. Hence, perhaps this effect is at the origin of the observed dynamic change in color. However, both yellow and brown core cane were known to contain bismuth nanoparticles from the previous TEM experiments. The reduction of bismuth oxide ions still took place from the beginning of the draw, and perhaps the kinetics of the reaction were increased due to the potential pressure drop. In this case, an increase in bismuth nanoparticles per unit volume could take place and increase the absorption properties of the glass. If this explanation does not hold, a change in glass structure would be at the origin of the change in core glass color. Nonetheless, without the possibility of carrying reliable UV-VIS experiments on the colored core canes, it is difficult to compare the results with the literature and make a conclusion on the origin of the different observed colors.

IV.6. Conclusions

In this chapter, the fabrication of bismuth oxide glass core optical fibers in soft glass claddings was investigated using the molten core method. It was found that the bismuth oxide precursor powder was very sensitive to the processing conditions, and more particularly to the precursor density designs. It was demonstrated that a high-density bismuth oxide powder (i.e., “pressed powder pellet” design) did not allow the melting of the precursor powder due to volume expansion. It is thought that the large

volume expansion required for the bismuth oxide solid-solid and solid-liquid phase transitions was prevented by the nearest neighbor particles and by the glass cladding. On the other hand, a low-density bismuth oxide powder (i.e., "poured powder" design) was shown to melt properly due to the large free volume allowed for the precursor powder to expand into. Interestingly, the "pressed powder pellet" design allowed the formation of bismuth silicate crystals in the cane/core (described in more details in Chapter III), whereas the "poured powder" design allowed the formation of an amorphous core.

The effect of the coefficient of thermal expansion mismatch between the bismuth silicate oxide core and the glass cladding was discussed, and its effect on the light transmission properties was demonstrated. It was shown that, when drawing fibers with a borosilicate glass cladding, large cracks were formed in the fiber core upon cleaving. This behavior was related to the stresses built in the core upon cooling due to the large core-clad CTE difference. These large cracks scattered the propagating light and these fibers did not transmit light. An annealing step was shown to remove the cracks and pointed towards a reduction of the built-in stresses. When drawing fibers with a soda-lime silicate glass cladding, no cracks were observed in the fiber core. It was observed that, by lowering the CTE mismatch between core and cladding, the draw-induced stresses were reduced. This, in turn, precluded crack formation and allowed the transmission of light (without any annealing step).

The well-known thermo-reduction behavior of bismuth oxide was also investigated during the drawing of bismuth oxide precursor powder with the molten core method. The formation of nanoparticles within the core glass was observed and was associated

to the formation of metallic bismuth nanoparticles in accordance with the literature. The addition of the oxidizing agent cerium oxide was shown to improve the transmission properties of the glass, but did not show the suppression of the metallic bismuth nanoparticle formation. The low concentration of oxidizing agent used (0.5mol%) was insufficient to reverse the thermo-reduction reaction and was thought to be at the origin of the observed behavior.

IV.7. References

[1] I. Barin, *Thermochemical data of pure substances*, Third edition. Weinheim : VCH, 1995.

[2] W. C. Schumb and E. S. Rittner, "Polymorphism of Bismuth Trioxide," *J. Am. Chem. Soc.*, vol. 65, no. 6, pp. 1055–1060, 1943.

[3] B. Aurivillius and L. G. Sillen, "Polymorphy of bismuth trioxide," *Nature*, vol. 155, pp. 305–306, 1945.

[4] J. Leitner, P. Chuchvalec, D. Sedmidubský, A. Strejc, and P. Abrman, "Estimation of heat capacities of solid mixed oxides," *Thermochim. Acta*, vol. 395, no. 1–2, pp. 27–46, 2003.

[5] N. G. Ainslie, J. D. Mackenzie, and D. Turnbull, "Melting Kinetics of Quartz and Cristobalite," *J. Phys. Chem.*, vol. 65, no. 10, pp. 1718–1724, 1961.

[6] E. M. Levin and R. S. Roth, "Polymorphism of bismuth sesquioxide. I. Pure Bi_2O_3," *J. Res. Natl. Bur. Stand. Sect. A Phys. Chem.*, vol. 68A, no. 2, p. 189, 1964.

[7] M. Hoch, "Thermodynamics and phase diagram of the binary system Bi_2O_3-B_2O_3," *Calphad Comput. Coupling Phase Diagrams Thermochem.*, vol. 20, no. 4, pp. 511–519, 1996.

[8] F. Schröder and N. Bagdassarov, "Phase transitions and electrical properties of Bi_2O_3 up to 2.5 GPa," *Solid State Commun.*, vol. 147, no. 9–10, pp. 374–376, 2008.

[9] M. Yashima, D. Ishimura, and K. Ohoyama, "Temperature dependence of lattice parameters and anisotropic thermal expansion of bismuth oxide," *J. Am. Ceram. Soc.*, vol. 88, no. 8, pp. 2332–2335, 2005.

[10] Schott glass, "Schott DURAN® tubing brochure." [Online]. Available: http://www.us.schott.com/tubing/english/products/DURAN.html.

[11] P. Dragic, C. Kucera, J. Furtick, J. Guerrier, T. Hawkins, and J. Ballato, "Brillouin spectroscopy of a novel baria-doped silica glass optical fiber," *Opt.*

Express, vol. 21, no. 9, pp. 10924–10941, 2013.

[12] M. Cavillon, P. D. Dragic, and J. Ballato, "Additivity of the coefficient of thermal expansion in silicate optical fibers," *Opt. Lett.*, vol. 42, no. 18, p. 3650, 2017.

[13] I. H. Shin, B. H. Kim, S. P. Veetil, W. T. Han, and D. Y. Kim, "Residual stress relaxation in cleaved fibers," *Opt. Commun.*, vol. 281, no. 1, pp. 75–79, 2008.

[14] F. H. El Batal, "Gamma ray interaction with bismuth silicate glasses," *Nucl. Instruments Methods Phys. Res. Sect. B Beam Interact. with Mater. Atoms*, vol. 254, no. 2, pp. 243–253, 2007.

[15] Schott glass, "AR-GLAS® brochure." [Online]. Available: http://www.schott.com/d/tubing/04f08d52-1060-400c-ac91-3d5adfeaca7d/1.0/schott-tubing_brochure_ar-glas_english.pdf.

[16] O. Sanz, E. Haro-Poniatowski, J. Gonzalo, and J. M. Fernandez Navarro, "Influence of the melting conditions of heavy metal oxide glasses containing bismuth oxide on their optical absorption," *J. Non. Cryst. Solids*, vol. 352, no. 8, pp. 761–768, 2006.

[17] M. Peng, C. Zollfrank, and L. Wondraczek, "Origin of broad NIR photoluminescence in bismuthate glass and Bi-doped glasses at room temperature.," *J. Phys. Condens. Matter*, vol. 21, no. 28, p. 285106, 2009.

[18] S. Khonthon, S. Morimoto, Y. Arai, and Y. Ohishi, "Redox equilibrium and NIR luminescence of Bi_2O_3-containing glasses," *Opt. Mater. (Amst).*, vol. 31, no. 8, pp. 1262–1268, 2009.

[19] G. Gao *et al.*, "Effect of Bi_2O_3 on physical, optical and structural properties of boron silicon bismuthate glasses," *Opt. Mater. (Amst).*, vol. 32, no. 1, pp. 159–163, 2009.

[20] M. Peng, C. Wang, D. Chen, J. Qiu, X. Jiang, and C. Zhu, "Investigations on bismuth and aluminum co-doped germanium oxide glasses for ultra-broadband optical amplification," *J. Non. Cryst. Solids*, vol. 351, no. 30–32, pp. 2388–2393, 2005.

[21] Y. Zhang, Y. Yang, J. Zheng, W. Hua, and G. Chen, "Effects of oxidizing additives on optical properties of Bi_2O_3-B_2O_3-SiO_2 glasses," *J. Am. Ceram. Soc.*, vol. 91, no. 10, pp. 3410–3412, 2008.

[22] X. Jiang *et al.*, "Broadband photoluminescence of Bi_2O_3-GeO_2 binary systems: glass, glass-ceramics and crystals," *Laser Phys.*, vol. 23, no. 10, p. 105812, 2013.

[23] Y. W. Wang, J. S. Kim, G. H. Kim, and K. S. Kim, "Quantum size effects in the volume plasmon excitation of bismuth nanoparticles investigated by electron energy loss spectroscopy," *Appl. Phys. Lett.*, vol. 88, no. 14, 2006.

[24] D. Velasco-Arias *et al.*, "Stabilization of strong quantum confined colloidal bismuth nanoparticles, one-pot synthesized at room conditions," *J. Phys. Chem.*

C, vol. 116, no. 27, pp. 14717–14727, 2012.

[25] X. Zhu, C. Mai, and M. Li, “Effects of B_2O_3 content variation on the Bi ions in Bi_2O_3-B_2O_3-SiO_2 glass structure,” *J. Non. Cryst. Solids*, vol. 388, pp. 55–61, 2014.

CHAPTER V

SUMMARY AND FUTURE PERSPECTIVES

Throughout this dissertation, the molten core method was used to investigate the formation of bismuth-containing crystals $Bi_4Ge_3O_{12}$/$Bi_4Si_3O_{12}$ (BGO/BSO) and bismuth-containing glasses during optical fiber draw, with a specific focus on the thermodynamic-kinetic interplay offered by said method. This section will review key results found throughout each chapter of this dissertation. Note that all conclusions made herein are only valid for the bismuth silicate oxide system drawn in soft glass claddings.

V.1. Summary

This dissertation began with the investigation of the formation of a single phase pure BGO crystalline core optical fiber for electro- and nonlinear-optic applications. Two designs were employed and yielded the formation of BGO crystals in fiber canes (large diameter fibers). In a first design employing a BGO single crystal precursor sleeved into a borosilicate glass cladding, the core was found to be polycrystalline due to a lack of Bi_2O_3 in the core melt. This arose from the glass clad-core interaction inherent to the molten core method. With the desire to fabricate a single phase crystalline core, the second approach employed the same BGO precursor single crystal but with additional Bi_2O_3 powder. The resultant core showed a core structure close to a single phase, confirming the necessity of retaining a higher Bi_2O_3 concentration in the core melt to fabricate a single phase crystalline core. Moreover, it was found in both cases that glass cladding incorporation was not an impediment to the crystallization process as the glass cladding compounds could substitute for compounds of eulytine crystal structure (specifically SiO_2 for GeO_2), which

ultimately led to the formation of $Bi_4(Ge_{1-x}Si_x)_3O_{12}$ (BGSO) crystals. Both designs employed exhibited a single crystalline-like core with heavily preferred crystal orientation. The origin and understanding of this latter aspect is still unclear.

With the formation of an acentric oxide phase demonstrated, it was then desired to understand the mechanisms for crystallization of the eulytine crystal structure during the draw in order to define boundaries to the thermodynamic-kinetic interplay. Three routes were explored for that purpose: homogeneous nucleation, heterogeneous nucleation and, the phase transformation $2Bi_2SiO_5 + SiO_2 \rightarrow Bi_4Si_3O_{12}$. Homogeneous nucleation was investigated employing Bi_2O_3 powder inserted in a borosilicate glass cladding. The resultant fabrication of a core showing a composition close to the BSO or Bi_2SiO_5 crystal stoichiometry with an amorphous structure refuted homogeneous nucleation as a mechanism for crystallization of BGO/BSO oxide crystals. The heterogeneous nucleation mechanism was then investigated, using two approaches. In a first approach (respectively, a second approach), a precursor mix of BGO crystal powder with Bi_2O_3 powder (respectively, a BGO pellet with additional Bi_2O_3 powder on top) was drawn in a borosilicate glass cladding. The formation of a polycrystalline BGSO core was demonstrated in both cases and confirmed that BGO seeds were necessary for nucleation. Thus, heterogeneous nucleation was validated as a crystal growth mechanism in the Bi_2O_3-SiO_2 system using the molten core method. Finally, the crystallization of BSO through the reaction path $2Bi_2SiO_5 + SiO_2 \rightarrow Bi_4Si_3O_{12}$ was investigated using Bi_2O_3 pressed powder pellets to form the metastable phase Bi_2SiO_5 in cane and then redraw the cane to fiber. While the unique formation of BSO crystals in fibers was observed using borosilicate glass claddings, it could not be (truly) pinpointed as originating from this reaction.

While this approach demonstrated the crystallization of phase pure BSO crystals in fibers without the necessity of a BGO seed, the crystallization mechanism of BSO in this case is unclear due to the dynamics of the molten core method.

With the formation and mechanism for oxide core crystals explored, the processing conditions that lead to amorphous bismuth oxide core optical fibers were next investigated. First, it was found that the melting behavior of the precursor powder was sensitive to the materials' processing conditions. Specifically, pressed powder pellets (i.e., "high density" powder) were shown to exhibit a non-melting behavior thought to originate from a volume expansion effect. Second, it was found that the core-clad CTE mismatch had an extensive impact on the stresses build during fiber draw. Using a borosilicate glass cladding, large cracks in the core would be formed upon cleaving and the necessity to anneal the fiber was underlined to keep the cores' integrity for future use. This glass cladding was deemed impractical for processing bismuth oxide (in addition to its poor mechanical properties). Instead, soda-lime silicate glass cladding offered better CTE matching as well as better mechanical properties. Third, the intrinsic thermo-reduction behavior of bismuth oxide to bismuth metal nanoparticles was investigated. The presence of nanoparticles was shown when processing the powder in borosilicate glass-cladded fibers. The use of an oxidizing agent (CeO_2) was shown to have an effect on the color of the glass (and hence transmission properties) but was not shown to prevent nanoparticle formation.

V.2. Limitations and future perspectives

V.2.1. Crystalline core oxide optical fibers

This work aimed to answer these main questions: *where does one draw the limit for the thermodynamic-kinetic interplay during optical fiber draw?* Or, *when does the*

thermodynamic take over the kinetic? Within this dissertation, a preliminary (but not limited to) answer was given using the bismuth germanate and bismuth silicate oxide systems: thermodynamic can take over during fiber draw if a foreign crystal surface is present. While this provides only part of the mystery, this dissertation further raised questions and additional experiments are required.

First and foremost, there is perhaps the question about the nature of surface that needs to be answered, i.e., *does the nature of the foreign surface need to be similar to that of the targeted crystals?* Or, *could it be of any crystal type such as it could reduce the thermodynamic barrier for nucleation?*

Second, the work undertaken in this dissertation was associated with drawing fibers in soft glass cladding tubes (i.e., in the drawing temperature range of 850-1100°C). Hence, as most optical fibers are drawn in silica at high temperatures (~2000°C), the natural question of *could one crystallized oxide crystals while drawing in silica glass?* comes to mind. Moreover, if one desires to control the nucleation with a foreign surface, *could the foreign surface integrity be kept (i.e., stay undissolved by the melt)?* Perhaps an answer to that latter question could be started by investigating the semiconductor elements (e.g., Ge) as a seed, as these elements are known to crystallize within fiber draw [1].

V.2.1.1. The challenge of crystalline core in flexible and long length fibers

First, it is important to recognize the limitations found in this dissertation towards the fabrication and development of crystalline oxide core optical fibers. Omitting the three requirements of phase purity, single phase and, single crystallinity, the (fourth?) requirement of long length (>1 m) was not achieved. Phase pure samples exhibiting a

single phase core were only demonstrated over millimeter length in cane and further investigation of the effect of drawing speed on core crystallization length is necessary.

Ultimately, this somewhat troublesome aspect of long crystal core fiber length would require one to control the core cladding interaction during fiber draw such that the core melt stoichiometry is preserved. This latter aspect is quite difficult to control (as of right now) as the molten core approach is a highly dynamic method and, concentration gradients arise not only in the core cross-section but also along the fiber axis. Nonetheless, melts with enriched Bi_2O_3 concentration compared to the BSO stoichiometry were demonstrated and thus leave hope for reaching stoichiometric melt over a few centimeters, at least in canes (i.e., in millimeter size fibers). In the case of flexible fibers (i.e., micrometer size fibers), high precursor concentration retained in the fiber core are more restricted due to the dynamics of the molten core method (smaller fiber diameter usually tends to exhibit smaller concentration of the initial precursor [2]) but, are not thought to be impossible. If one can retain a high amount of precursor in the fiber, lengths on the order of a meter could be achieved. If the answer lies in molten flow dynamics, perhaps the effect of preform sizes may need to be explored. An experiment employing a 1.2 mm BGO single crystal as a precursor sleeved in a borosilicate glass cladding with dimensions of 1.2x12 mm drawn to large fiber diameter (such as 250-500 μm) would be a first start to verify if crystals can be crystallized in flexible fibers (and eventually over long length). A similar approach to that used in section III.5.2 with additional Bi_2O_3 powder on top could potentially allow a single phase crystalline oxide core to be fabricated.

V.2.1.2. Which oxide crystals could, realistically, be formed in optical fibers using the molten core method?

The second limitation comes with the aforementioned inherent core-clad interaction of the molten core when using oxide systems[11]. Oxide precursor systems mix well with the oxide glass cladding compounds and this behavior would limit the fabrication of oxide crystalline core fibers to crystals in the silicate family when one works with commercially available glass cladding systems such as borosilicate or silica glass claddings. Moreover, including the first limitation mentioned above, the desired silicate crystal would necessitate a stoichiometry with at least a silica content of 50-60 mol%. In the case of noncentrosymmetric crystals, this limits the choice to a few potential crystals only ($K_2Si_3ZrO_9$, $CaZrSi_2O_7$, $SrSi_2VO_7$, $BaTiSi_3O_9$)[12] [3]. Further assuming the isomorphism of SiO_2 and GeO_2 in crystal structures, two other oxide compounds ($Li_2Ge_2O_5$, $Cd_2Ge_7O_{16}$)[13] [3] could eventually be added to the list. Note that the isomorphism assumption is more prone to be valid for compounds within which GeO_2 adopts a tetrahedral coordination state rather than an octahedral coordination state as SiO_2 rarely adopts the octahedral state [4], and, thus, the isomorphism between $Cd_2Ge_7O_{16}$ and $Cd_2Si_7O_{16}$ is unlikely to take place [5]. In the case of rare-earth host crystals for laser applications, the Y_2O_3-SiO_2 phase diagram offers silicate structures such as Y_2SiO_5 or $Y_2Si_2O_7$.

[11] In comparison, semiconductors core optical fibers showed limited core-clad interaction, with the sole incorporation of oxygen element in the core as seen from the results depicted in [12]. As intriguing as it is, the reason for this behavior is unclear and may lie within the thermodynamics of mixing of oxides and semiconductor elements/compounds.

[12] $K_2Si_3ZrO_9$ = $20K_2O$-$20ZrO_2$-$60SiO_2$; $CaZrSi_2O_7$ = $25CaO$-$25ZrO_2$-$50SiO_2$; $SrSi_2VO_7$ = $28.5SrO$-$14.3V_2O_4$-$57.2SiO_2$; $BaTiSi_3O_9$ = $20BaO$-$20TiO_2$-$60SiO_2$.

[13] $Li_2Ge_2O_5$ = Li_2SiO_5 = $33.3Li_2O$-$66.7SiO_2$; $Cd_2Ge_7O_{16}$ = $Cd_2Si_7O_{16}$ = $22.2CdO$-$77.8SiO_2$.

V.2.2. Bismuth-containing glass optical fibers

With the understanding of essential processing conditions for the fabrication of optical fibers using the molten core method, optical fibers containing a large amount of bismuth oxide (17-27 mol% Bi_2O_3, or 55-66 wt% Bi_2O_3) were fabricated and require investigation of their optical properties. Specifically, the transmission losses and nonlinearities (i.e., nonlinear refractive index and nonlinear parameter) need to be measured to evaluate their properties. Moreover, their Brillouin gain coefficient (BGC) could be investigated for sensor application purposes as bismuth silicate glass system possess a large BGC [6].

Furthermore, the same fibers could be investigated for their luminescence properties. Bismuth-doped optical fibers are known to exhibit luminescent properties of interest with broad emissions in the telecommunication window [7]. The study of luminescent properties on the high bismuth concentration end in optical fibers have not been yet explored and could help in understanding the bismuth related NIR emitting centers in fibers [8]. Note that luminescent properties in bismuth oxide materials may originate from the presence of bismuth nanoparticles [9].

Which materials for high nonlinear optical fibers using the molten core method?

The molten core method offers a unique opportunity for exploring new optical fiber materials. While bismuth oxide offers some of the highest nonlinearities in the oxide family, it is perhaps difficult to pinpoint if nonlinearities originate from metallic bismuth nanoparticles through surface plasmon resonance effect (since bismuth nanoparticles are likely present in the glass core) or from the electronic polarization of bismuth oxide. Hence, other compounds that exhibit high electronic polarizability (or

high nonlinear refractive index) could be easier to analyze and are of interest as well. Such compounds are Na_2O, CdO, ZnO, Nb_2O_5, V_2O_5, TeO_2, Ta_2O_5 [10]–[12].

V.3. References

[1] J. Ballato *et al.*, "Advancements in semiconductor core optical fiber," *Opt. Fiber Technol.*, vol. 16, no. 6, pp. 399–408, 2010.

[2] J. Ballato *et al.*, "On the fabrication of all-glass optical fibers from crystals," *J. Appl. Phys.*, vol. 105, no. 5, p. 53110, 2009.

[3] P. S. Halasyamani and K. R. Poeppelmeier, "Noncentrosymmetric Oxides," *Chem. Mater.*, vol. 10, no. 10, pp. 2753–2769, 1998.

[4] A. Durif-Varambon, "Etude de la substitution du silicium dans quelques types d'orthosilicates," *Bull. la société française minéralogie Cristallogr.*, vol. 82, pp. 285–314, 1959.

[5] E. Plattner and H. Völlenkle, "Die Kristallstruktur der Verbindung $Cd_2Ge_7O_{16}$," *Monatshefte für Chemie*, vol. 108, no. 2, pp. 443–449, 1977.

[6] J. H. Lee, T. Nagashima, T. Hasegawa, S. Ohara, N. Sugimoto, and K. Kikuchi, "Bismuth-oxide-based nonlinear fiber with a high SBS threshold and its application to four-wave-mixing wavelength conversion using a pure continuous-wave pump," *J. Light. Technol.*, vol. 24, no. 1, pp. 22–27, 2006.

[7] I. A. Bufetov and E. M. Dianov, "Bi-doped fiber lasers," *Laser Phys. Lett.*, vol. 6, no. 7, pp. 487–504, 2009.

[8] E. M. Dianov, "Nature of Bi-related near IR active centers in glasses: state of the art and first reliable results," *Laser Phys. Lett.*, vol. 12, no. 9, p. 95106, 2015.

[9] R. Butkutė *et al.*, "Bismuth quantum dots and strong infrared photoluminescence in migration-enhanced epitaxy grown GaAsBi-based structures," *Opt. Quantum Electron.*, vol. 47, no. 4, pp. 873–882, 2015.

[10] V. Dimitrov and S. Sakka, "Linear and nonlinear optical properties of simple oxides. II," *J. Appl. Phys.*, vol. 79, no. 3, p. 1741, 1996.

[11] V. Dimitrov and S. Sakka, "Electronic oxide polarizability and optical basicity of simple oxides. I," *J. Appl. Phys.*, vol. 79, no. 3, p. 1736, 1996.

[12] V. Dimitrov and T. Komatsu, "Classification of oxide glasses: A polarizability approach," *J. Solid State Chem.*, vol. 178, no. 3, pp. 831–846, 2005.

APPENDICES

APPENDIX A

Complementary experiment for BGO melt interaction with a silica cladding:

The interaction of a BGO melt with silica was investigated further with a simple experiment, where a BGO single crystal of 1.2 mm diameter was sleeved in a silica capillary of 2.47 mm core diameter and melted in a box furnace at 1100°C for six minutes before cooling to room temperature by turning off the oven. This experiment aimed to better understand cladding dissolution by the BGO melt.

The BGO single crystal melted and took the shape of the capillary, yielding a white opaque core upon cooling. Figure A-14 illustrates a SEM micrograph representative of the capillary core and this latter depicted needles and droplet/clovers microstructures. Quantitative analysis of the core composition yielded an average core composition of $66.1SiO_2$-$25.8GeO_2$-$8.1Bi_2O_3$ in the droplets/clovers and $31.7SiO_2$-$43.9GeO_2$-$24.4Bi_2O_3$ on the needles, thus demonstrating a large silica incorporation. Moreover, the Bi_2O_3/GeO_2 ratio was shown to be 0.56, demonstrating a larger loss of Bi_2O_3 under the static conditions used herein. The temperature used in this experiment corresponded roughly to the T_g of silica and the cladding was then in a highly viscous state. Thus, the incorporation of silica was a diffusion process and was mainly imparted from cladding dissolution by the BGO melt. The melt physically ruptured the silica bonds and then silica diffused into the melt. Additionally, Bi_2O_3 has a high partial vapor pressure and evaporation of Bi_2O_3 molecules contributed to its loss.

Although the composition was not close to any known crystalline structure, the white color of the core most likely indicated the presence of crystalline phases that would have scattered light around. In the effort of unveiling the possible presence of

crystallinity, EBSD experiment was carried out on the core sample. Several phases were inputted in the computer software for matching search: $Bi_4Si_3O_{12}$, $Bi_4Ge_3O_{12}$, Bi_2SiO_5, Bi_2GeO_5 and $Bi_2Ge_3O_9$. Figure A-15 exhibits the SEM micrograph and the associated color phase match picture of the core. Bi_2SiO_5 and Bi_2GeO_5 crystalline phases were detected on the needles while the clovers did not match with any crystalline phases. Hence, it was demonstrated that in addition to silica cladding dissolution, the silica molecules reacted with the melt to form the Bi_2SiO_5 crystalline structure. This phase was shown in the literature to be a metastable structure that easily crystallizes upon cooling. Thus, this experiment confirmed the importance of the kinetics of glass formation in both Bi_2O_3-GeO_2 and Bi_2O_3-SiO_2 systems as well as the complexity of the underlying thermodynamics.

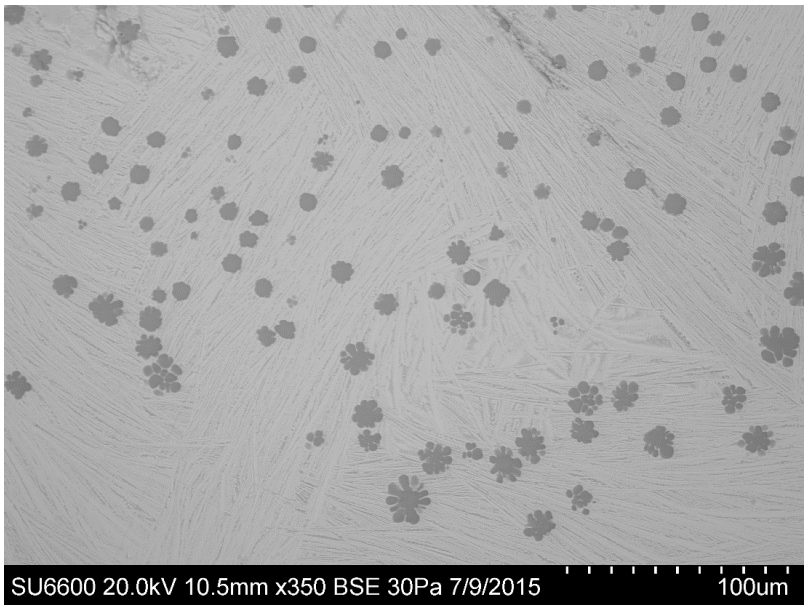

Figure A-14. SEM micrograph of a magnified core cross section of BGO single crystal melted in a silica capillary. Needle-like microstructures are observed (in bright) as well as clovers (in dark). The droplets/clovers are richer in silica than the matrix.

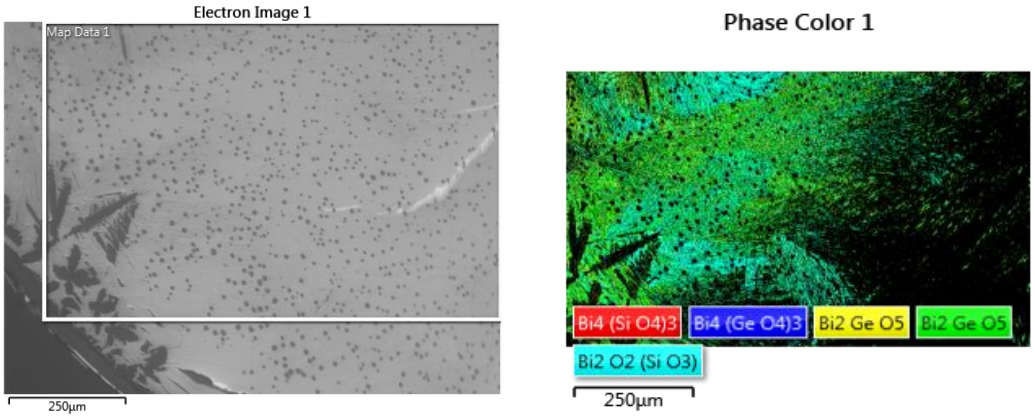

Figure A-15. SEM micrograph of the area taken for investigation (white rectangle) and its associated color phase match picture. Bi_2GeO_5 and Bi_2SiO_5 crystalline structures are detected and matched with the needle-like microstructures.

2nd draw design: BGO single crystal surrounded by $80GeO_2$-$20Bi_2O_3$ powder mix

This draw employed a 1.2 mm diameter BGO single crystal surrounded by a powder mix design, using an $80GeO_2$-$20Bi_2O_3$ powder mix. The preform was drawn at 1080°C at a speed of 0.3 $mm.min^{-1}$. A white core cane and a pink core cane were obtained. Figure A-16 depicts the picture of the pink core cane drawn. Bubbles were observed throughout the length of the core and are attributed to evaporation of GeO_2 due to the large vapor pressure of GeO_2 [1]. The compound concentration of the pink core was found to be $21.1SiO_2$-$69.9GeO_2$-$8.1Bi_2O_3$-$1.1Al_2O_3$ at core center (Figure A-16b). The large amount of GeO_2 and low amount of Bi_2O_3 likely originates from the drawing of the powder mix melt (without mixing of the BGO single crystal melt). This would be supported by the observation that this pink cane was drawn after the white core cane (which is known originate from the BGO single crystal melt).

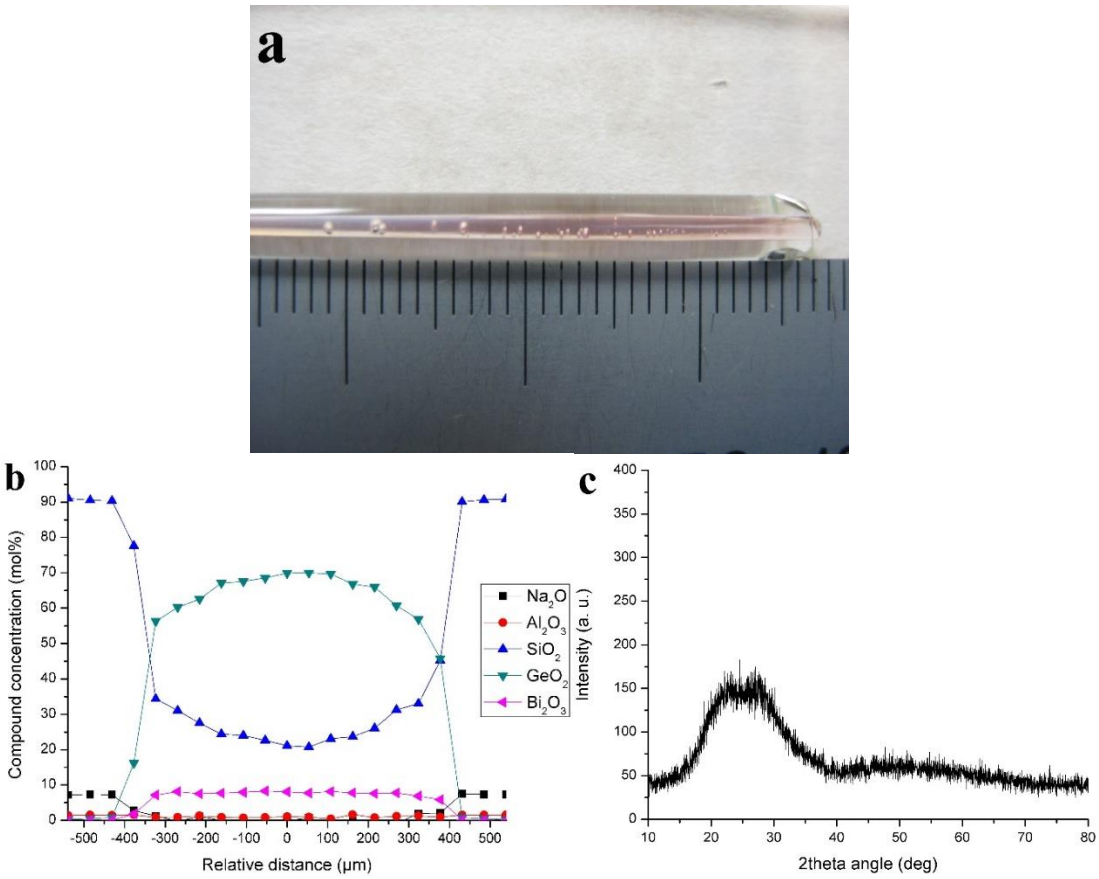

Figure A-16. (a) Picture of the pink core cane obtained from the second draw design employing an $80GeO_2$-$20Bi_2O_3$ powder mix surrounding the BGO single crystal. The ruler gradients are in millimeter. (b) EDX compound concentration profile across the pink core cross section. (c) XRD diffractogram performed on the pink core phase. The core was found amorphous.

Figure A-17 illustrates the SEM micrographs of the cane cross section from the white core cane. The cane was 3.85 mm diameter and the core was 450 µm diameter. Small homogeneous grains were observed in a similar manner to that obtained with the first design and were found to correspond to BGSO crystals through XRD and EBSD (Figure A-18 and Figure A-19). These grains were found to be grown from a bismuth-poor melt and, the amount of the Bi_2O_3 was found to be the critical parameter towards the formation of a single homogeneous phase. Note that in this case though, the crystal structure was closer to that of BGO compared to the 1st design. Indeed, the crystalline peaks observed in Figure A-18 match closely that of the BGO crystal

precursor and very small peak shifts were observed 0.07° to 0.28°, indicating a low amount of silicon atoms in the crystal structure. This showed that the surrounding powder mix used in the 2nd design effectively raised the amount of GeO_2 in the BGO melt. Figure A-19 exhibits the IPF orientation maps taken on the white core cane cross section along the X, Y and Z direction. Each map shows single plane orientations of the BGO crystals regarding the measured axis. Hence, the core was found to be single crystal-like despite polycrystallinity.

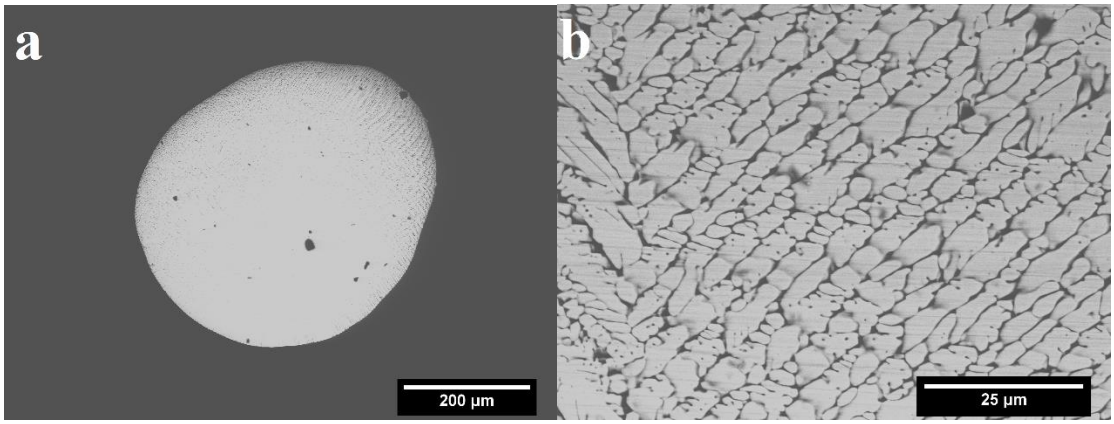

Figure A-17. (a) SEM micrographs of a white core cane cross section obtained from the second design, involving a BGO single crystal surrounded by an $80GeO_2$-$20Bi_2O_3$ powder mix. (b) SEM micrograph of the same core taken at higher magnification. Small homogeneous grains were observed.

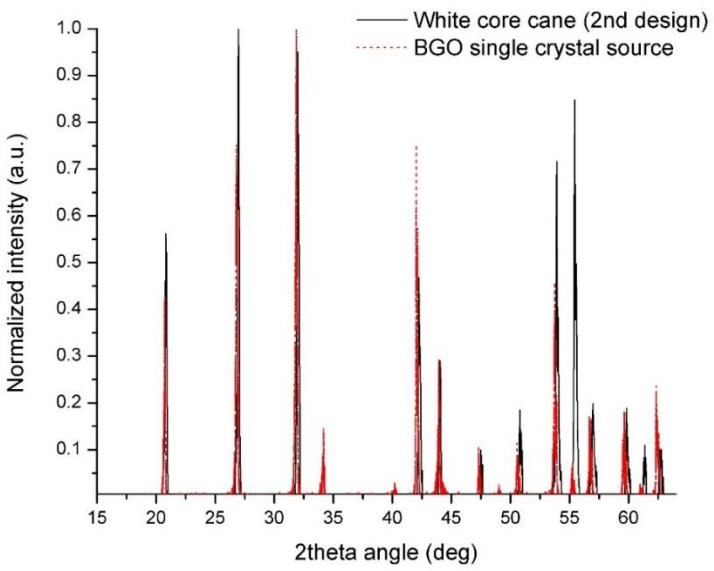

Figure A-18. XRD diffractogram of the white core cane obtained from the second design employing a powder mix of $80GeO_2$-$20Bi_2O_3$ surrounding the BGO single crystal. The peaks were matched with the BGO eulytine crystal structure.

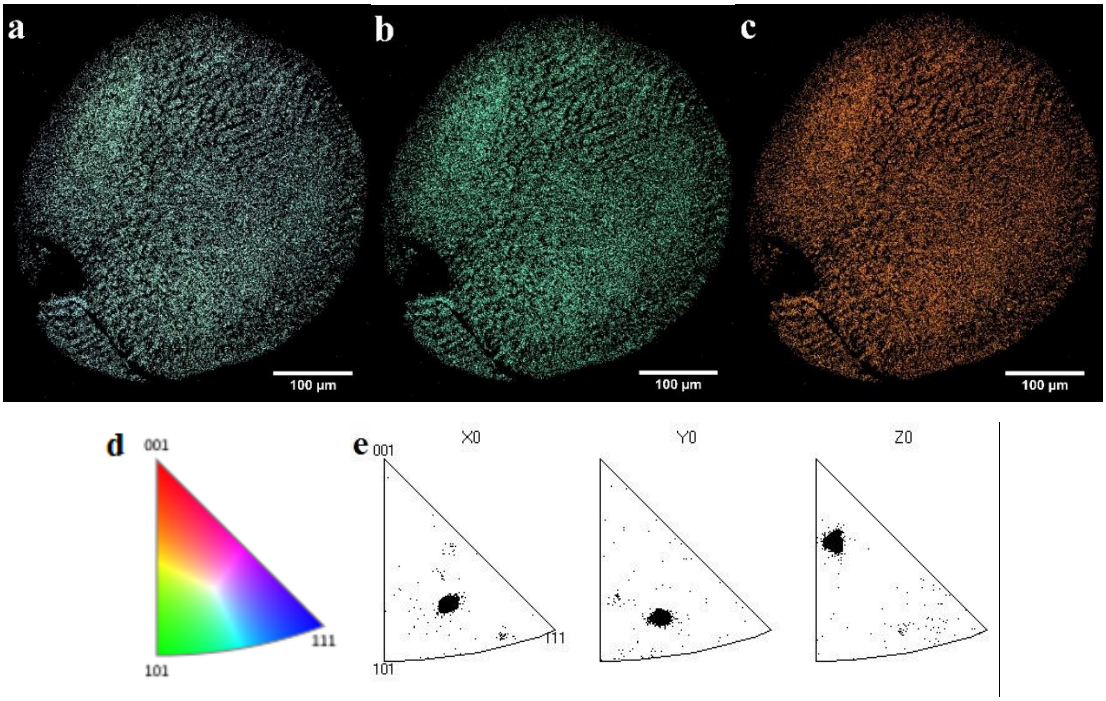

Figure A-19. IPF orientation maps in the (a) X, (b) Y, and (c) Z direction obtained for the core drawn with the second design. (d) hkl planes color-matching legend. A single color is observed for each direction map revealing a single crystal-like plane orientation. e) Color matching between each pixel of the IPF orientation map and the orientation color-scale, showing heavy preferred crystal orientation along each axis (i.e., single crystal-like).

It was demonstrated here that by tuning the composition of the surrounding powder, a larger amount of GeO_2 was retained in the crystal structure. The material transport of the Bi_2O_3 compound was found to be the limiting mechanism towards the formation of a single crystal phase (in terms of microstructure). More importantly, this experiment showed that through preform design and composition design, one can tune the crystal composition and crystal structure of grown crystals.

References

[1] R. H. Lamoreaux, D. L. Hildenbrand, L. Brewer, and L. Brewer, "High-Temperature Vaporization Behavior of Oxides II . Oxides of Be, Mg, Ca, Sr, Ba, B, Al, Ga, In, Tl, Si, Ge, Sn, Pb, Zn, Cd and Hg," *J. Phys. Chem. Ref. Data*, vol. 16, no. 3, pp. 419–443, 1987.

APPENDIX B

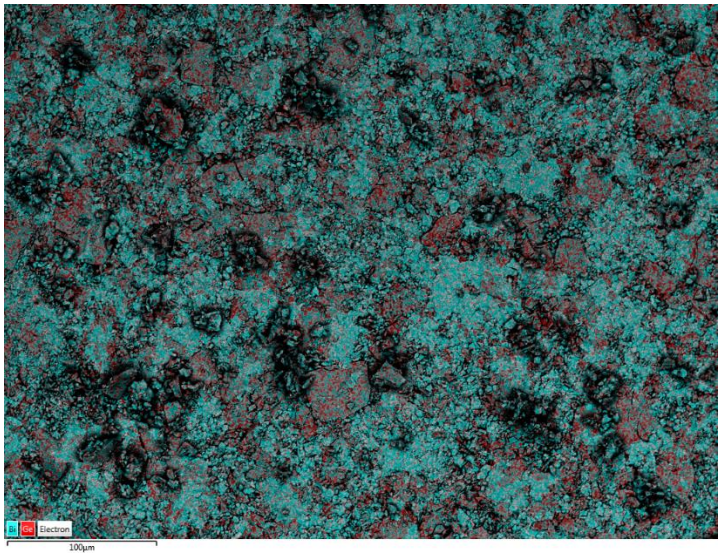

Figure B-1. SEM micrograph with overlaid EDX map showing the repartition of Bi and Ge elements in a pellet comprising a mix of BGO and Bi_2O_3 crystal powder. The Ge element originating from the BGO powder shows that BGO particles are homogeneously spread in the mix. Aggregates larger than 80 µm were not observed, showing that the BGSO crystalline core observed in Chapter III section III.5.1 did not originate from aggregates in the precursor mix.

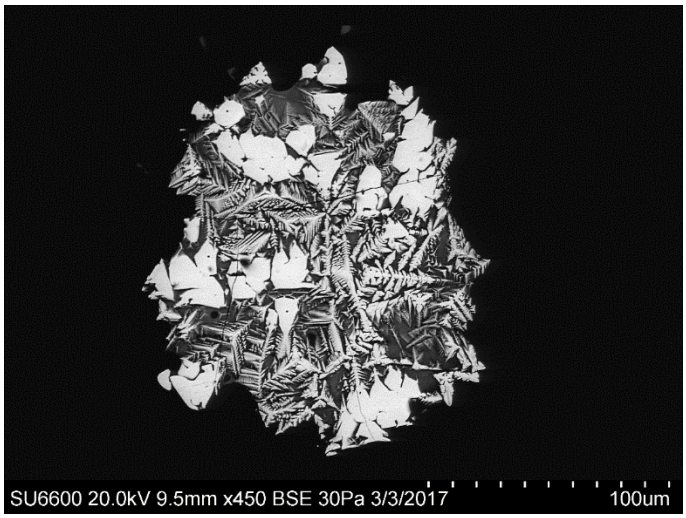

Figure B-2. SEM micrograph of a core drawn at 1000°C from a BGO powder packed in a 3x30 mm borosilicate glass cladding. The observed core is highly non-circular due to the powder that did not melt entirely and was likely to be only partially dissolved. Plus, blob-like structures as well as dendrite-like ("pine tree") crystals were seen, the latter structures indicating crystal growth from a very bismuth-poor melt. The difference in structures between this core and that observed in Chapter III section III.5.1 indicated that in the latter case the crystals were grown through heterogeneous nucleation rather than being the result of non-molten BGO powder.

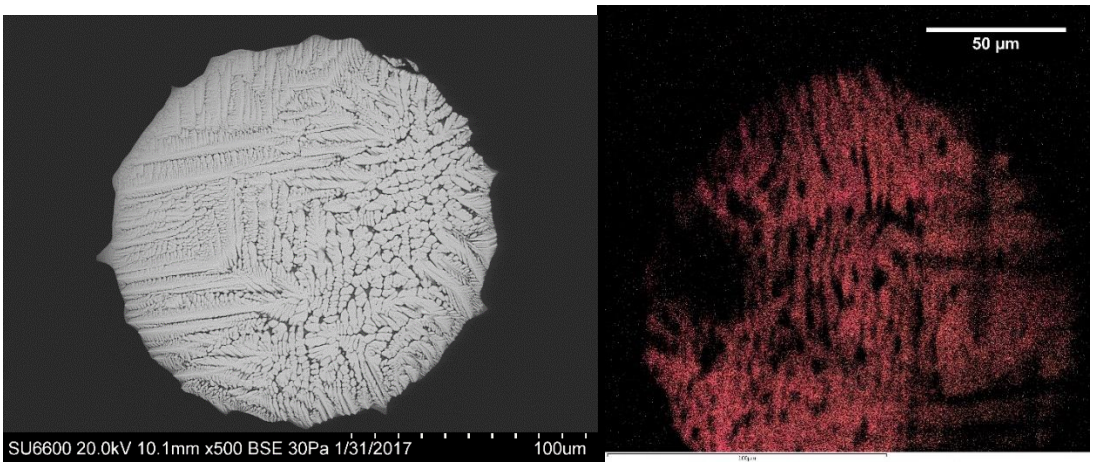

Figure B-3. (a) SEM micrograph of a core cross section obtained from drawing a BGO-Bi_2O_3 powder mix packed in a 3x12mm borosilicate glass cladding at 1000°C with a speed of 0.7 $mm.min^{-1}$. (b) Associated Z-axis orientation map gathered using EBSD analysis showing that all crystals in the core grew along the same direction. The core drifted during analysis and thus the bottom part of the core was cut.

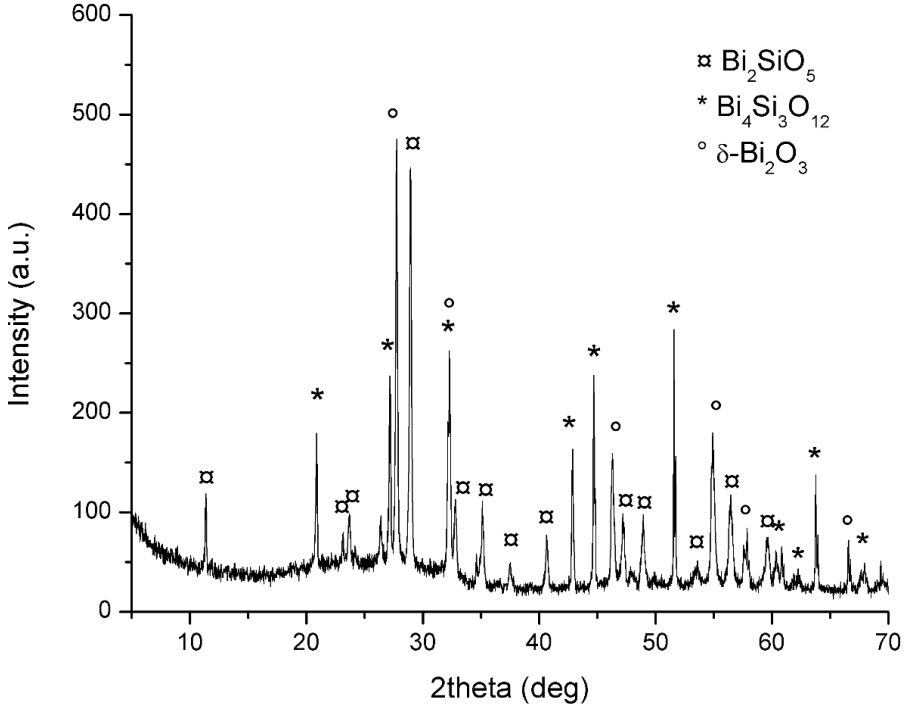

Figure B-4. PXRD diffractogram of the yellow core cane obtained from drawing Bi_2O_3 pellets in a borosilicate glass cladding preform. Crystalline peaks were observed and matched with Bi_2SiO_5, $Bi_4Si_3O_{12}$ and δ-Bi_2O_3.

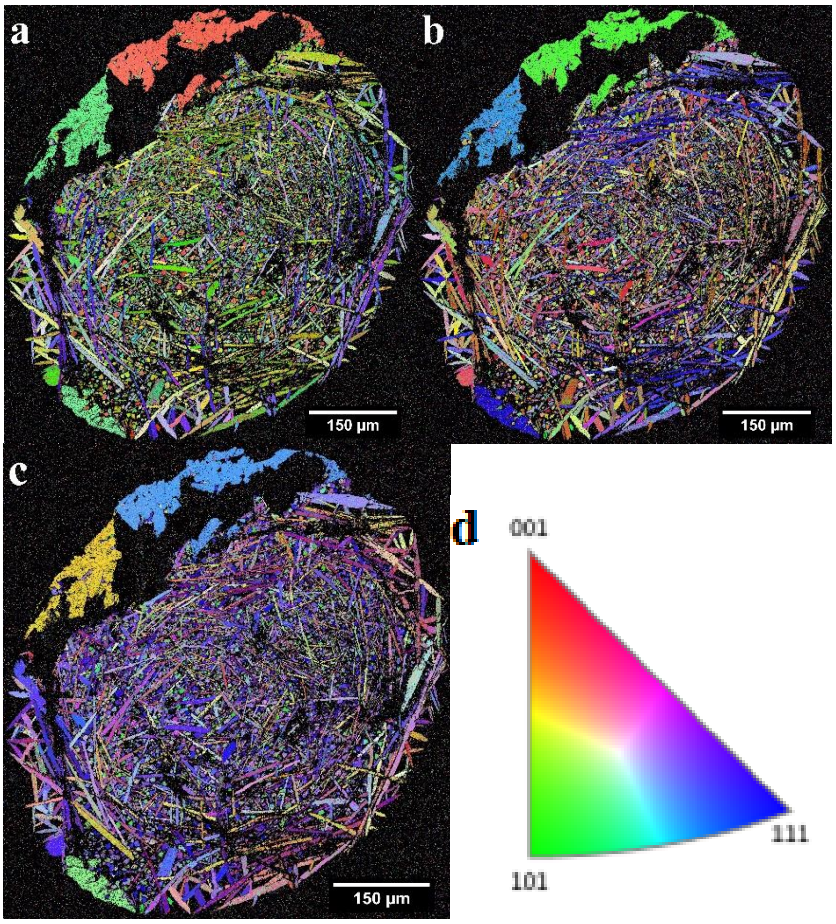

Figure B-5. IPF orientation maps along the a) X-, b) Y- and, c) Z-axis of the yellow core cane obtained from Bi_2O_3 pellets drawn in a borosilicate glass cladding. d) Stereographic triangle showing the orientation color-scale. Random crystal plane orientations were observed for each crystalline structure.

Table B-1. Plane orientations of the BSO crystals observed in above EBSD picture.

Grain	Plane grown in X axis	Plane grown in Y axis	Plane grown in Z axis
Lower left	4-31	56-5	146
Upper left	3-4-1	65-3	205
Upper right	1-62	6-1-4	324

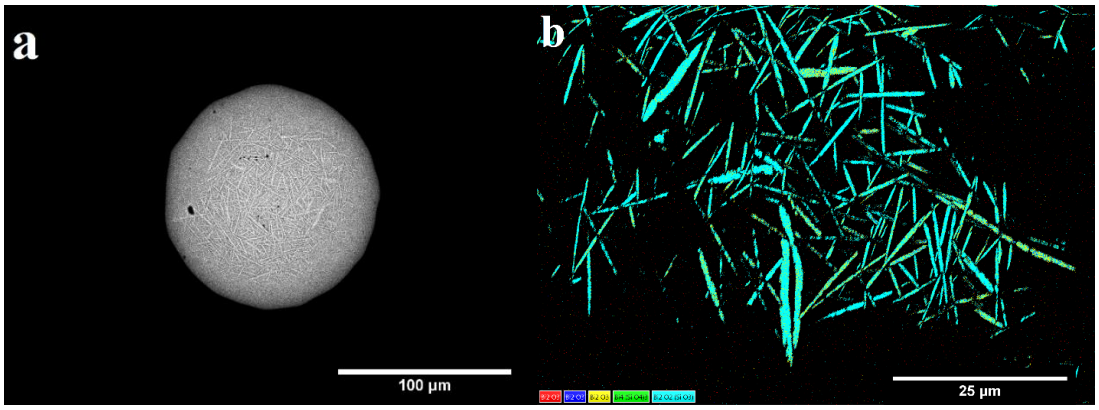

Figure B-6. (a) SEM micrograph of a white core cane cross-section derived from Bi_2O_3-B_2O_3-CeO_2 in AR-GLAS® revealing needle-like microstructures. The cane is 1.2 mm diameter and the core is 120 µm diameter. (b) EBSD phase color matching image of the white core cane cross section. Needle-like microstructures are matched with the metastable Bi_2SiO_5 crystal structure. Legend: blue cyan = Bi_2SiO_5, green = $Bi_4Si_3O_{12}$, yellow = β-Bi_2O_3, blue = γ-Bi_2O_3, red = α-Bi_2O_3.

Complementary experiment for the interaction of a large BGO single crystal precursor:

A large diameter BGO single crystal (3 mm) was sleeved in a 3x30 mm borosilicate glass cladding and drawn at 1080°C. Figure B-7 depicts an optical micrograph of the beginning of the draw exhibiting core sample. A large bulge was observed with a cane diameter of 3.2 mm. The core was 2.4 mm diameter and exhibited a single phase with a composition of $61.4GeO_2$-$37.6Bi_2O_3$-$0.5SiO_2$-$0.4Al_2O_3$ at core center. Clearly, the large core diameter in addition to the stoichiometric composition close to BGO revealed that the BGO single crystal did not melt at the beginning of the draw. Interestingly, the core seemed to have exhibited a large progressive reduction in diameter during the draw. The sample in Figure B-7 was polished along the longitudinal axis to investigate the melting evolution of the precursor crystal. Figure B-8 depicts a series of images taken at the core-cladding interface along the core sample showing the evolution of the core structure. Figure 8a corresponds to the

beginning of the bulge (i.e., begin of draw) and Figure 8k corresponds to the end of the core sample. In all micrographs, the bright phase is the core sample and the dark phase corresponds to the surrounding glass cladding. The homogeneous phase seen in Figure B-8a, b, c, d, e and f correspond to the non-molten BGO single crystal precursor. Grains as well as dendrite-like microstructures were observed at the core-cladding interface, showing crystallization from a melt likely formed by the dissolution of the BGO crystal by the glass cladding. Figure B-8e and Figure B-8f show the moment (frozen in time) at which the BGO crystal precursor fully melted. The homogeneous non-molten BGO crystal phase is not seen anymore and small homogeneous grains were seen in a bismuth-poor matrix. This likely indicated that the BGO precursor melted and the microstructures observed from thereon (i.e., in Figure B-8g, h and i) were crystals resulting from the crystallization of the melt.

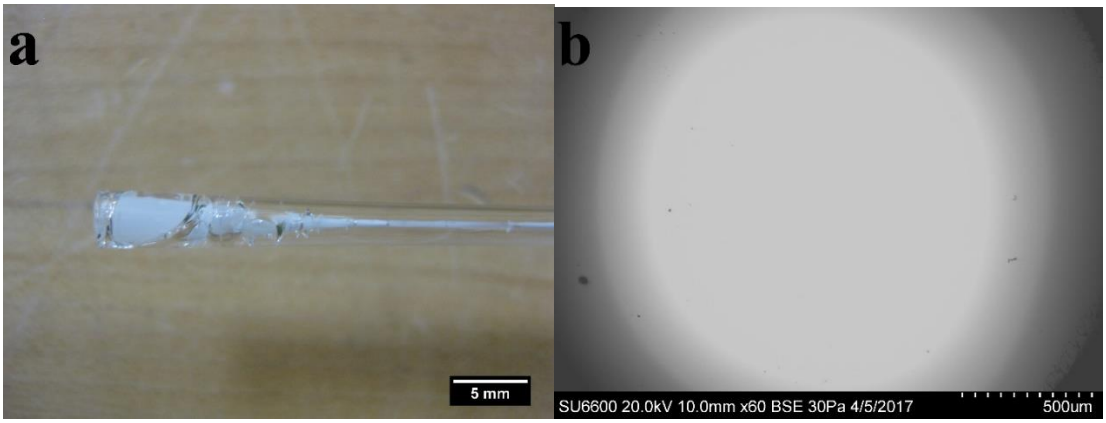

Figure B-7. (a) Optical micrograph of the beginning of the draw exhibiting core sample. A large bulge was observed and was shown to correspond to the BGO single crystal precursor that did not melt. (b) SEM micrograph of the large bulge cross-section. The core was 2.4 mm diameter and showed a homogeneous phase across the entire core.

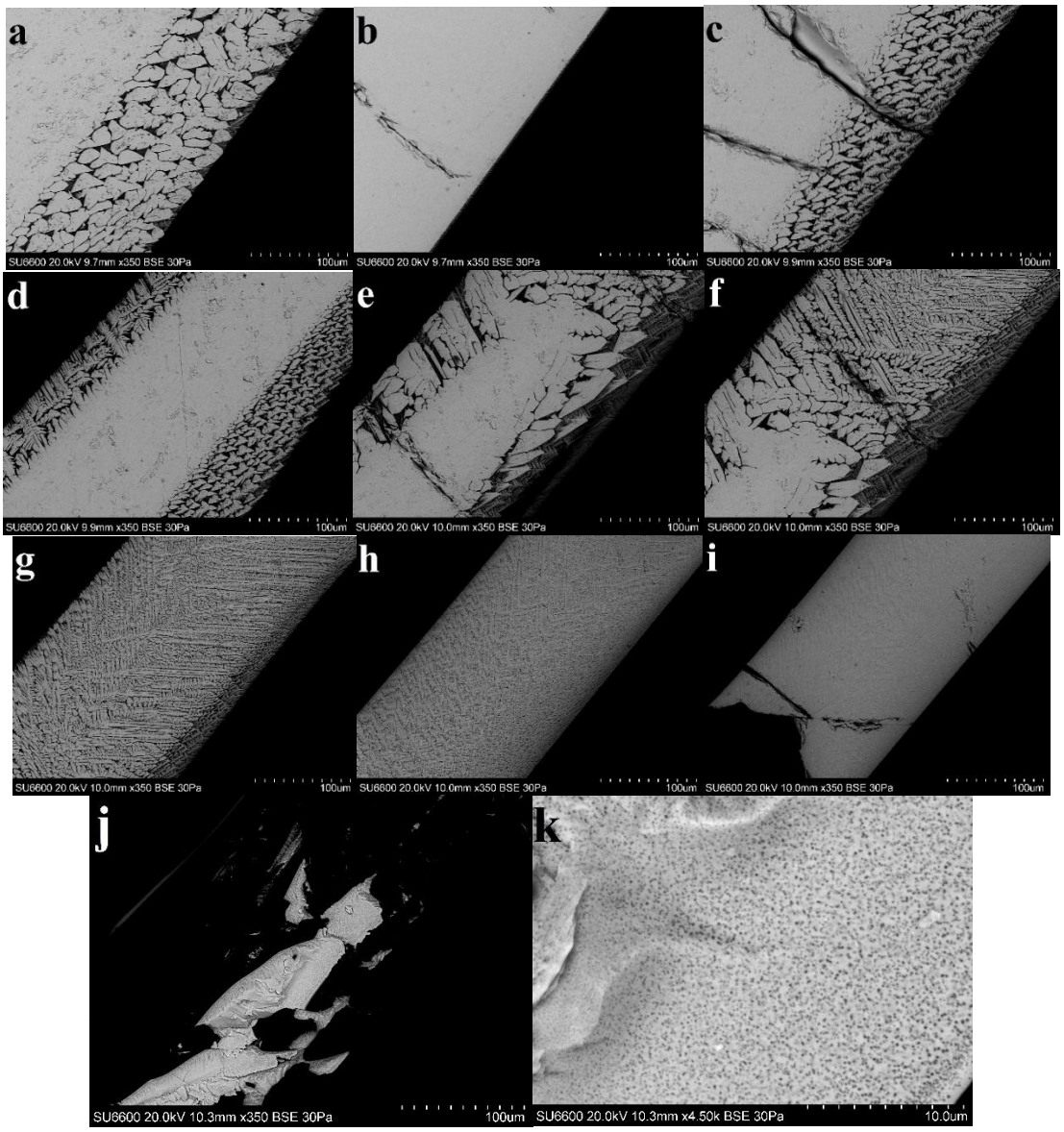

Figure B-8. Serie of SEM micrographs taken along the sample shown in Figure 7. The micrographs were taken starting from the beginning of the bulge (large diameter core) to the end of the core sample. The homogeneous phase in micrographs a), b), c), d) and f) is the non-molten BGO precursor sample. Grains as well as dendrite-like microstructures were observed at the core-cladding interface. Micrographs e) and f) depict the moment at which the BGO precursor fully melted. The microstructures observed from thereon were a result of a crystallization process. The micrographs j) correspond to the end of the core sample and exhibited a phase separated core as seen in the magnified micrograph k).

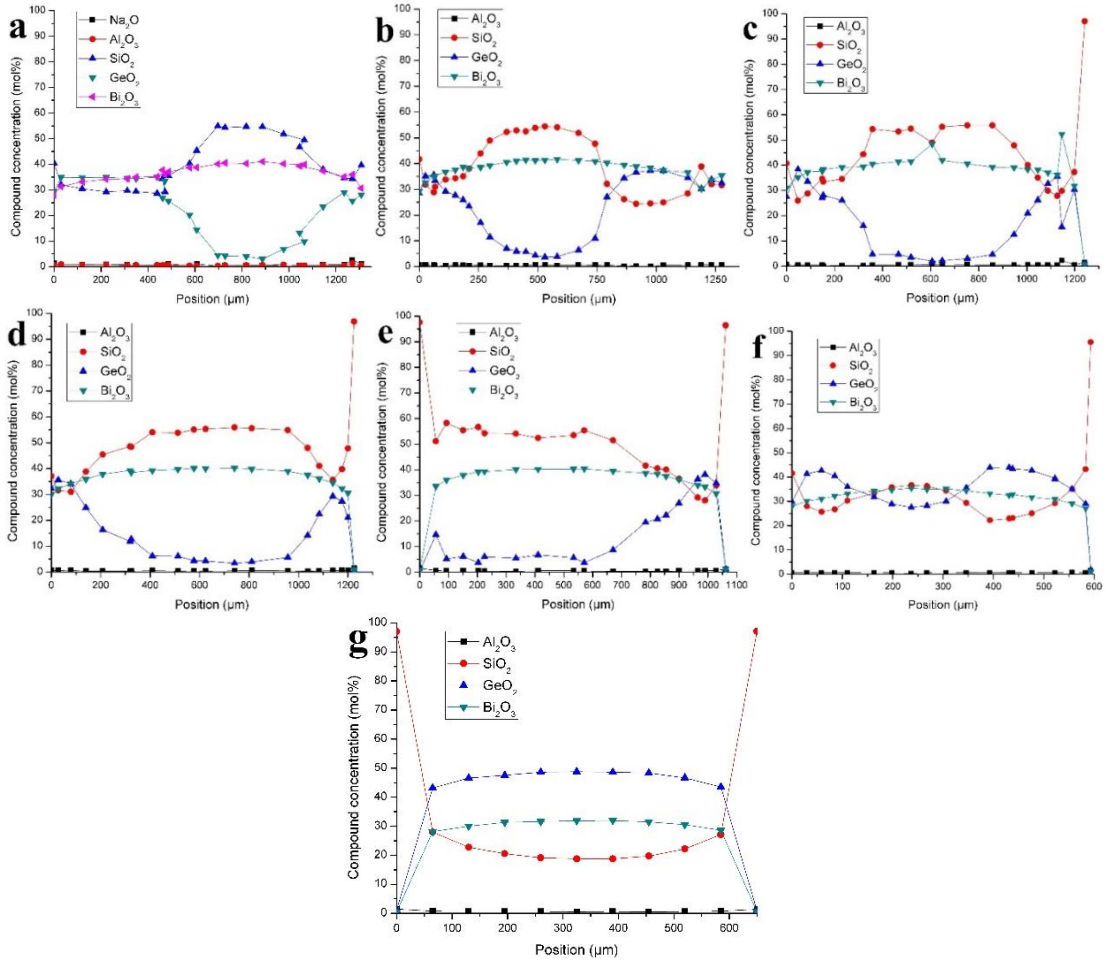

Figure B-9. EDX compound concentration profiles of each core cross-section analyzed along the length of the white core cane (with a yellow tint) derived from the second design in Chapter III section III.5.2. The profiles were taken at various positions along the length of the cane: (a) 0 μm (i.e., end of white core cane), (b) 500 μm, (c) 1500 μm, (d) 2500 μm, (e) 3500, (f) 6500 and, (g) 7500 μm from the end of the cane.

APPENDIX C

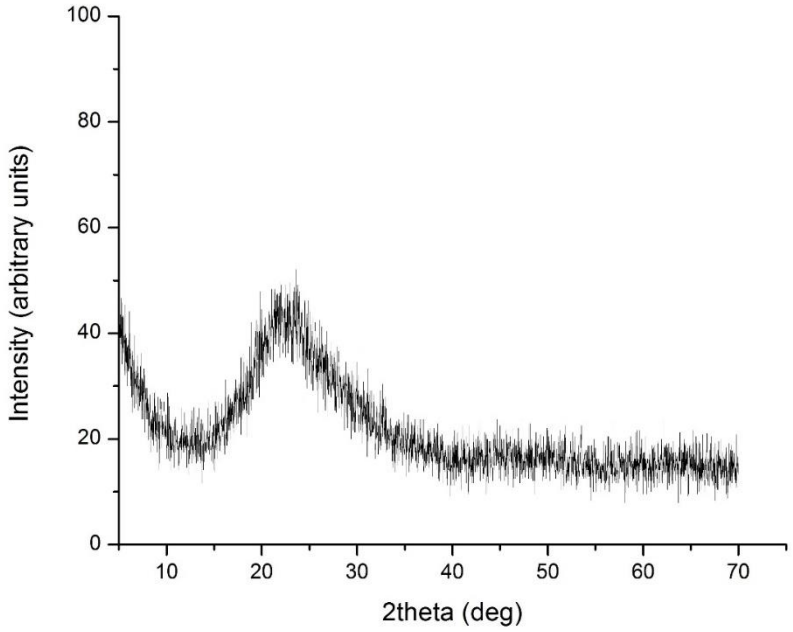

Figure C-1. PXRD diffractogram of a brown core cane obtained from drawing Bi_2O_3 pressed pellets in a borosilicate glass cladding. The core was demonstrated to be amorphous.

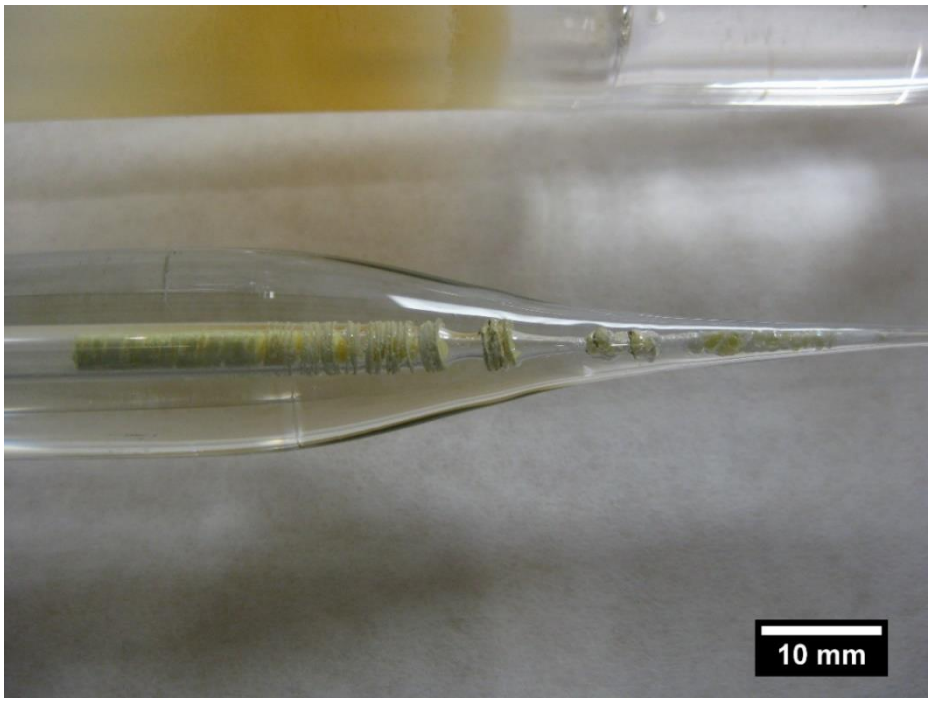

Figure C-2. Picture of the neckdown preform obtained after drawing 3mm Bi_2O_3 pressed powder pellets in a 3x18mm soda-lime silicate glass cladding to 125µm fiber. The pellets were shown to be non-molten (i.e., they retained their shapes) and they were shown to be crushed during the cladding diameter reduction.

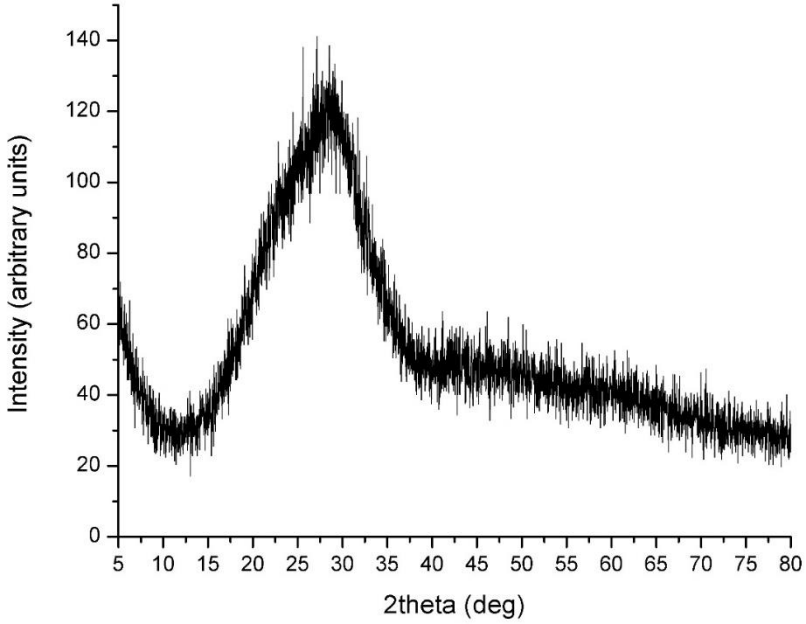

Figure C-3. PXRD diffractogram of a fiber obtained from drawing $10B_2O_3$-$90Bi_2O_3$ (mol%) pressed pellets in a soda lime silicate glass cladding. The core was demonstrated to be amorphous.

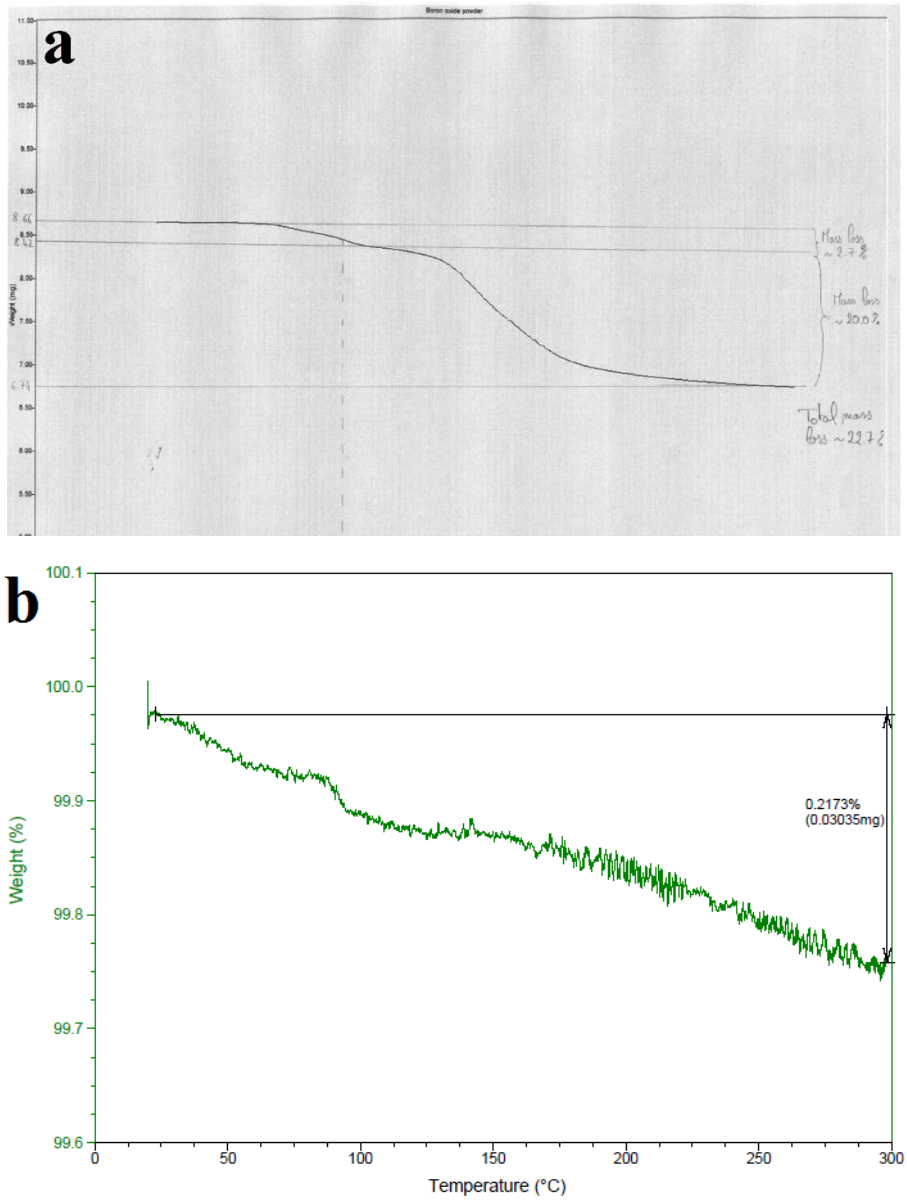

Figure C-4. (a) TGA graph of (untreated) boron oxide powder. A 2.7% mass loss was observed at 100°C and an additional 22.0% mass loss was seen at 300°C, totaling a 22.7% mass loss. These mass losses were attributed to the release of H_2O molecules at 100°C and the release of hydroxyl groups from B-OH bonds at higher temperature respectively. (b) TGA graph of boron oxide powder heat treated at 285°C for 65h. A total mass loss of 0.2% was observed, revealing that the precursor powder was contaminated.

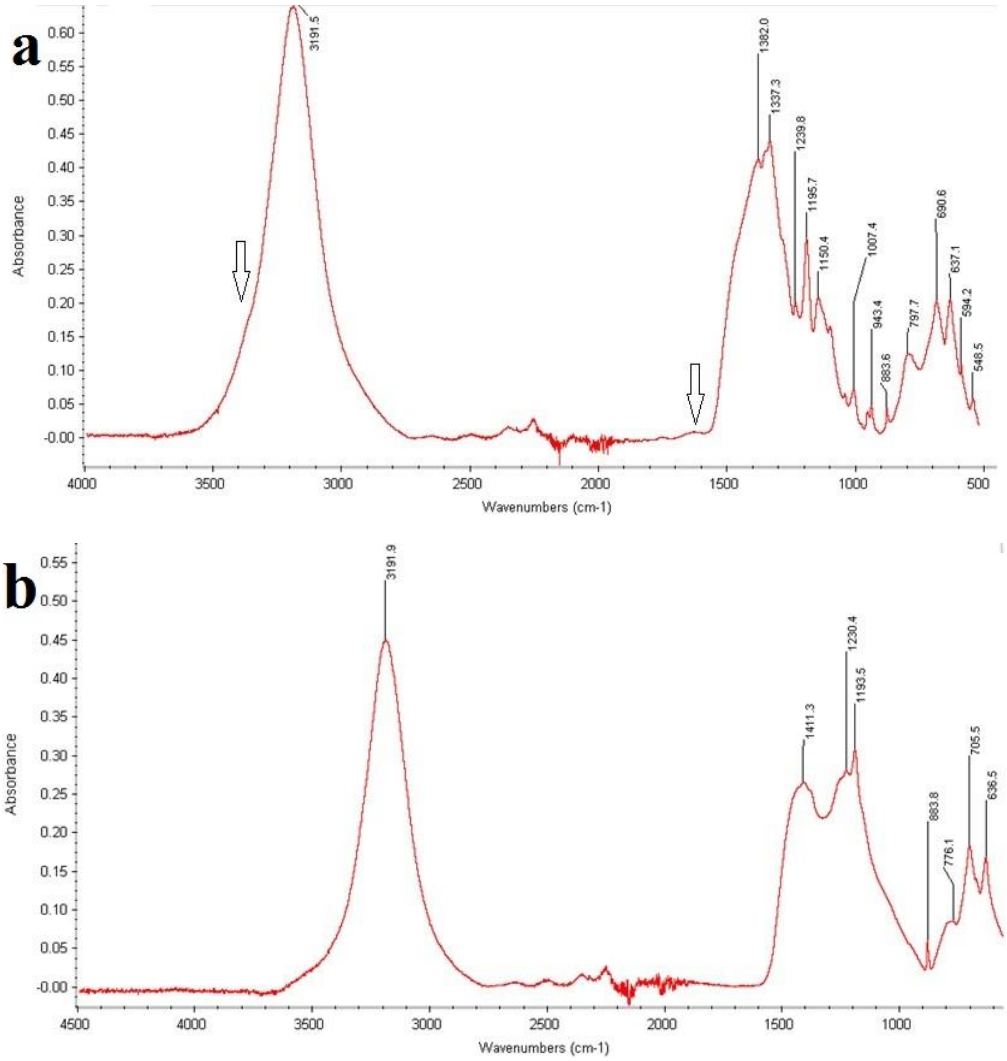

Figure C-5. (a) FTIR spectra of untreated boron oxide powder and, (b) FTIR spectra of boron powder heat treated at 200°C for 15h. The arrows in Figure C-5a point at vibrations specific to water [1], which are shown to disappear in Figure C-5b upon heating the powder. The OH bending mode corresponding to chemically bonded water peaks at ~3200 cm^{-1}, and its absorbance was reduced but not suppressed.

Investigation of compositional effect on the melting behavior of Bi_2O_3 precursor during fiber draw in a soda lime silicate glass cladding using the pressed pellets design.

Draw #1: Three millimeters pellets of $90Bi_2O_3$-$10B_2O_3$ (mol%) were used and inserted in a 3x18 mm dimension soda lime silicate glass cladding. The B_2O_3 was heat

treated beforehand to remove water contamination. Fibers were drawn at 885°C and could not be spooled due to lump formation. Empty core fibers were obtained as seen in Figure C-6.

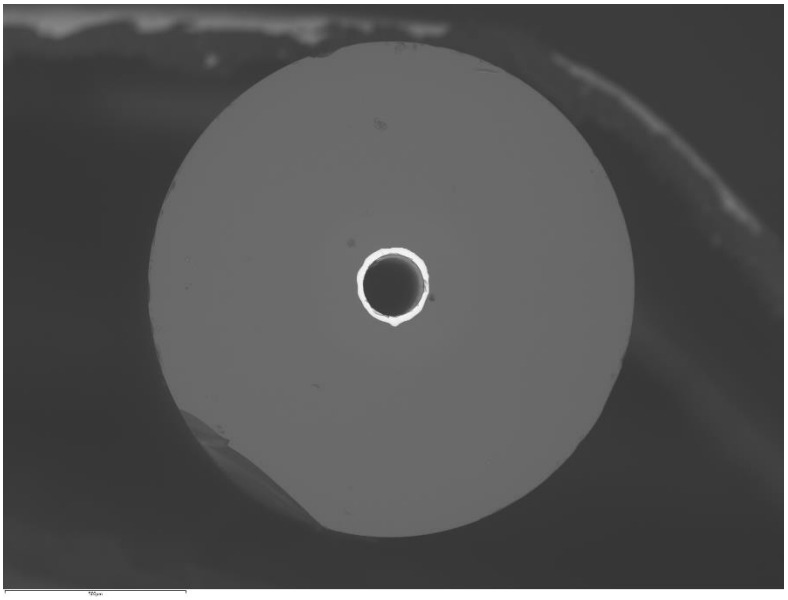

Figure C-6. SEM micrograph of a fiber cross section obtained from draw #1. An empty core fiber was observed.

Draw #2: A powder mix of $13Bi_2O_3$-$87B_2O_3$ (mol%) was packed in a 3x18 mm dimensions soda lime silicate glass cladding. The B_2O_3 was heat treated beforehand to remove the water. Fibers were drawn at 880°C and could not be spooled due to lump formation. A small length of fiber was spooled (10m) but showed an empty core. Fiber scraps were analyzed and revealed a largely cracked core with air gap at the core cladding interface as seen in Figure C-7. The cracks and the gap were associated with the large coefficient of thermal expansion (CTE) of the boron oxide powder (~$150x10^{-7}$ K^{-1}[2]), which likely induced a large contraction upon cooling and ruptured the core from the glass cladding. Interestingly, the CTE of B_2O_3 is about 1.6 times higher than that of the soda lime glass cladding (~$91x10^{-7}$ K^{-1} [3]), and that of Bi_2O_3 is about three times higher (~$100x10^{-7}$ K^{-1}) than that of the borosilicate glass

cladding (~$33x10^{-7}$ K^{-1}) in which it was drawn . In the latter case, core-cladding rupture was not observed despite a larger CTE difference and this behavior is unexplained.

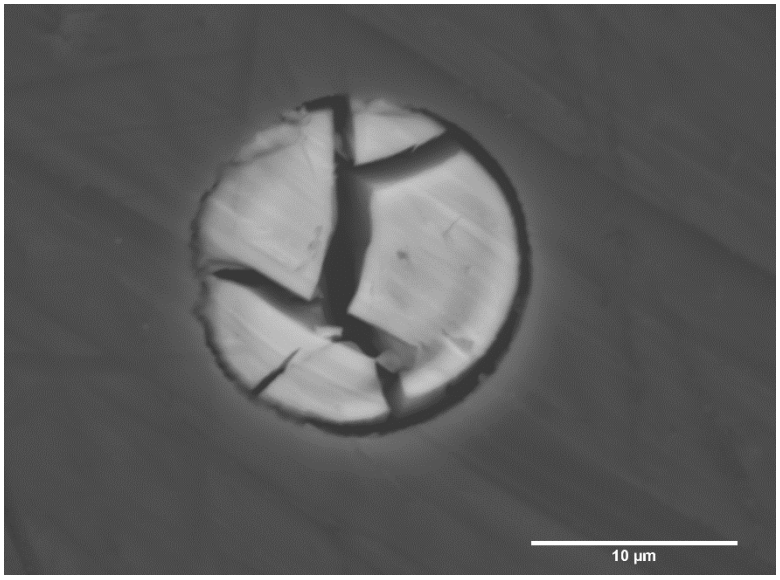

Figure C-7. SEM micrograph of the core cross section from a fiber derived from draw #2. The core was shown to be highly cracked.

Draw #3: Three millimeters pellets of $55Bi_2O_3$-$45B_2O_3$ (mol%) were used and inserted in a 3x18 mm dimensions soda lime silicate glass cladding. The B_2O_3 was heat treated beforehand to remove the water. Fibers were drawn at 885°C and the preform was held at 760°C for 5 min in order to allow time for the powder to melt. Fibers could not be spooled due to lump formation. Fiber scraps were examined and revealed an oblong core as seen in Figure C-27.

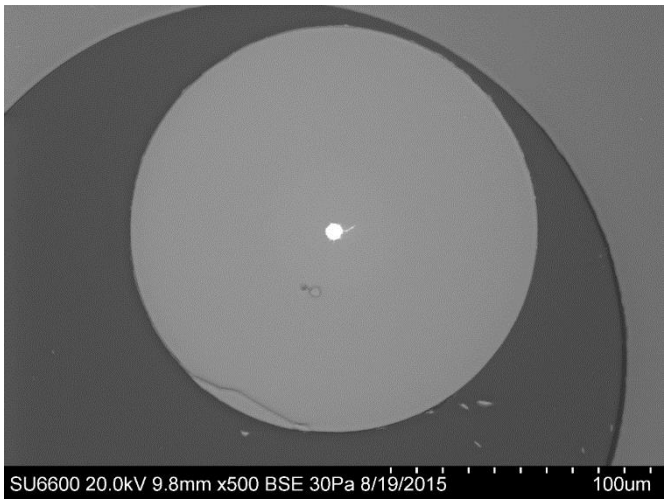

Figure C-8. SEM micrograph of a fiber cross section obtained from draw #3. The core was oblong.

Table C-4. Summary table of compositions and parameters used for the investigation of the melting of Bi_2O_3 powder during fiber draw in soda lime silicate glass cladding.

Draw #	Powder composition (mol%)	B_2O_3 powder heat treated?	Pellets or powder packed?	T_{draw} (°C)	Holding in furnace?	Lumps formation?
1	$90Bi_2O_3$-$10B_2O_3$	Yes	Pellets	885	No	Yes
2	$13Bi_2O_3$-$87B_2O_3$	Yes	Powder packed	880	No	Yes
3	$55Bi_2O_3$-$45B_2O_3$	Yes	Pellets	885	Yes 5min	Yes

DSC experiment between loose Bi_2O_3 powder and pressed Bi_2O_3 powder pellet:

Figure C-9 illustrates the DSC curves obtained heating a loose Bi_2O_3 powder and a pressed Bi_2O_3 powder pellet. The extracted enthalpies of phase transformation and phase transformation temperatures for each precursor design are gathered in Table C-1. Note that the values reported here are not in agreement with the standard values found in thermodynamic tables and, that the DSC curves are by no means meant to be true, but since the experiments were performed in the same condition, the data can be

used for comparison between each experiments. One can see from Table C-1 that, in the case of pressed pellets, the enthalpies of phase transformation 1 and 2 are higher (by 56% and 11% respectively) compared to the loose powder. Plus, the baseline between the two phase transformation peaks (i.e., heat capacity) in Figure C-9 is seen to be higher in the case of the pressed pellets. Thus, the amount of energy needed to melt the Bi_2O_3 pressed pellet seems to be larger than that to melt the loose powder. This, in turn, could indicate that the kinetics of melting are involved during optical fiber draw (as the input power from the furnace is constant) and that longer times could be needed to melt the Bi_2O_3 pressed pellet. Note that the DSC experiment performed here was made in unconstrained conditions (i.e., without a glass cladding around the powder that could act as a barrier for volume expansion).

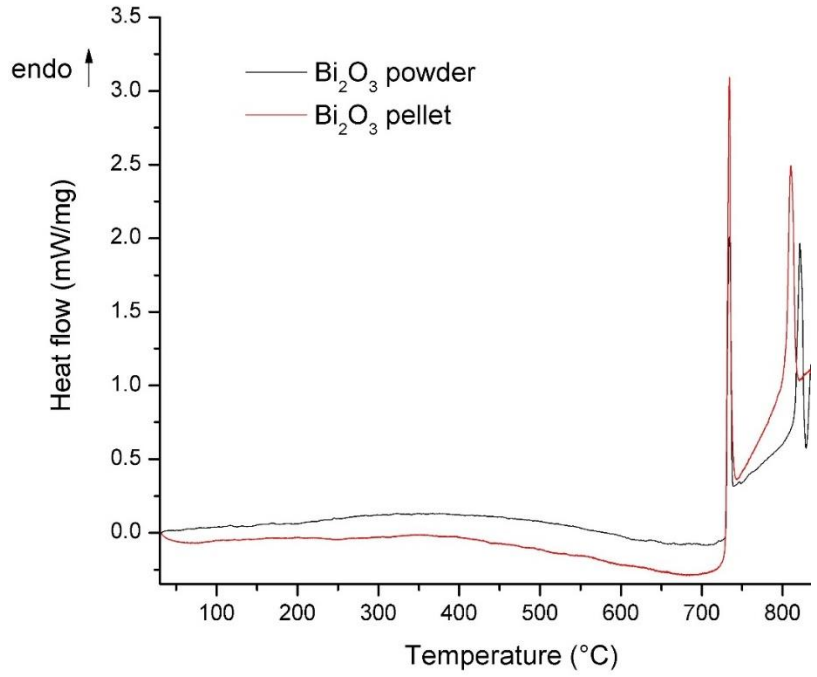

Figure C-9. DSC heating curves obtained for a loose Bi_2O_3 powder (in black) and a Bi_2O_3 pressed powder pellet (in red).

Table C-1. Enthalpies of phase transformations and associated phase transformation temperature extracted from the DSC curves in Figure C-9. The label 1 corresponds to the solid-solid α→δ phase transformation, and the label 2 corresponds to the solid-liquid phase transformation.

Design	ΔH_1 (kJ.mol^{-1})	T_1 (°C)	ΔH_2 (kJ.mol^{-1})	T_2 (°C)	Total energy to melt the compound[a]
Pressed pellet	39.1	734.0	36.8	810.0	131.5
Loose powder	25.3	734.0	33.2	821.3	112.7

[a]This value was obtained by integrating the area under curve of each transformation peak as well as the area under curve between the two transformation peaks.

Experiment investigating the cladding effect on the non-melting behavior of Bi_2O_3 pressed powder pellets:

In this experiment, the cladding effect on the non-melting behavior of pellets was investigated. For that purpose, the pellet diameter used was of 1 mm instead of 3 mm, such that the volume expansion upon the phase transformation is not affected by the glass cladding. Nonetheless, such small pellets were challenging to make, and their stacking such that it formed a "rod" without touching the glass cladding wall failed; and, the pellets were introduced randomly in the borosilicate glass cladding preform in a similar manner to the "poured powder" design. The draw was performed at 1060°C with a draw speed of 0.3 m.min^{-1}. The resultant core cane was fully melted and depicted a brown color. A homogeneous and amorphous core structure was obtained as seen in Figure C-10a. The core concentration was shown to be $47.4SiO_2$-$49.2Bi_2O_3$-$1.5Al_2O_3$-$1.9Na_2O$ as seen in Figure C-10b. While the 1 mm pellets were fully melted, the cladding could not be said to affect the melting behavior of the 3 mm bismuth oxide pellets due to the lack of control during preform preparation.

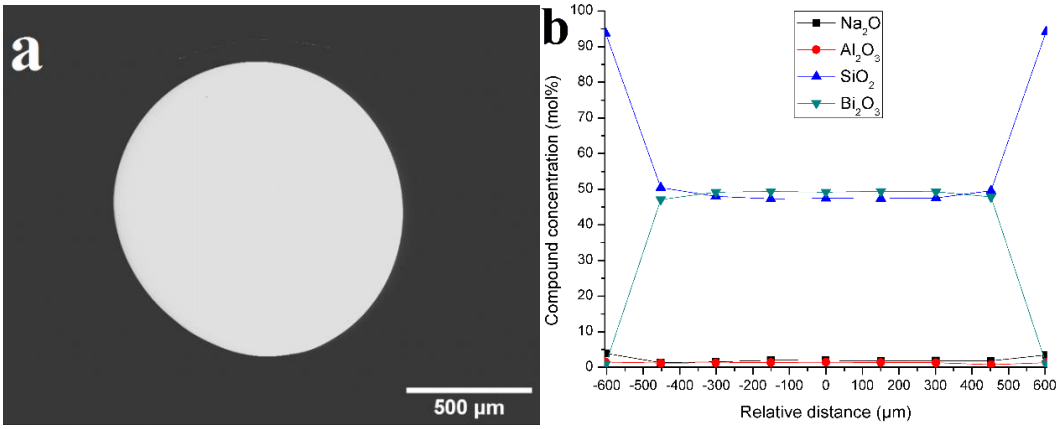

Figure C-10. (a) SEM micrograph of 1 mm pellets drawn in a borosilicate glass cladding tube. (b) EDX compound concentration profile across the same core cane cross section as in Figure C-10a.

Additional information for section IV.5:

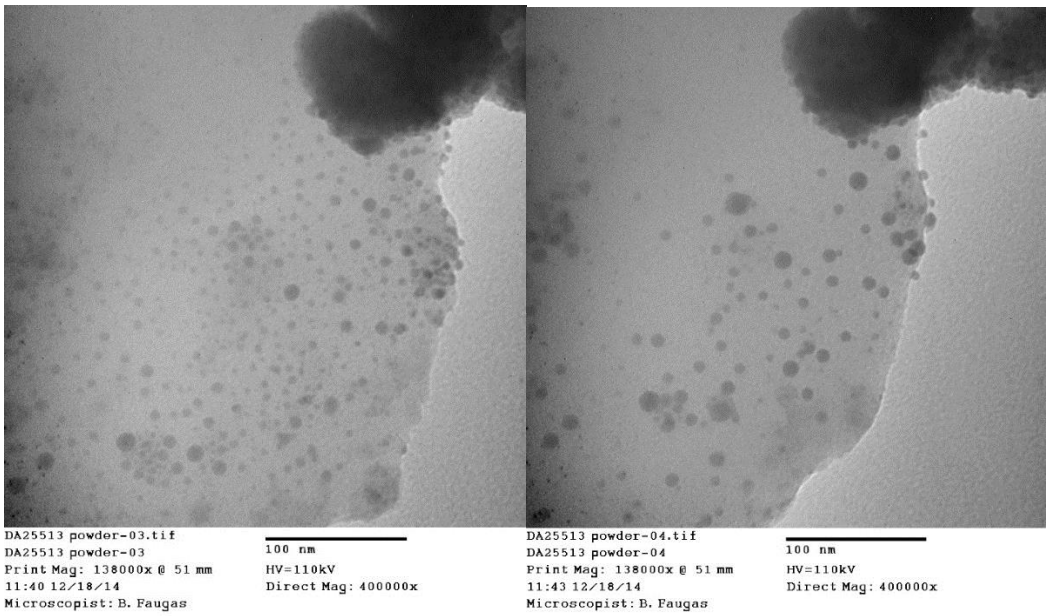

Figure C-11. TEM micrographs showing the evolution of the bismuth nanoparticles within the glass matrix after some time t (on the order of minutes). The nanoparticles are seen to aggregate and cluster together due to the high electron beam energy.

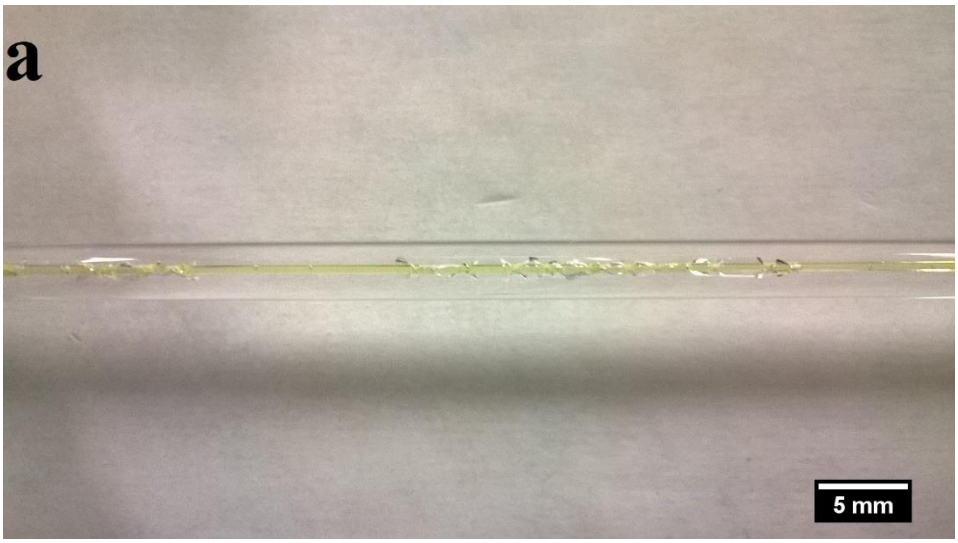

Figure C-12. Optical micrograph of a cane drawn at 1060°C in a 3x30 borosilicate glass cladding from pressed pellets precursor composition of 99.5Bi_2O_3-0.5CeO_2. The core depicted a yellow color.

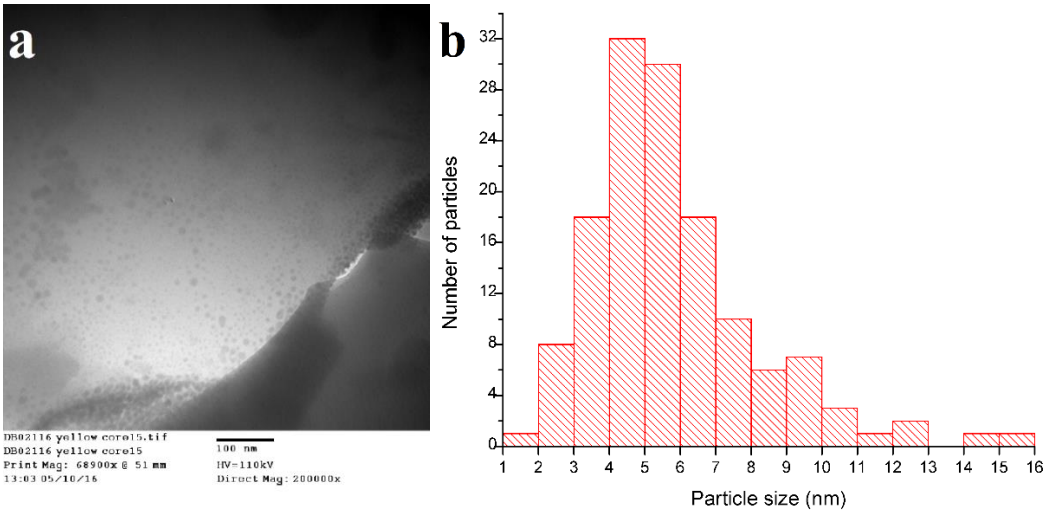

Figure C-13. (a) Representative TEM micrograph of glass particles obtained from yellow glass core canes. The initial precursor composition was 99.5Bi_2O_3-0.5CeO_2. Nanoparticles were observed with an average size of 5.8 ± 2.4 nm. (b) Associated histogram showing the size distribution of the bismuth nanoparticles.

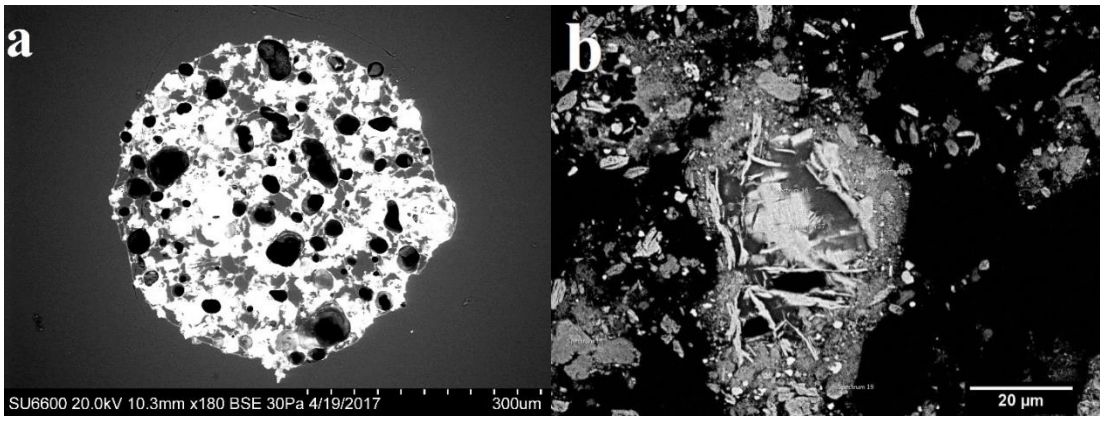

Figure C-14. SEM micrographs of a core cane cross section obtained from drawing a composition of 50wt%DURAN®-50wt%(14.3Bi_2O_3-85.7CeO_2 mol%) in a borosilicate glass cladding. (a) Core micrograph showing voids and, (b) magnified micrograph with enhanced contrast revealing a powder-like core microstructure. The voids were thought to be the result of oxygen release from the CeO_2 reaction, while the core microstructures were thought to be non-molten Ce_2O_3. The powder-like structure composition was found to be 41.5SiO_2-55.0Ce_2O_3-1.9Bi_2O_3-0.7Al_2O_3-0.8Na_2O.

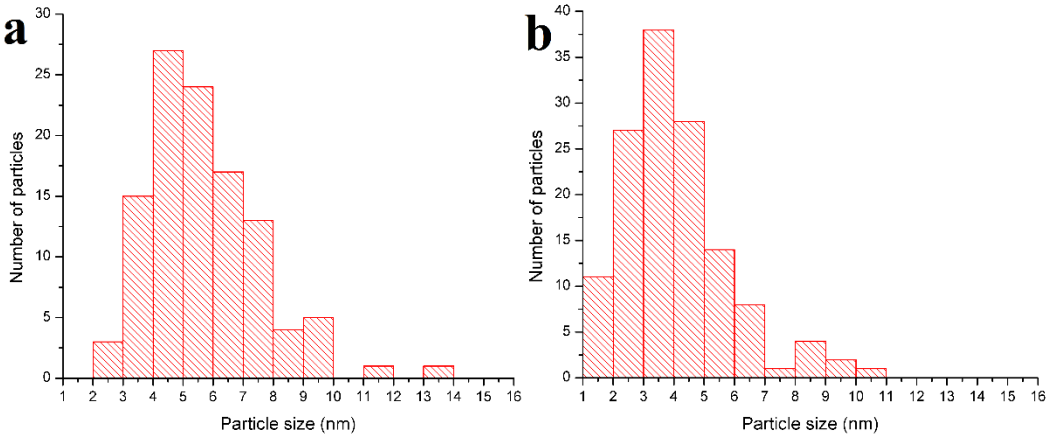

Figure C-15. Histogram of particle size distribution for (a) brown core and (b) yellow core canes obtained within the same cane draw. The average particle size was found to be 5.6 ± 1.9 nm and 4.0 ± 1.8 nm in the brown and yellow core respectively.

References

[1] J. L. Parsons and M. E. Milberg, "Vibrational Spectra of Vitreous B_2O_3-xH_2O," *J. Am. Ceram. Soc.*, vol. 43, no. 6, pp. 326–330, 1960.

[2] A. K. Varshneya, *Fundamentals of Inorganic Glasses*, 1st editio. New York: Academic Press, 1994.

[3] Schott glass, “AR-GLAS® brochure.” [Online]. Available: http://www.schott.com/d/tubing/04f08d52-1060-400c-ac91-3d5adfeaca7d/1.0/schott-tubing_brochure_ar-glas_english.pdf.